

**HYDROTHERMAL EXPERIMENTS (300°C) CONDUCTED USING
BANNOCK RHYOLITE TUFF (MONTANA) AND CONWAY GRANITE
(NEW HAMPSHIRE): IMPLICATIONS FOR HIGH-LEVEL NUCLEAR WASTE
DISPOSAL AND COMPARISONS WITH GEOTHERMAL SOLUTION DATA**

A Thesis Submitted
to the Temple University Graduate Board

in Partial Fullfiment
of the Requirement for the Degree

MASTER OF ARTS

by

Arthur C. Lee

1990

DEPARTMENT COPY

**HYDROTHERMAL EXPERIMENTS (300°C) CONDUCTED USING
BANNOCK RHYOLITE TUFF (MONTANA) AND CONWAY GRANITE
(NEW HAMPSHIRE): IMPLICATIONS FOR HIGH-LEVEL NUCLEAR WASTE
DISPOSAL AND COMPARISONS WITH GEOTHERMAL SOLUTION DATA**

A Thesis Submitted
to the Temple University Graduate Board

in Partial Fulfillment
of the Requirement for the Degree

MASTER OF ARTS

by

Arthur C. Lee

1990

DEPARTMENT COPY

Hydrothermal Experiments (300°C) Conducted Using
Bannock Rhyolite Tuff (Montana) and Conway Granite
(New Hampshire): Implications for High-Level
Nuclear Waste Disposal and Comparisons with
Geothermal Solution Data

by

Arthur C. Lee

A Thesis Submitted in Partial Fulfillment of the
Requirements for the Master of Arts Degree in
Geology, College of Arts and Sciences.

Temple University
Philadelphia, Pennsylvania

1990

Approved

by:

and:

and:

Dr. Gene C. Ulmer

Dr. David Grandstaff

Dr. George H. Myer

Thesis Advisors

Date:

August 8, 1990.

ABSTRACT

Holocrystalline Conway granite, and 95% glass Bannock Rhyolite Tuff were reacted with $3.4 \times 10^{-3} \text{M}$ NaCl solution in Dickson rocking autoclave experiments conducted at 300°C . Granite and tuff experiment data were compared against similar basalt data to determine the effects of rock type (granite, glassy tuff, and 10-40% glass Basalt) and crystallinity in containing high-level nuclear waste. These data were evaluated to determine the degree to which short-term autoclave data correspond with the long-term chemistry of geothermal solutions.

Redox comparisons of 300°C autoclave solutions indicate that the stable $\log f_{\text{O}_2}$ produced by reactions with rhyolitic glass are 3-5 units more oxidizing than those with granite or basalts. More oxidized redox potential may result in higher waste container corrosion rates and solubility of UO_2 for spent fuel rods, at a tuff repository site (*i.e.*, Yucca Mountain, Nevada). The redox buffering capacity (based on FeO content) is also lowest for the glassy tuff, followed by granite and basalts, respectively. The exhaustion of highly soluble rhyolitic glass by oxidizing repository solutions may result in the more rapid acceleration of container corrosion- and U-complex release rates at a tuff repository (compared to granite and basalt). In these tuff and granite experiments Fe-Mg poor, Al-rich dioctahedral beidellitic smectites were formed. In comparison Fe-Mg rich, Al-poor trioctahedral smectite (saponite) was formed in 300°C basalt autoclave solutions. The precipitation of beidellitic smectites in the tuff and granite solutions resulted in comparatively acidic solutions (compared to basalt). For tuff and granite, lower repository solution pH may result in comparatively higher container corrosion rates, and greater solubility for UO_2 in spent fuel rods. The illite/smectite mass ratio is higher for the secondary clay minerals removed from the tuff and granite experiments (compared to basalt). The formation of comparatively larger amounts of sorptive smectites in a basalt repository should result in comparatively lower radionuclide mobility (compared to tuff and granite). Lesser amounts of secondary minerals were formed in the granite experiments. The formation of less secondary minerals in granite repository solutions would result in comparatively higher radionuclide mobility at such a site (compared to basalt and tuff). High concentrations of F in glass-influenced tuff repository solutions may result in higher solubility of UO_2 for spent fuel rods. These geochemical criteria suggest that basalt may be the most suitable of the three repository host rock types compared (followed by granite and tuff, respectively).

Experimental solution geothermometer, cation/proton mass ratio, and secondary mineral data from our high SiO₂-rock:water experiments (holocrystalline granite and 95%-glass tuff), Temple basalt (10-40% glass) experiments and geothermal fields, when compared indicate that the granite autoclave solution came closest to emulating long-term geothermal fluid chemistry, followed by the basalt and tuff solutions, respectively. These data indicate that the time interval necessary for short-term autoclave experiments to predict long-term geothermal fluid chemistry is a function of glass content. Natural geothermal field data is considered to be useful in predicting the long-term chemistry of high-level nuclear waste repository solutions. Our results indicate that rock crystallinity should be considered when selecting geothermal analog data for such purposes.

ACKNOWLEDGEMENTS

1. Special thanks to my thesis advisor Dr. David E. Grandstaff for his help, instruction, and advice in completing this thesis project. I am appreciative for his encouragement in continuing my studies at USC, and for his help in enhancing my research ability.

2. Special thanks to my thesis advisor Dr. Gene C. Ulmer for his help in selecting this thesis project, for helping spark my initial interest in the general field of geochemistry, help, encouragement, advice, and instruction.

3. I would also like to thank Dr. Roger P. Cuffey (The Pennsylvania State University, Professor) for encouraging me to continue my studies at Temple University.

4. Thanks are also extended to thesis committee member Dr. G. H. Myer (Temple University) for his help in interpreting the X-Ray diffractometer data.

5. Thanks should also should be extended to the other faculty members in the T. U. Geology dept.

including, Dr. Peter W. Goodwin, Dr. Joyce Castro, Dr. Hill, Dr. E. J. Anderson, and Dr. J.A. Adams.

6. Warm thanks are extended to Mrs. Wilhemenia Simpson, and Mrs. Shelah Burgess for all of their help and their sense of humor.

7. I would like to thank Mr. Jon Cawley (at Temple University) for showing me his techniques in developing photographs.

8. I would also like to thank my fellow graduate students for making my stay at Temple University a friendly one.

9. I would also like to thank Mr. Steven Sylvester of Franklin and Marshall University for his help and instruction in conducting the XRF analyses.

10. My sincerest thanks are offered to my father (Dr. Y. K. Lee) for helping my family survive financially, and to my mother (Mrs. Theresa Lee) for her caring for my son while Jenny and I had other things to do.

11. Most importantly I would like to thank my wife Jenny for her kindness, encouragement, and moral

support. For without her help the writing of this thesis would not be possible.

12. Lastly I would like to thank my son William for distracting me during the writing of this thesis.

Table of Contents

	Page
List of Tables.....	i
List of Figures.....	ii
Introduction.....	1
Experimental Methods.....	9
Characterization of Starting Materials.....	14
Secondary Mineral Analysis.....	27
Solution Parameter Trends <u>vs.</u> Time.....	86
Redox Comparisons.....	123
pH Trends <u>vs.</u> Time.....	141
Cation/proton Comparisons between CG:2, BRT:1, 300°C Temple Basalt Autoclave Experiments, and Icelandic Geothermal Fields.....	157
Tuff and Granite Solution Geothermometer Evaluation.....	168
Summary.....	178
References.....	192
Appendix.....	205

List of Tables

1. Autoclave experiments referred to in this study.....	6
2. Composition analyses of Bannock Rhyolite Tuff (BRT) and Conway Granite (CG).....	21
3. Secondary mineral chart.....	67
4. CG:2 log IAP/K values <u>vs.</u> time.....	74
5. BRT:1 log IAP/K values <u>vs.</u> time.....	75
6. CG:2 solution parameters <u>vs.</u> time.....	87
7. BRT:1 solution parameters <u>vs.</u> time.....	88
8. CG:1 solution parameters <u>vs.</u> time.....	89
9. Geothermometer Readings <u>vs.</u> time.....	170

List of Figures

1. Measured sections of the Topopah Spring Member showing variations in welding zones, and crystallization zones.....	2
2. Photograph of coarse-grained red phase Conway Granite (CG).....	15
3. Schematic diagram showing lithologies intersected by the DOB core at the Red Stone Quarry in New Hampshire.....	17
4a. Bannock Rhyolite Tuff sample location map (BRT).....	18
4b. Conway Granite sample location map.....	18
5. EDS spectrum and SEM photomicrograph of unreacted BRT glass.....	20
6a. Primary Conway Granite XRD pattern.....	22
6b. Primary Bannock Rhyolite Tuff XRD pattern...	24
7. LaMaitre diagrams.....	26
8. EDS spectrum and SEM photomicrograph of secondary amorphous silica from BRT 1.2.....	30
9. EDS spectrum of illite and smectite from BRT 1.2.....	31
10. EDS spectrum and SEM photomicrograph of illite, anhydrite, and smectite from BRT	

1.7.....	32
11. EDS spectrum of illite, anhydrite, and smectite from BRT 1.7.....	34
12. EDS spectrum and SEM photomicrograph of Ca- smectite and illite from BRT 1.9.....	35
13. BRT 1.2 aliquot X-ray diffractogram.....	37
14. BRT 1.3 aliquot X-ray diffractogram.....	39
15. BRT 1.4 aliquot X-ray diffractogram.....	40
16. BRT 1.5 aliquot X-ray diffractogram.....	41
17. BRT 1.6 aliquot X-ray diffractogram.....	42
18. BRT 1.7 aliquot X-ray diffractogram.....	43
19. BRT 1.8 aliquot X-ray diffractogram.....	44
20. BRT 1.9 aliquot X-ray diffractogram.....	45
21. BRT 1.10 aliquot X-ray diffractogram.....	46
22. BRT 1.4 ethylene glycol treatment XRD results.....	48
23. BRT 1.5 ethylene glycol treatment XRD results.....	49
24. BRT 1.6 ethylene glycol treatment XRD results.....	50
25. BRT 1.10 ethylene glycol treatment XRD results.....	51
26. SEM photomicrograph of illite and primary K- feldspar from CG:1 quench solution.....	54
27. EDS spectrum and SEM photomicrograph of smectite from CG:2 quench solution.....	56

28. EDS spectrum of illite and smectite from CG:2 quench solution.....	57
29. EDS spectrum of secondary quartz from CG:2 quench solution.....	58
30. EDS spectrum and SEM photomicrograph of primary hastingsite from CG:2 quench solution.....	59
31. CG 1.E Quench aliquot X-ray diffractogram...	61
32. CG 2.E Quench aliquot X-ray diffractogram...	62
33. CG:1 Quench ethylene glycol treatment XRD results.....	65
34. CG:2 Quench ethylene glycol treatment XRD results.....	66
35. A near-linear BRT:1 aliquot data point trend on a log Na/H <u>vs.</u> log K/H phase diagram indicating a probable dioctahedral illite:smectite (beidellite) phase boundary.	70
36. A near-linear CG:2 aliquot data point trend on a log Na/H <u>vs.</u> log K/H phase diagram indicating a probable high albite:illite phase boundary.....	71
37. Granite experiment: Quartz log IAP/K <u>vs.</u> time.....	76
38. Granite experiment: Hematite log IAP/K <u>vs.</u> time.....	77
39. Tuff experiment: Amorphous silica log IAP/K	

	<u>vs.</u> time.....	78
40.	Tuff experiment: Anhydrite log IAP/K <u>vs.</u> time.....	79
41.	Tuff experiment: Illite log IAP/K <u>vs.</u> time.....	80
42.	Tuff experiment : Ca, Na, Mg Beidellite log IAP/K <u>vs.</u> time.....	81
43.	CG:1 concentration <u>vs.</u> time trends, Major Species.....	92
44.	CG:2 concentration <u>vs.</u> time trends, Major Species.....	93
45.	BRT:1 concentration <u>vs.</u> time trends, Major Species.....	94
46.	Granite and Tuff; K and SiO ₂ trends.....	97
47.	SEM photomicrograph of a etch-pitted quartz grain.....	100
48.	Granite and Tuff; F and Al trends.....	102
49.	Granite and Tuff; Cl and HCO ₃ trends.....	107
50.	Granite and Tuff; Ca and Na trends.....	109
51.	EDS spectrum and SEM photomicrograph of a hydrothermally-etched micropertthite grain from quench aliquot CG:2.....	113
52.	Granite and Tuff; SO ₄ and H ₂ S trends.....	115
53.	Granite and Tuff; Fe and Mg trends.....	118
54.	Granite and Tuff; Mn and Li trends.....	121

55. CG:2: DHEM and SO_4/H_2S oxygen fugacity comparison.....	124
56. Granite, Tuff and Basalt; $\log fO_2$ <u>vs.</u> time.	127
57. Calculated redox buffering capacity of 1 gram of Bannock Rhyolite Tuff, Conway Granite, and average basalt from 0 to 350°C.....	135
58. Granite and Tuff; measured pH values <u>vs.</u> time.....	142
59. Granite and Tuff; calculated pH values <u>vs.</u> time.....	145
60. Diagram showing the $FeO+MgO/Al_2O_3$ <u>vs.</u> SiO_2/Al_2O_3 tie lines used to construct Figure 61.....	150
61. Topology of stability relationships in the system: $(FeO, MgO)-Al_2O_3-SiO_2-H_2O$ (The relationship between smectite composition and pH).....	151
62. Comparisons with previous basalt experiments and Icelandic geothermal fields: $\log Ca/(H)^2$ <u>vs.</u> $\log Na/H$	159
63. Comparisons with previous basalt experiments and Icelandic geothermal fields: $\log Mg/(H)^2$ <u>vs.</u> $\log Ca/(H)^2$	163
64. Comparisons with previous basalt experiments and Icelandic geothermal fields: $\log Na/H$ <u>vs.</u> $\log K/H$	166
65. Tuff geothermometers.....	171

66. Granite geothermometers.....174

INTRODUCTION

Our government is currently considering the long-term storage of high-level commercial nuclear waste in a single central repository 500 meters beneath Yucca Mountain, Nevada [DOE/RW-0198]. The rhyolite tuff in the Yucca Mountain region was formed from volcanic eruptions occurring between 8 and 16 million years ago, as layers with a total thickness of approximately 2170 meters. During the time of these eruptions molten material explosively expanded due to rapidly decreasing gas pressure, spewing hot glass shards and crystals. Layers or lenses which remained glassy are called "vitric tuffs". In some areas the rhyolitic glassy shards tended to devitrify and develop crystals.

At Yucca Mountain the repository will be constructed in the Paintbrush Tuff Formation. The proposed repository horizon is located in the 1100 foot thick (Miocene) Topopah Spring member (the lowermost member) of the Paintbrush Tuff Formation. Figure 1 includes measured sections of the Topopah Spring member showing welded- and crystallization zones at four different drill core locations. This diagram shows that rhyolitic glass is common in non-welded to densely welded zones within the

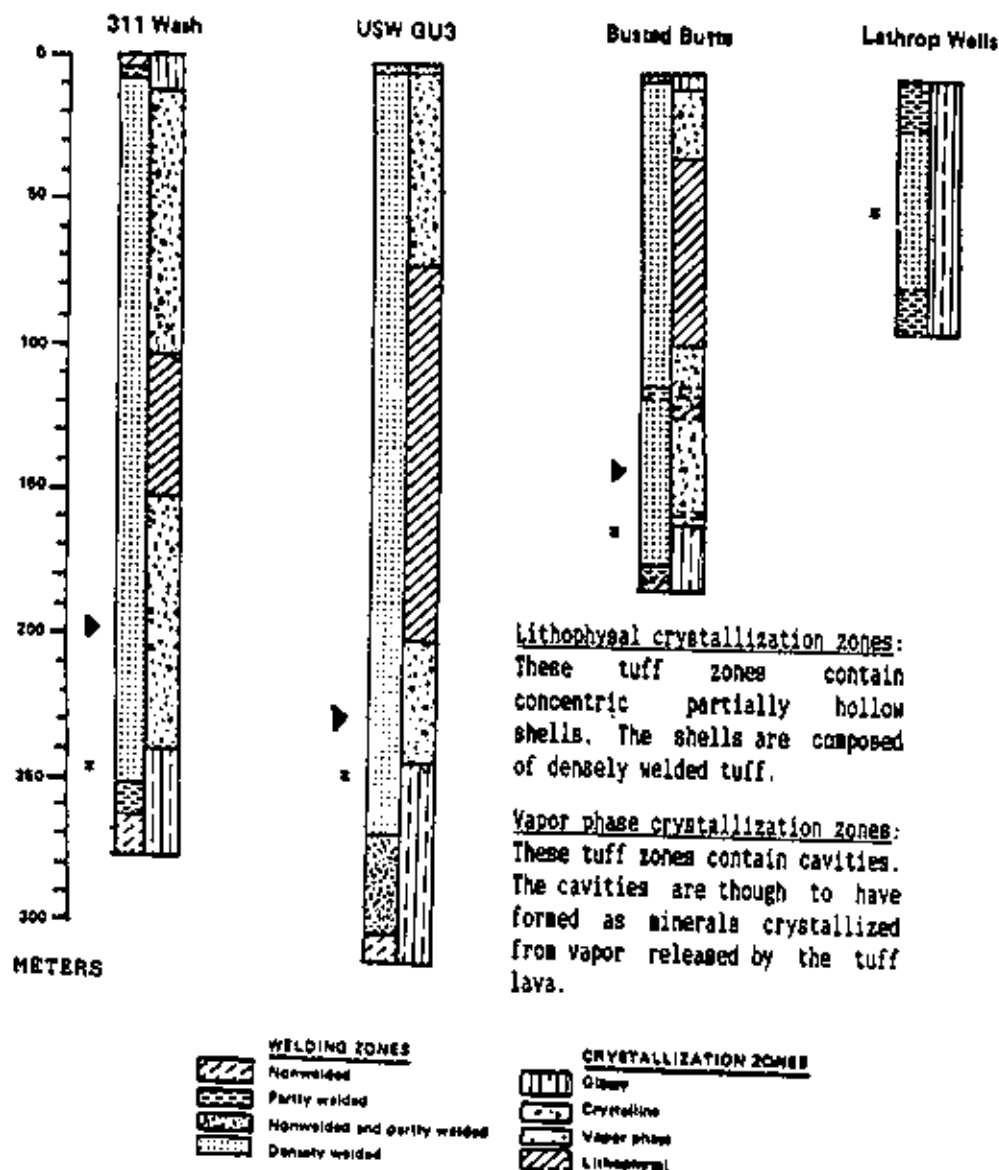


Figure 1: Measured sections of the Topopah Spring Member (Yucca Mountain, Nevada) showing variations in welding zones and crystallization zones (Lipman, 1967). Key: \blacktriangleright -Repository horizon, \ast -Glassy horizon (directly below the repository horizon). The possible effect of rhyolitic glass dissolution, in the containment of high-level nuclear waste (at the proposed Yucca Mountain repository site), is analyzed in this thesis.

Topopah Spring Tuff (Lipman *et al.*, 1966). The average volume percent glass contained within the non-welded glassy tuff layer directly below the devitrified densely-welded-tuff potential repository horizon is slightly greater than 50% (Personal communication, Dr. W. Glassley, National Livermore Laboratory, Earth Sciences Section).

High-level nuclear waste must be isolated for approximately 10,000 years in order for it to lose approximately 99% of its radiation toxicity [DOE/RW-0198]. Water leakage into engineered experimental tunnels (Grossman, 1989), earthquake activity, climate change, and changing aquifer conditions may lead to infiltration of water into this now comparably dry repository site. Manganese oxide mineral deposits have been found in the Topopah Tuff (Carlos, 1986) suggesting groundwater movement through the site in the past.

Dickson rocking autoclave studies have been conducted using densely welded, devitrified 0.1% glass Topopah Spring proposed repository horizon tuff as starting materials (Knauss *et al.*, 1984; Knauss, 1987; Oversby, 1984 1985). However in this thesis, since groundwater at the Yucca Mountain repository site may be influenced by rhyolitic glass dissolution, a Dickson rocking autoclave

experiment using 95% glass rhyolite tuff as starting material was conducted. Solution parameter and secondary mineral formation data from this experiment will be used to determine the effect of rhyolitic glass dissolution in the isolation of high-level nuclear waste. These data will also be evaluated for use in approximating the long-term solution chemistry of geothermal fields.

In the past the U.S. Department of Energy has considered using other materials as host rock for the isolation of high-level nuclear waste. These rock types included basalt, shale, salt, and granite (DOE/TIC-11033). Currently other nations such as The United Kingdom (Savage, 1986; Savage et al., 1987) Japan (Sato, 1985), Sweden (Morano et al., 1987; Birgersson et al., 1988), (Abelin et al., 1988) and Canada (Vandergraaf et al., 1987; Hancock, 1986) are primarily considering the use of granite or granitoid gneisses in the isolation of nuclear waste. Therefore we also conducted experiments using granite as starting material. The secondary mineral and solution parameter data gained from this experiment will be compared to the tuff data. These data are used to determine the advantages and disadvantages of using tuff and granite in isolating high-level nuclear waste.

In recent years many granite:groundwater autoclave studies have been conducted, (Savage, 1986; Savage, 1987; Charles, 1983; Dickson, 1977). Ferrous-iron rich (1.2% FeO by weight) glassy tuff autoclave experiments using deionized distilled water, and NaCl-rich starting solutions have also been conducted (Dickson and Potter, 1982). However when compared with previous Temple University basalt:water experiments, all other experiments were conducted using different experimental parameters (i.e. temperature, experimental apparatus, starting solution, rock powder grain size range, and starting water:rock mass ratio). These differences make it more difficult to determine whether dissimilarities in autoclave solution parameter and secondary mineral data are due to differences in rock type (or crystallinity), or the above mentioned experimental parameters. A list of all of the autoclave experiments mentioned in this study is included in Table 1.

The research for this thesis consists of three hydrothermal experiments conducted at 300°C and 30 MPa using two rocks of similar chemical composition: 1) holocrystalline Conway Granite (experiments CG:1 and CG:2) 2) 95% glass Bannock Rhyolite Tuff (experiment BRT:1). Although peak

TABLE 1: AUTOCLAVE EXPERIMENTS REFERRED TO IN THIS STUDY

ROCK TYPE	TEMP (°C)	PRESSURE (BARS)	WATER	W:R	REFERENCE
Rhyolite	90	50	SGW	10	Knauss <i>et al.</i> (1987)
Rhyolite	90	100	DDW	10	Knauss <i>et al.</i> (1985)
Rhyolite	120	50	SGW	10	Overby <i>et al.</i> (1984)
Rhyolite	150	50	SGW	10	Knauss <i>et al.</i> (1985)
Rhyolite	150	100	DDW	10	Knauss <i>et al.</i> (1985)
Rhyolite	250	100	SGW	10	Knauss <i>et al.</i> (1985)
Rhyolite ^a	200	500	DDW	3	Dickson and Potter (1982)
Rhyolite ^a	200	500	0.1% NaCl	3	Dickson and Potter (1982)
Rhyolite ^a	200	500	2.0% NaCl	3	Dickson and Potter (1982)
Rhyolite ^a	300	500	DDW	3	Dickson and Potter (1982)
Rhyolite ^a	300	500	0.1% NaCl	3	Dickson and Potter (1982)
Rhyolite ^a	300	500	2.0% NaCl	3	Dickson and Potter (1982)
Rhyolite ^a (ERT:1)	300	300	0.002% NaCl	10	Lee <i>et al.</i> (1990)
Granite	80	500	NW	10	Savage <i>et al.</i> (1987)
Granite	150	500	NW	10	Savage <i>et al.</i> (1987)
Granite	250	500	NW	10	Savage <i>et al.</i> (1987)
Granite	300	1000	SEAWATER	3	Dickson (1977)
Granite (CG:2)	300	300	0.002% NaCl	10	Lee <i>et al.</i> (1990)
Basalt	300	300	SGW	5-50	Moore <i>et al.</i> (1984)
Basalt	300	300	SGW	50	McKeon <i>et al.</i> (1984)
Basalt	300	300	SGW	10	Korn (1986)
(spent fuel experiment)					
Basalt	300	300	SGW	50-140	Gardiner <i>et al.</i> (1986)
(re-injection experiment)					
Basalt	300	300	SGW	10	Lazar (1988)
(copper hydrothermal stability study)					
Basalt	300	300	SGW	10	Kacandes (1990)

SGW= SIMULATED GROUNDWATER (FOR SPECIFIC GROUNDWATER COMPOSITION DATA REFER TO INDIVIDUAL REFERENCES, DDW=DISTILLED DEIONIZED WATER, NW=METEORIC WATER,

^a=GLASSY TUFF

temperatures at a high-level nuclear waste repository will probably be lower than 300°C, a temperature of 300°C was chosen for these experiments to analyze rock:water interactions resulting from accelerated reactions. The results of these high-temperature autoclave interactions are utilized, to make inferences about long-term interactions in lower temperature repository solutions. Rock-powder-grain size range, and starting water:rock mass ratios of the two experiments were identical. The $3.4 \times 10^{-3} \text{M}$ NaCl starting solution selected for these experiments had a ionic strength identical to that of Yucca mountain groundwater (Delaney, 1985). The results of the tuff and granite experiments are compared. Our results are also compared with previous Temple University 300°C basalt:water data. These comparisons are used to determine possible advantages and disadvantages of using rhyolite tuff, granite, or basalt as country rock for the isolation of high-level nuclear waste. In order to accomplish this we need to evaluate the effect of rhyolitic glass vs. granitic holocrystalline textures on solution parameters and secondary mineral evolution.

Secondary minerals formed in the tuff and granite experiments are compared to those identified in 300°C Temple basalt experiments, to help evaluate possible effects on radionuclide mobility and repository porosity. Solution parameter trends will be analysed to determine the factors responsible for changes in tuff and granite solution chemistry. Differences between tuff and granite stable solution chemistry will also be analysed. Stable fO_2 values of these experiments are compared against each other, with those measured in natural geothermal fields, and with previous Temple basalt experiments. Ferrous iron weight percentage values of the Conway Granite, Bannock Rhyolite Tuff, and an average basalt (LeMaitre, 1976) were calculated, to estimate maximum redox buffering capacity values. These values are compared to determine the effect of rock type and crystallinity, on radionuclide mobility, U-complex release rates, and canister corrosion at a high-level nuclear waste repository. For CG:2, for BRT:1, and for Temple basalt:water experiments, stable pH values are compared to determine possible effects on container corrosion and U-complex release rates (*i.e.*, solubility of UO_2 in spent fuel rods).

For CG:2, for BRT:1, and for 300°C Temple basalt, Ca-Na-K (Fournier and Truesdall, 1973), Na-K (White, 1965), and Quartz geothermometers (Fournier and Rowe, 1966) are compared. Stable cation/proton data calculated from these experiments are also compared. These comparisons to geothermal field data are used to determine whether the results of these experiments correspond with those of long-term geothermal field solutions.

EXPERIMENTAL METHODS

Three Dickson rocking autoclave experiments were conducted using Conway Granite (CG:1, CG:2) and Bannock Rhyolite Tuff (BRT:1) sample rock. Descriptions of the Dickson autoclaves may be found in Seyfried et al. (1987). Sample rock powders were reacted with 3.4×10^{-3} μM NaCl solutions at 300°C and 30MPa in flexible gold reaction bags, following methods described by Moore et al. (1985). The initial water:rock mass ratio of both experiments was 10:1.

Sample rocks were ground to the 125-250 μm grain size range using a percussion mortar, and mullite mortar and pestle. Ground sample rocks

were then immersed in an ultrasonic bath to remove adhering fines. Conway Granite and Bannock Rhyolite Tuff major element compositions were measured in duplicate, using a Diano 8300 Automated Vacuum X-Ray Fluorescence Spectrometer, with chrome radiation ($K\alpha_1=2.2897\text{\AA}$, $K\alpha_2=2.2936\text{\AA}$). Mean values were used to determine the composition of the rock samples. An iron titration technique with permanganate developed by Ingamells (1965) was used to determine FeO weight percentages. Oxide weight percentages were input into the Patrx computer program (Jassey, 1985) to determine normative mineral values. Primary minerals and glass were identified using XRD and thin section analyses. One thousand points were counted twice in both the granite and tuff thin sections and mean values were tabulated to determine mineral volume percentage values. Curves based on the number of grains counted and mineral proportions (Van Der Plaas, 1965), were used to evaluate the reliability of the Conway Granite and Bannock Rhyolite Tuff point counts (with a 95% confidence interval).

Secondary minerals were removed from solution aliquots by injection through a $0.22\ \mu\text{m}$ plastic membrane filter, in the method adopted by Kacandes (1989). The filters were then suspended in an

ultrasonic cleaning bath and vacuum filtered through 0.45 μm silver filters. Upon completion of the granite experiments, (CG:1, CG:2), secondary minerals contained in the quench solution were also removed using this method. Secondary minerals contained on each silver filter were analyzed using a Rigaku X-Ray Diffractometer, D/Max-B, automated system with a horizontal goniometer and $\text{CuK}\alpha_1\alpha_2$ radiation ($K\alpha_1=1.5406\text{\AA}$, $K\alpha_2=1.5443\text{\AA}$). Secondary minerals were also identified and photographed using a PGT Energy Dispersive X-Ray Spectrophotometer (EDS) and ETEC Autoscan scanning Electron Microscope (SEM). Secondary minerals from the granite and tuff experiments were treated with ethylene glycol to determine the presence of crystallized smectites. Saturation indices (log IAP/K values) of secondary minerals identified using SEM/EDS, and/or XRD, were calculated to verify the results of our secondary mineral identification analyses.

Solution aliquots were removed throughout the course of these experiments in order to quantify solution variables. A Parkin-Elmer 3030 Atomic Absorption Spectrophotometer was used to measure Ca, Fe, K, SiO_2 , Mg, Li, Na, Al, and Mn solution activities. A Dionex System IC System 14 Liquid

Ion Exchange Chromatograph was used to determine F, Cl, and SO_4 activities. Total dissolved carbonate (ECO_2) concentration was measured using a ultraviolet, light-aided, infra-red Dohrmann carbon analyzer. An Orion specific ion meter and electrode was used to make H_2S measurements. A Corning specific ion meter was used to conduct room temperature pH measurements.

Solution $\log fO_2$ was calculated using mean dissolved H_2 concentrations, using the Valco 1000 Trace Gas Analyzer according to the methodology developed by (Kishima and Sakai, 1984 and Grandstaff *et al.*, 1985). Redox buffering capacity values were calculated using Conway Granite, Bannock Rhyolite Tuff, and average basalt FeO weight percent data, and O_2 solubility values (for solutions ranging from 0° to $350^\circ C$) from (Naumov, 1973). The average FeO wt% value used for the average basalt calculation is based on the mean of 3621 analyses (LeMaitre, 1976).

Solution parameter values were inputted into the computer program HIPHR2 (Racandes and Grandstaff, 1989; Grandstaff *et al.*, 1990) to calculate, in situ pH, $\log IAP/K$, $\log fO_2$, saturation indices, geothermometer temperatures, and \log cation/proton mass ratio values.

The first granite experiment (CG:1) continued for 100 hours, but was terminated by rupture of the gold bag. Before rupture, four solution aliquots were analysed, and the quench solution was filtered in order to identify secondary minerals. The data from CG:1 was compared with CG:2 data to assess the reproducibility of these granite experiments. The second completed granite experiment (CG:2) continued for 2762 hours until termination. The tuff experiment (BRT:1) solution aliquots and secondary minerals were analyzed to 3531 hours from the start of the experiment. This experiment will be reinjected with fresh solution (by Mr. Cheng Yan of Temple University), to determine effects on solution parameter equilibration, solution redox, and secondary mineral formation. These analyses if successful will be presented and published at a major meeting in the near future.

The procedures used throughout, while not QA-1 verified are exactly based on the 13 standard operating procedures developed while this lab at Temple University was under DOE QA-1 contract (1985-1989). Even with the Graham-Rudmann curtailment of contract, our research nevertheless continued at a QA-1 level of effort, and very careful record keeping.

CHARACTERIZATION OF STARTING MATERIALS:**GEOLOGIC SETTINGS**

The Conway Granite is located in areas of New Hampshire, Maine, and Vermont, and belongs to the Triassic to Cretaceous age White Mountain plutonic-volcanic series (Hoag et al., 1977). The Conway Granite includes the following major different phases (Billings, 1964):

- 1) A coarse-grained red phase
- 2) A porphyritic phase
- 3) A medium grained phase
- 4) A green medium-grained phase
- 5) A fine grained phase

The coarse grained red-phase Conway Granite DOE core sample rock used in experiments CG:1 and CG:2, was obtained from Dr. Wallace A. Bothner (University of New Hampshire). Figure 2 contains a photograph of a sample of coarse grained red-phase Conway granite collected at Red Stone Quarry, N.H (by Dr. Gene C. Ulmer, Temple University).

As a result of the encouragement of Governor Thomson of New Hampshire, the members of his Mineral and Energy Resources Council, and the interest of the National Energy and Research



Figure 2: Photograph of a Coarse-Grained Red-Phase Conway Granite hand sample recovered from the Red Stone Quarry, New Hampshire (Collected by Dr. Gene C. Ulmer, Temple University).

Administration, a 3000 foot borehole with a 1 7/8" diameter core was recovered from the Red Stone Quarry near North Conway, New Hampshire. A portion of the 1499-1503 feet section of this DOE core was used for these autoclave experiments.

The drillcore sample was part of the coarse-grained red-phase Conway Granite typical of the quarry at Redstone (Hoag et al. 1977). Figure 3 is a schematic diagram showing the various igneous rock lithologies intersected by the Red Stone Quarry DOE core. Figure 4a is a section of the geologic map of New Hampshire compiled by Marland P. Billings of the USGS in 1955 showing the core site location with an X. The rock sample primarily consists of pink crystals of microperthite (averaging 6 mm. in diameter), smoky quartz grains (averaging 3 mm. in diameter), and biotite flakes (averaging 2 mm. in diameter).

The Bannock Rhyolite Tuff sample used in these experiments was purchased from Mr. J. Fox of Ward's Natural Science Est. in Rochester, N.Y., and was collected by Miss Carla Carey of Montana State University. The Bannock Rhyolite Tuff is one of a series of little studied rhyolitic flows in the Frying Pan Basin in southwestern Montana [Oral communication: (Dr. D. Alt, U. of Montana, 1989)].

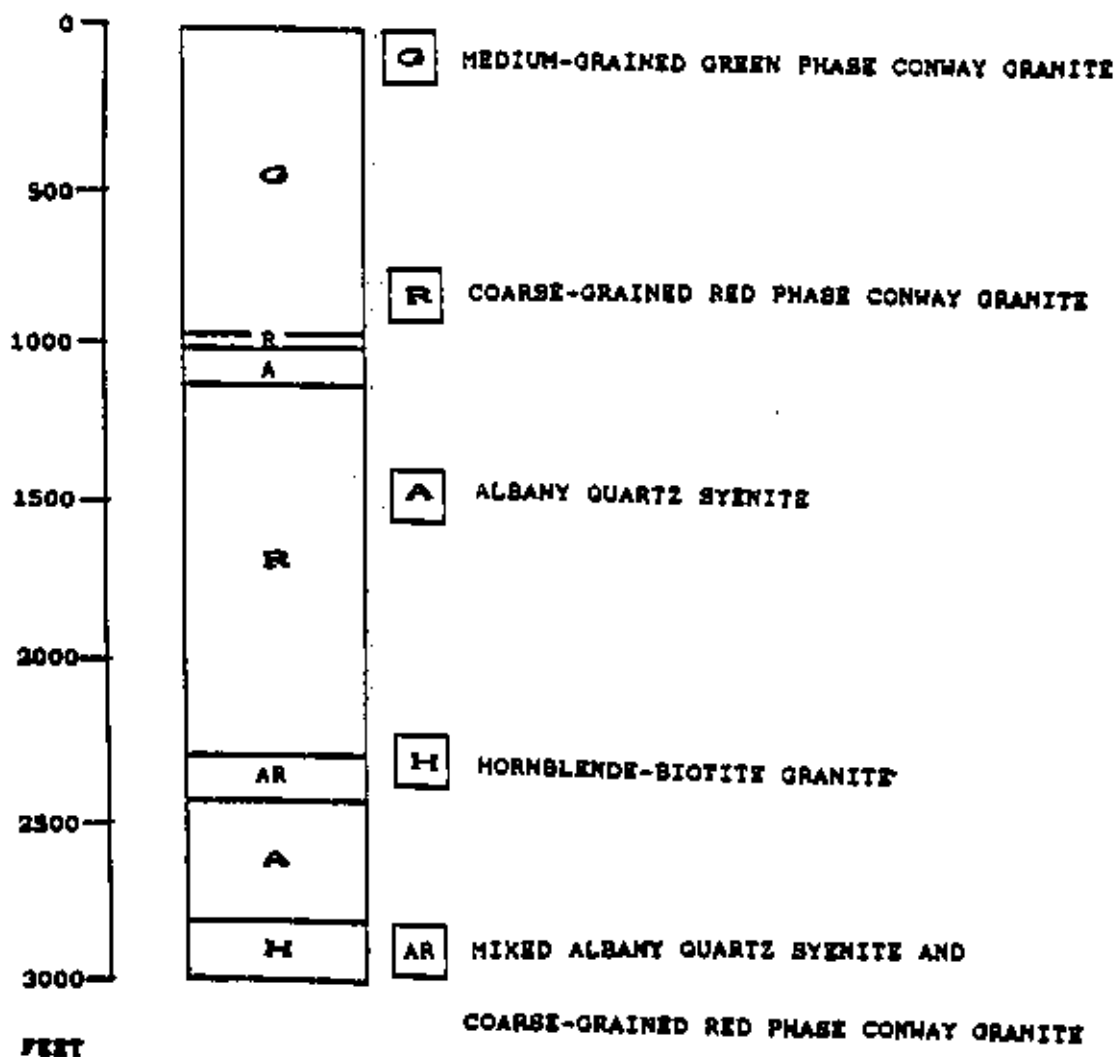


Figure 3: Schematic diagram showing the various lithologies intersected by the DOE core taken from the Red Stone Quarry in New Hampshire (Hoag, 1976). The Coarse-Grained Red-Phase Conway Granite sample used in experiments CG:1 and CG:2 was removed from the 1499-1503 foot section of this core.



Figure 4a: Conway Granite sample rock location

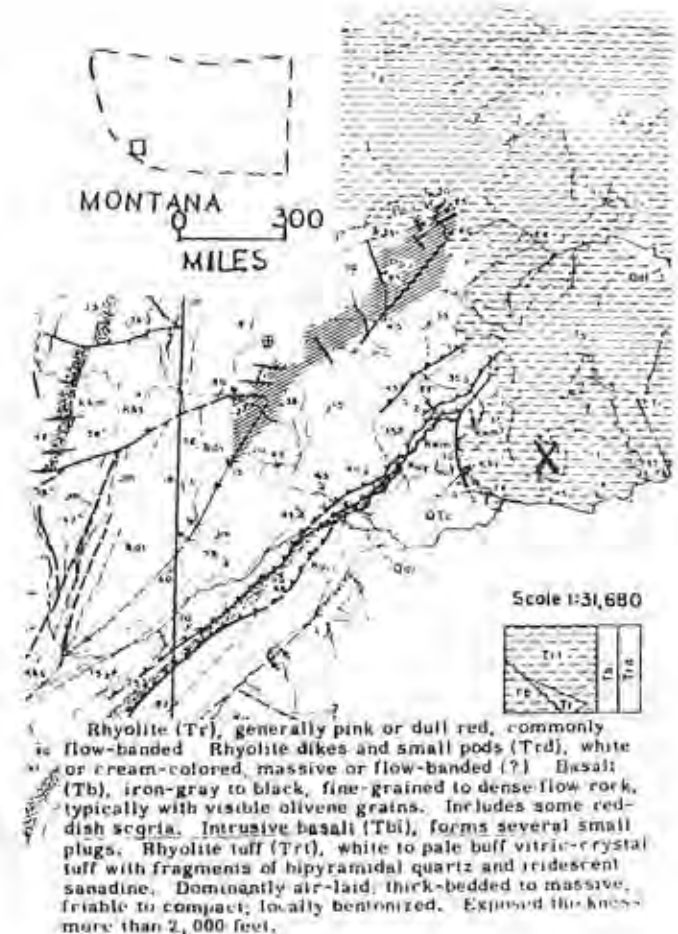


Figure 4b: Bannock Rhyolite Tuff sample rock location

Figure 4b is a portion of the preliminary geologic map of the NW 1/4 of the Willis quadrangle, Beaverhead County, Montana (open file map MBMG 189, W. B. Myers, 1946). The Bannock Rhyolite Tuff sample location with an X. These flows are approximately 40 million years old, and are located 5-6 miles northwest of Dillon in the Frying Pan Basin, Montana. These flows consist primarily (95%) of rhyolitic glass (Winchell, 1914). A SEM photomicrograph and EDS spectrum of the vesicle-rich rhyolitic glass contained within the Bannock Rhyolite Tuff sample rock is included in Figure 5.

STARTING MATERIAL ANALYSES

The results of thin section and XRD analyses were used to determine the modal mineralogy of the Conway Granite and Bannock Rhyolite Tuff (listed in Table 2).

The Conway Granite contains microperthite with thin lamellas of plagioclase ($7\% \pm 1.3\%$), found within the microcline ($60\% \pm 2.3\%$). The CG 2.0 XRD peaks best correlate with low albite and microcline, respectively (Figure 6a). The quartz ($29\% \pm 2.0\%$) found within the sample rock is smoky colored due to radiation damage. Hoag (1977) found

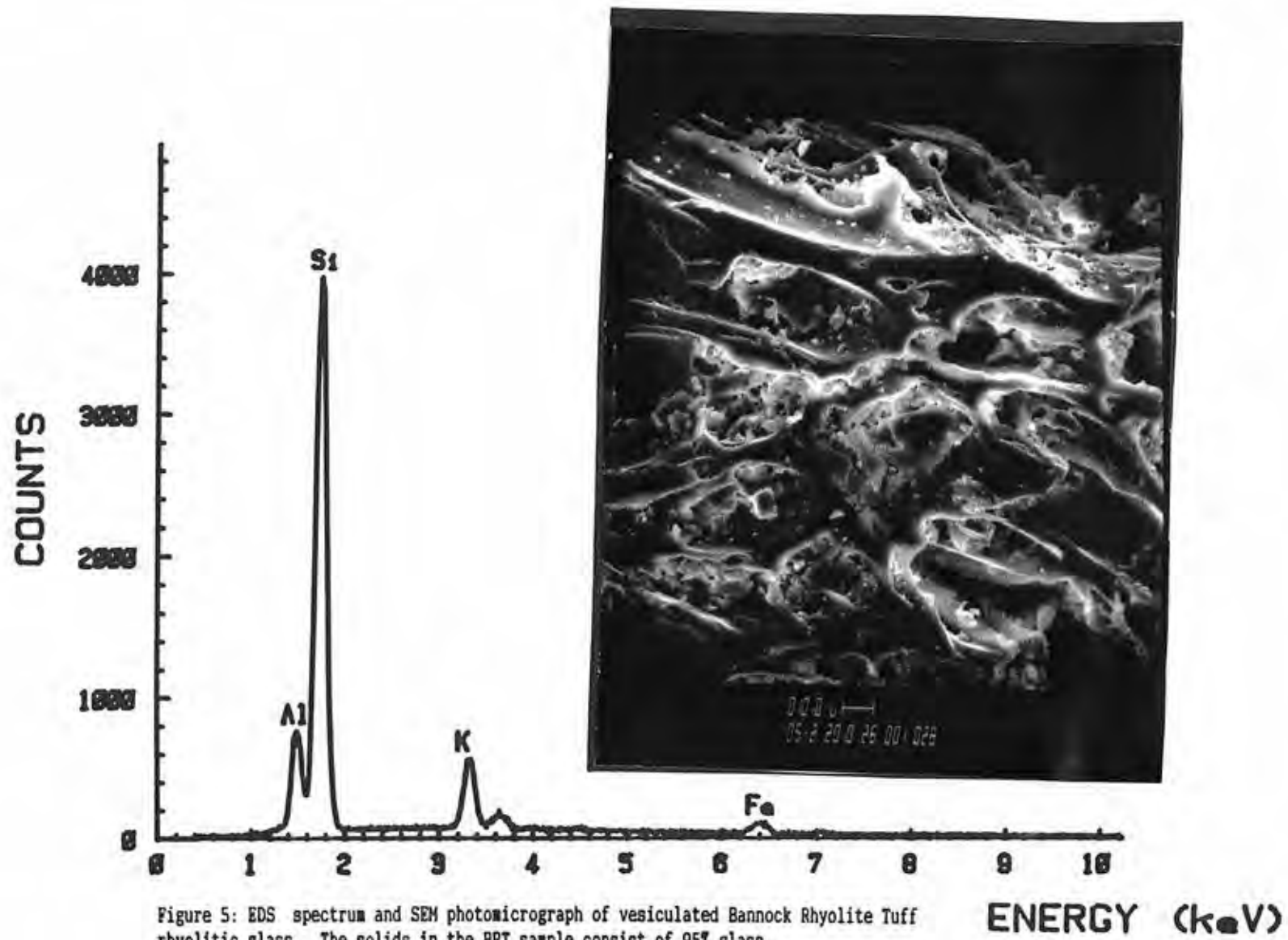


Figure 5: EDS spectrum and SEM photomicrograph of vesiculated Bannock Rhyolite Tuff rhyolitic glass. The solids in the BRT sample consist of 95% glass.

Table 2: Results of Bannock Rhyolite Tuff and Conway Granite Composition Analyses

Table A: Chemical Mode			Table B: Normative Minerals			Table C: Modal Mineralogy		
Oxides (Wt.%)	Conway Granite	Bannock R. Tuff	Normative Minerals(%)	Conway Granite	Bannock R. Tuff	Minerals (%)	Conway Granite	Bannock R. Tuff
SiO ₂	74.53	69.53	Quartz	29.68	36.66	Quartz	29.0	1.8
TiO ₂	0.17	0.27	Corundum	3.18	Biotite	4.0	0.4
Al ₂ O ₃	12.92	14.32	Orthoclase	26.22	31.80	Plagioclase	7.4	0.6
Fe ₂ O ₃	1.89	2.03	Albite	15.20	17.84	K-feldspar:		
FeO	2.47	0.43	Anorthite	2.97	6.95	Microperthite	59.6
MnO	0.07	0.03	Hypersthene	2.72	0.65	Sanidine	1.7
MgO	0.01	0.25	Magnetite	2.70	0.73	Glass	94.7
CaO	0.66	1.35	Monatite	1.63	Calcite	Tr.	Tr.
Na ₂ O	4.22	2.01	Ilmenite	0.32	0.53	Cristobalite	Tr.
K ₂ O	4.30	5.13	Apatite	0.02	0.02	Fayalite	Tr.
H ₂ O ⁺	0.55	3.02	Diopside	0.17	Mastingsite	Tr.
H ₂ O ⁻	0.03	0.47	Total	100.00%	100.00%	Apatite	Tr.
P ₂ O ₅	0.01	0.01				Fluorite	Tr.
Total	102.02%	98.85%				Magnetite	Tr.
						Pyrite	Tr.
						Zircon	Tr.
						Allanite	Tr.
						Total	100.0%	100.0%

Note: Major element weight oxide percentages were measured using a XRF spectrometer, with chrome radiation (K_{α1}=2.2897Å, K_{α2}=2.2936Å). A permanganate titration technique developed by Ingalls (1965) was used to determine FeO weight percentages. Normative mineralogy was calculated using the computer program PETER (Jassey, 1985). Thin section analyses were used to determine the modal mineralogy.

This analysis was conducted using $\text{CuK}\alpha$ radiation ($K\alpha_1=1.5406\text{\AA}$, $K\alpha_2=1.5443\text{\AA}$)

Sample Name : CG 2.B

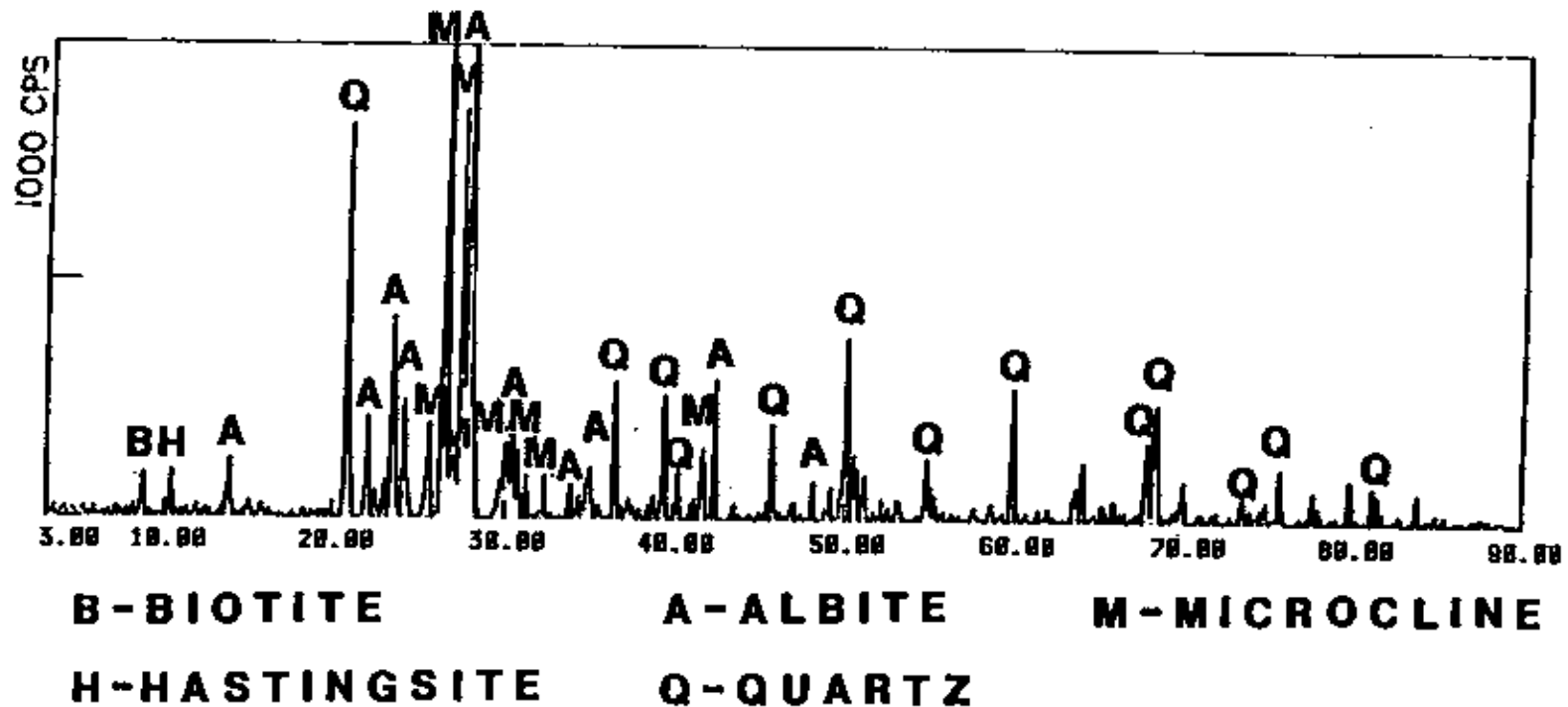


Figure 6a. X-ray diffractogram of unreacted Conway Granite rock powder.

that the Conway Granite has a uranium plus thorium concentration two to four times that of an average granite (i.e. as high as 60 ppm U, and 17 ppm Th for the red-phase). Biotite (4% \pm 1.0%) and hastingsite (Tr.) were also identified using the Figure 6a XRD pattern. Other trace minerals contained within the granite were identified using optical methods only. These minerals included; apatite, zircon, fluorite, allanite, calcite, magnetite, and pyrite.

The Bannock Rhyolite Tuff is composed primarily of vesiculated glass (95% \pm 1.1%). The EDS pattern of this glass (Figure 5) suggests that this glass is rich in Al, K, and lesser amounts of Fe. Analysis of the 125-250 μ m BRT starting material in refractive index fluids, confirmed the 95% volume rhyolitic glass value obtained through thin section point count analysis. The shattered mineral grains in the tuff include quartz (1.8%), sanidine (1.7%), plagioclase (0.8%), and biotite (0.4%). The shattering may have been the result of a explosive eruption. Quartz, sanidine, and albite were identified in the unreacted tuff sample using the Figure 6b X-ray diffractogram. Trace amounts (<1%) of iron-rich olivine, calcite, and cristobalite were identified using optical methods.

This analysis was conducted using $\text{CuK}\alpha_1$ radiation ($\text{K}\alpha_1=1.5406\text{\AA}$, $\text{K}\alpha_2=1.5443\text{\AA}$)

Sample Name : RT-1(Lee)

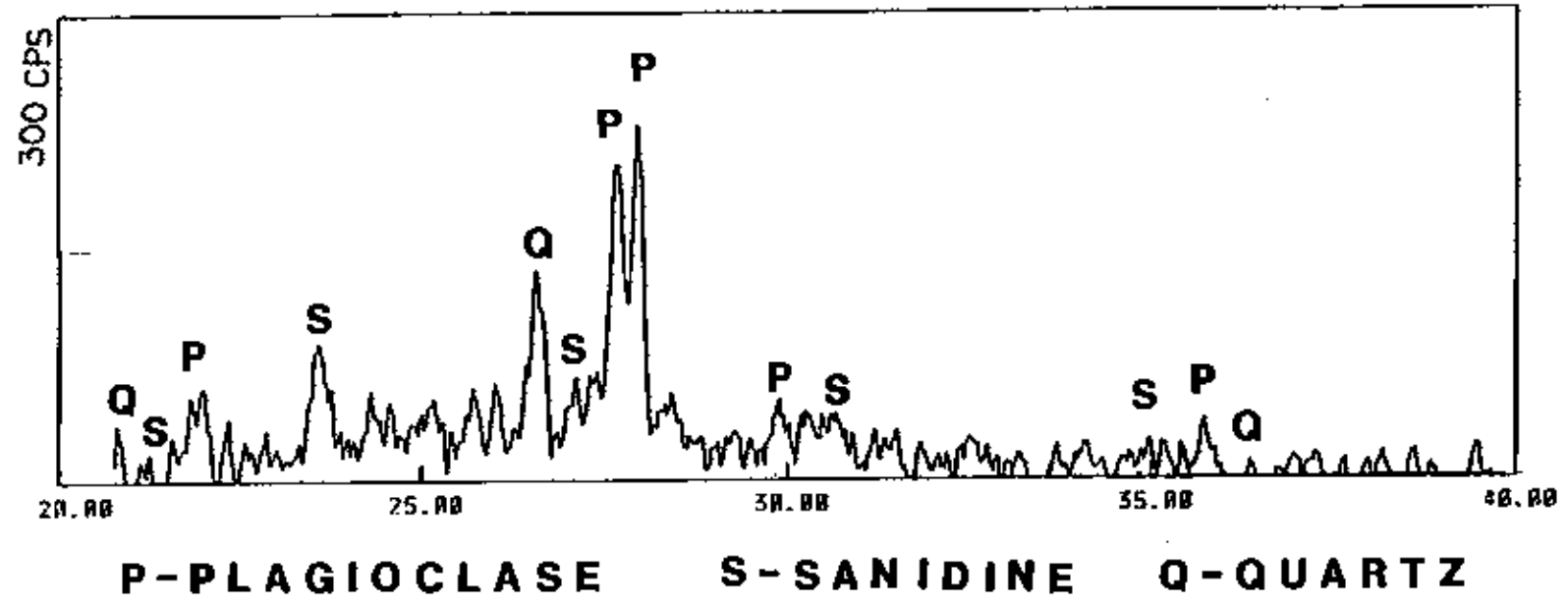


Figure 6b: X-ray diffractogram of unreacted Bannock Rhyolite Tuff rock powder.

The chemical composition and normative analyses are also presented in Table 2. The Conway granite has 2.1 times more Na_2O and 5.7 times more FeO than the tuff. The significance of FeO wt.% on redox buffer capacity, and solution pH is further discussed in the Redox Comparison and pH trends vs. time sections. Otherwise these two rock samples are chemically very similar. All major oxides and normative mineral percentages fall within the LeMaitre (1976) range of average granites and rhyolites (Figure 7). Therefore the results of these experiments can be used to compare the rock:water interactions occurring between a chemically common holocrystalline granite, and a 95% glass rhyolite tuff.

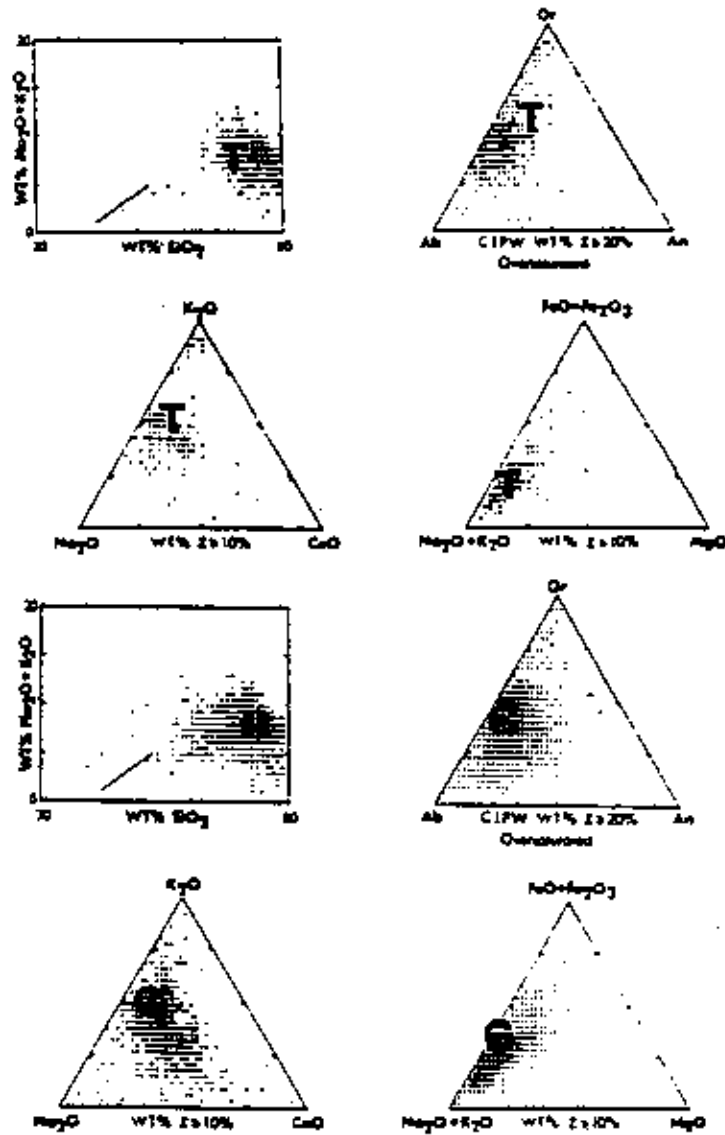


Figure 7: Normative mineral and oxide weight percentage values of the Conway Granite sample (G), and the Bannock Rhyolite Tuff sample (Y). Sample rock values are juxtaposed upon Lemaitre analyses of rhyolites (top) and granites (bottom).

SECONDARY MINERAL ANALYSES

Secondary minerals formed in our experiments were identified using SEM/EDS and XRD techniques. Mineral saturation indices (log IAP/K data) were used to corroborate SEM/EDS and XRD identification results.

Secondary mineral identifications based on EDS spectra and morphology, using SEM/EDS techniques are included in Figures 8-12 (Tuff experiment), and Figures 26-30 (Granite experiments). The bracket scale located near the bottom of all of the included SEM photomicrographs represents a distance of 1 or 10 micrometers, as indicated. Secondary mineral silver filter holders generated the Ag and Cl peaks included in the above mentioned EDS spectra.

Secondary minerals were also identified using X-ray diffractograms (Tuff experiment: Figures 13-25, Granite experiments: Figures 31-34). The d-spacings of diffractogram peaks were matched against values contained within the JCPDS (Joint Committee on Powder Diffraction Standards) file. None of the filtered solution aliquots in both granite experiments (CG:1, CG:2) produced XRD peaks due to the loss of suspended material by the

filtration effect of accumulating granite secondaries in the autoclave sampling stem. Thus while secondary minerals were identified from tuff solution aliquots (Figures 8-25), only granite quench sample solutions were available for secondary mineral research (Figures 26-34). The Ag and Cl peaks produced during X-ray diffraction analyses result from the Ag secondary mineral filter holders.

Table 3 (see page 67) summarizes conclusions from the SEM/EDS and XRD secondary mineral identification analyses.

Saturation indices (log IAP/K values) were calculated using the computer program HIPHPR2 to determine which secondary minerals may be controlling solution composition in the tuff and granite experiment (Tables 4-5). These values were used to construct log IAP/K vs. time diagrams (Figures 37-42) which support the SEM/EDS and XRD secondary mineral identification results.

TUFF SECONDARY MINERALS

EXPERIMENT BRT:1 SEM/EDS IDENTIFICATION RESULTS (FIGURES 8-12): SEM/EDS techniques were used to photograph and identify tuff secondary minerals from aliquots BRT 1.2, BRT 1.7, and BRT 1.9 (Figures 8-12).

The Si peak in the Figure 8 EDS spectrum was used to identify a dark amorphous silica grain removed from the BRT 1.2 aliquot (in the included SEM photomicrograph. In Figure 9 a EDS spectrum containing Fe, Al, Si, K, Ti, Ca, and Mn peaks was used to identify a white fine-grained mixture of illite and Fe-smectite recovered from the BRT 1.2 solution aliquot. The EDS spectrum in Figure 10 contains Si, Fe, Al, K, Ti, Mn, Ca, and Na peaks, used to identify a mixture of white fine-grained secondary illite, smectite, and anhydrite removed from aliquot BRT 1.7. The sulphur peak and part of the Ca peak are thought to indicate the presence of secondary anhydrite, a common Ca-S-bearing mineral alteration product found in geothermal solutions near 300°C (Kenley et al., 1984). The SEM photomicrograph included in Figure 10 shows the above mentioned white-fine grained secondary mineral mixture, and dark rounded primary material

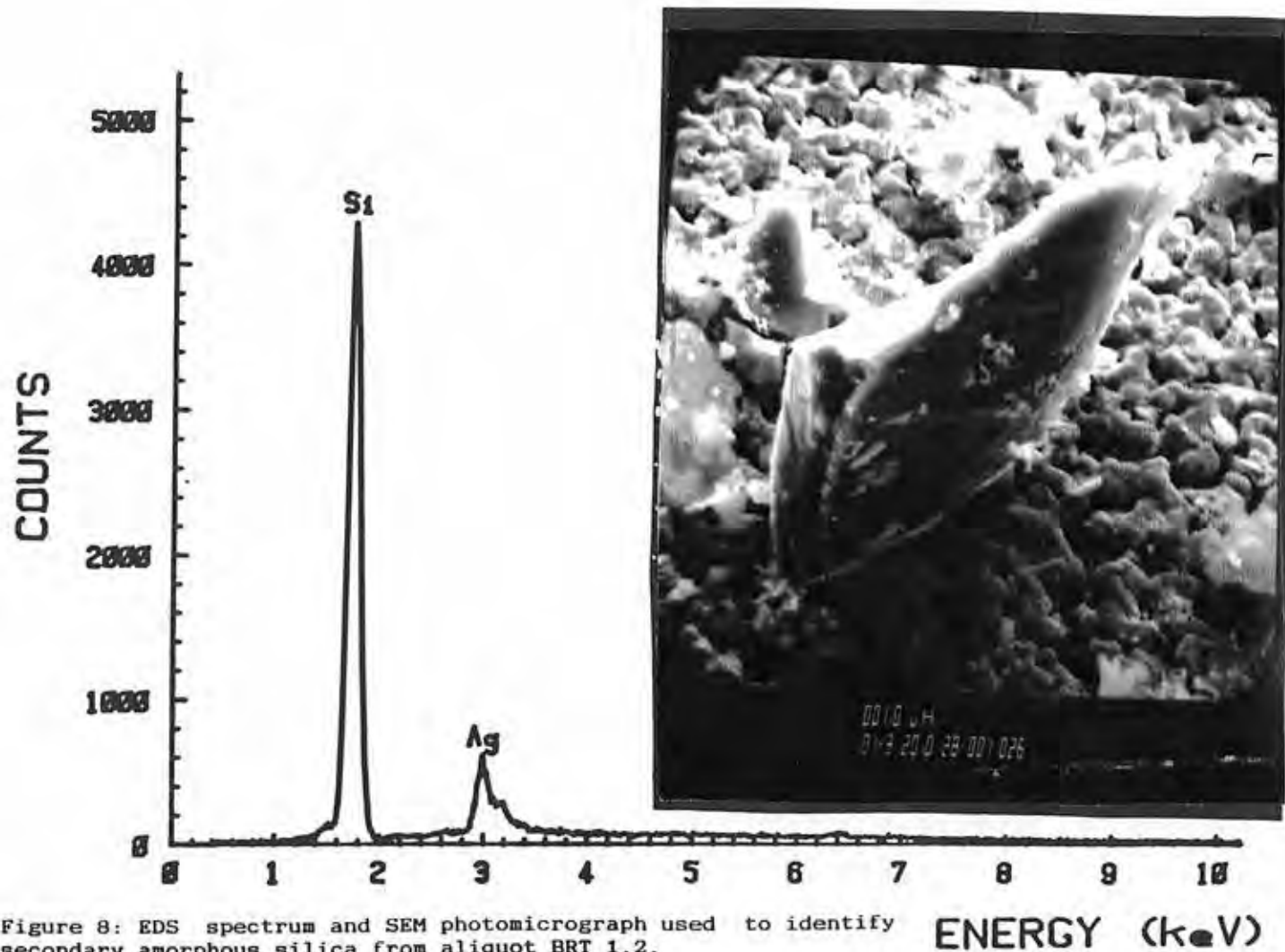


Figure 8: EDS spectrum and SEM photomicrograph used to identify secondary amorphous silica from aliquot BRT 1.2.

ENERGY (keV)

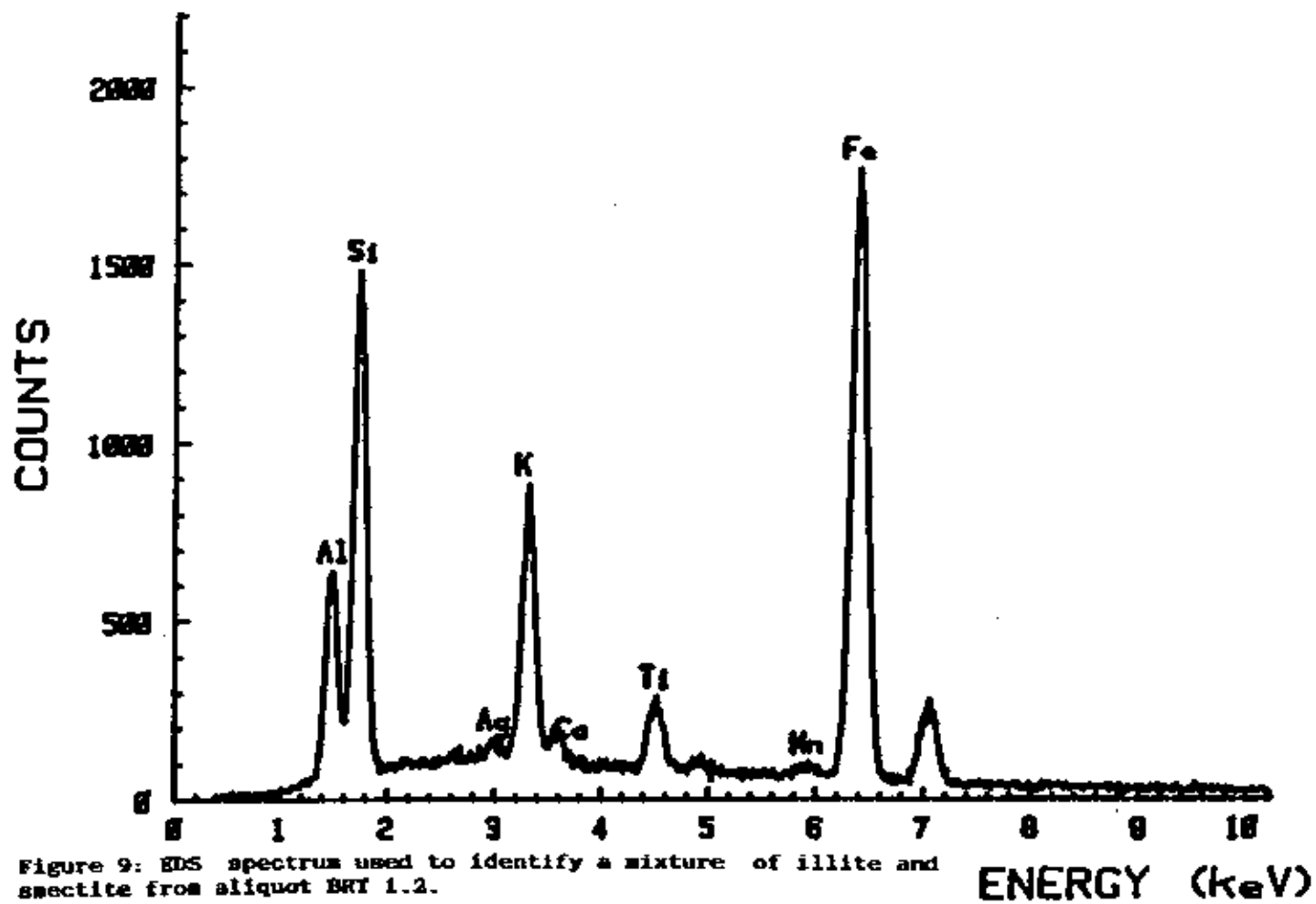


Figure 9: EDS spectrum used to identify a mixture of illite and smectite from aliquot BRT 1.2.

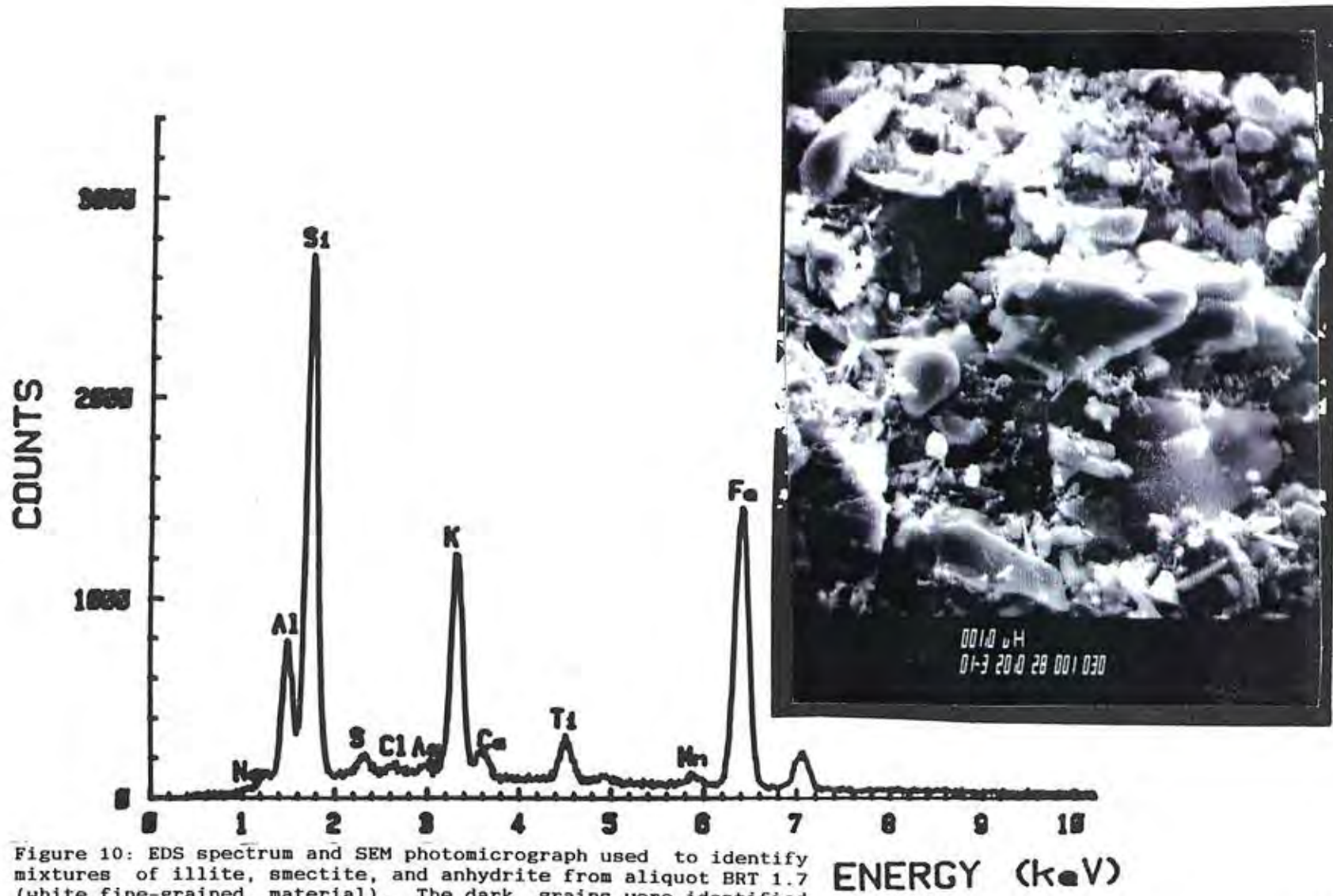


Figure 10: EDS spectrum and SEM photomicrograph used to identify mixtures of illite, smectite, and anhydrite from aliquot BRT 1.7 (white fine-grained material). The dark grains were identified as primary rhyolitic glass and plagioclase.

ENERGY (keV)

grains removed from aliquot BRT 1.7. The primary materials were identified as rhyolitic glass and plagioclase. The Figure 11 EDS spectrum contains the Si, Al, K, Ca, Fe, Na, and Ti peaks used to identify a mixture of illite, anhydrite, and smectite removed from the BRT 1.7 aliquot. The S peak and part of the Ca peak were used to identify the presence secondary anhydrite. The Figure 12 EDS spectrum contains Si, Al, K, Ca, Ti, Mn, and Fe peaks used to identify a mix of Ca-illite and smectite from the BRT 1.9 aliquot. The SEM photomicrograph included Figure 12 shows the above mentioned mixture of Ca-smectite and illite (next to a piece of primary albite). In summary: illite, amorphous silica, smectite(s), and anhydrite were identified in the tuff experiment using EDS/SEM techniques.

EXPERIMENT BRT:1 FURTHER SEM/EDS DATA INTERPRETATION (FIGURES 9-12): The identification of amorphous silica from aliquot BRT 1.2 suggests that secondary amorphous silica formation started to control dissolved SiO_2 concentrations by the 3.3 hour sample. The EDS spectra of BRT clay minerals (Figures 9-12), show a trend of increasing Ca content from BRT 1.2 to 1.9. These results suggest

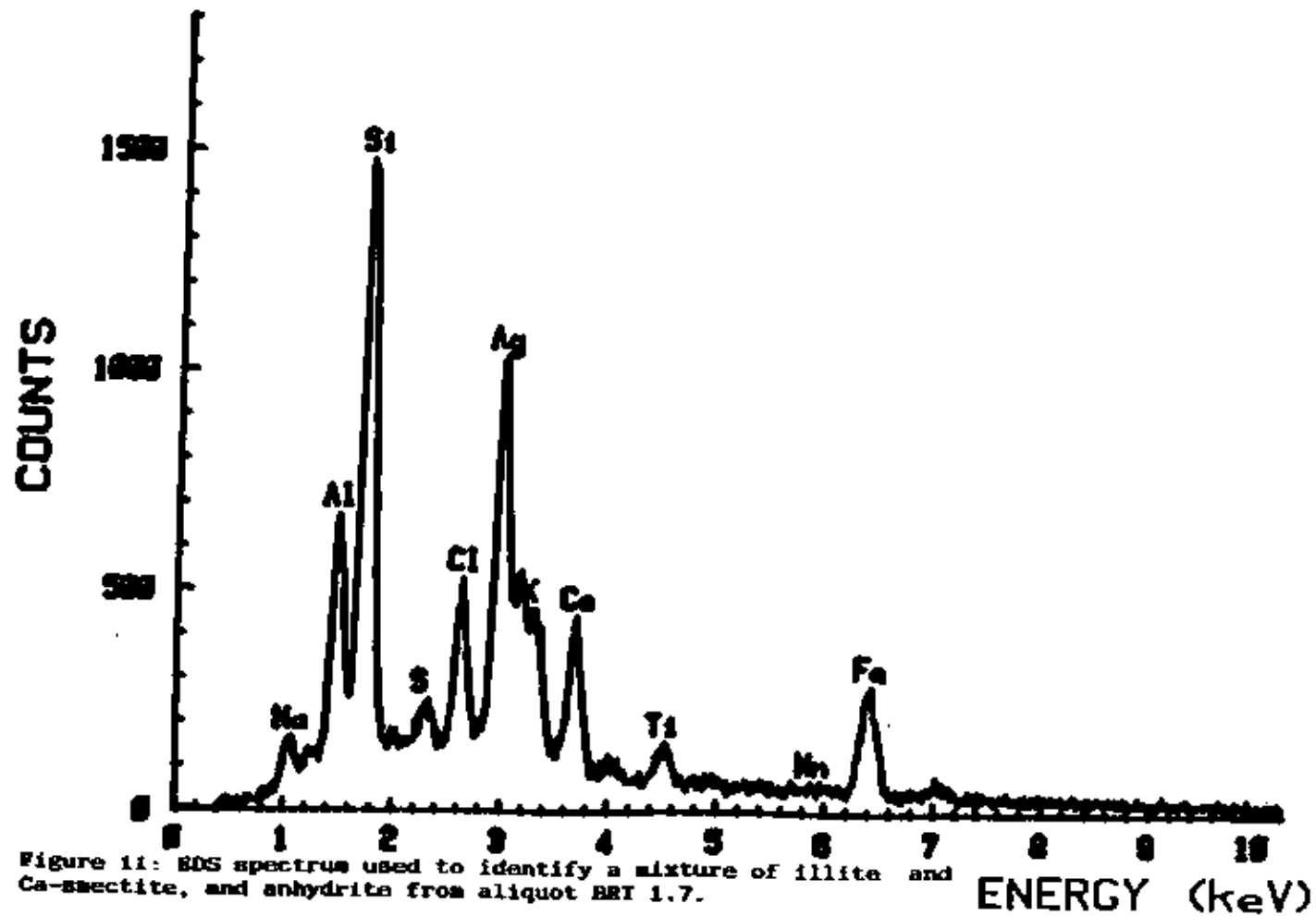


Figure 11: EDS spectrum used to identify a mixture of illite and Ca-saectite, and anhydrite from aliquot BRT 1.7.

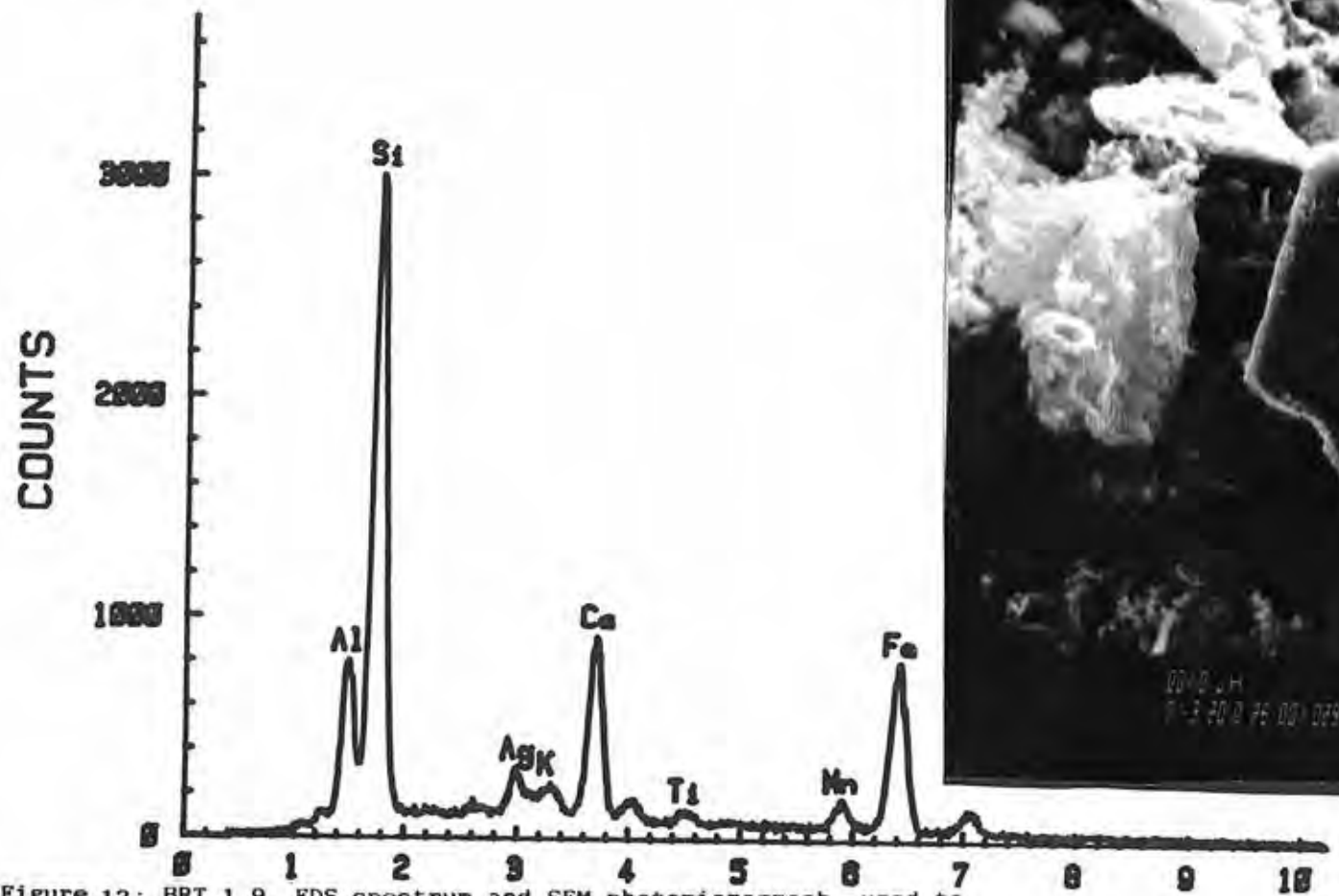


Figure 12: BRT 1.9 EDS spectrum and SEM photomicrograph used to identify Ca-smectite (whitish large mass to the left of dark grain). The smaller fine grained masses at the top (left) of the photograph were identified as illite. The dark grain is primary plagioclase.

ENERGY (keV)

that Ca was replacing other cations in smectite structures during the course of the experiment. Secondary anhydrite was identified from the BRT 1.7 aliquot (Figures 10-11). These identification results suggest that the precipitation of this mineral was responsible for removing Ca and SO_4 from solution by the 1264 hour sample. Variations in peak heights for elements in Figures 9-12, suggest that the composition of different smectite grains are not identical indicate. These smectite grains incorporated varying amounts of Na, Fe, Mn, and Ti into their structures.

EXPERIMENT BRT:1 XRD IDENTIFICATION RESULTS
(FIGURES 13-21): Figures 13-21 contain labeled X-ray diffractograms of secondary minerals removed from aliquots BRT 1.2 to BRT 1.10. The BRT 1.1 X-ray diffractogram did not produce any peaks (diffractogram therefore not included in this thesis). Figure 13 is an X-ray diffractogram of secondary minerals removed from the BRT 1.2 solution aliquot (3.3 hours). The d -spacing of the broad peak in Figure 13 was used to identify secondary smectite. Figure 13 may also contain very faint illite (001), (002), and (003) peaks. The illite peaks best match those of illite (2M₁),

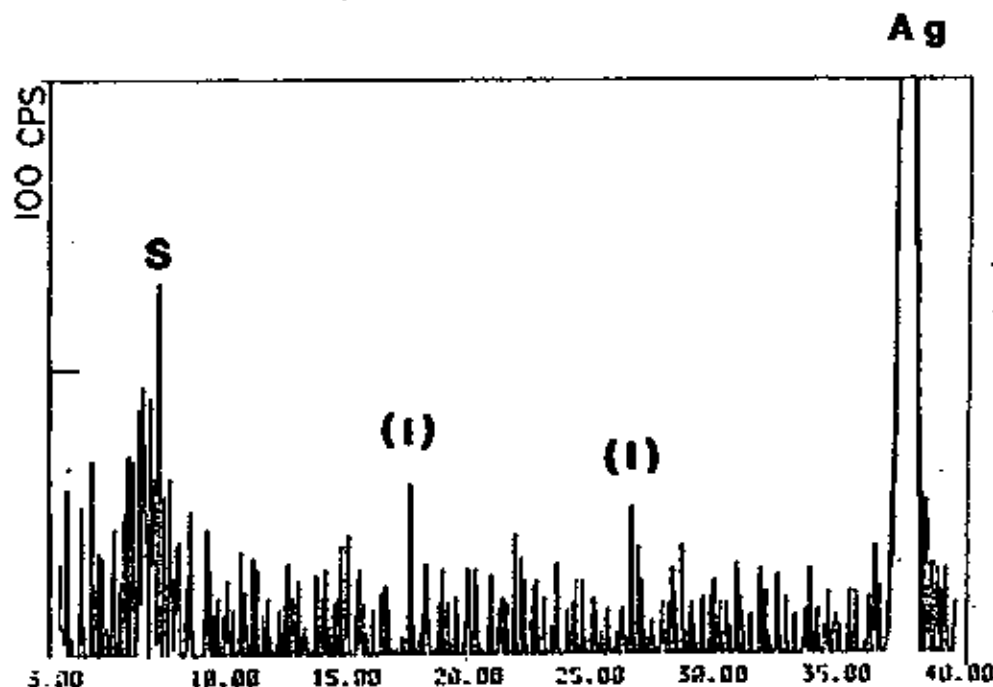
SAMPLE NAME: BRT 1.2
 TARGET : Cu
 VOL and CUR: 40KV 30mA
 SLITS : 0.05 1 RS 15 33 1
 SCAN SPEED: 10 DEG/MIN.
 STEP SIZE: 02 DEG
 PRESET TIME: 0 SEC
 FILE NAME : M1851A8
 OPERATOR : GEMMYER
 COMMENT :

DATE: 00.04.26

SMOOTHING NO.: 9
 THRESH. INTEN.: 17 CPS
 2nd DERIV.: 2442 CPS/(DEGxDEG)
 WIDTH: 15 DEG
 B.G. (SAMP.): 52
 B.G. (CYCLE): 52
 OUTPUT FILE : M1851A8OP

2-THETA INTER 2.353 1.27 1.80

Sample Name : BRT 1.2



Ag

S-SMECTITE

I-ILLITE

Ag-SILVER

This analysis was conducted
 using CuK α , α radiation
 ($K\alpha_1 = 1.5406 \text{ \AA}$, $K\alpha_2 = 1.5443 \text{ \AA}$)
 (I) = Possible faint peak

Figure 13: X-ray diffractogram of the secondary clay fraction removed from aliquot BRT 1.2.

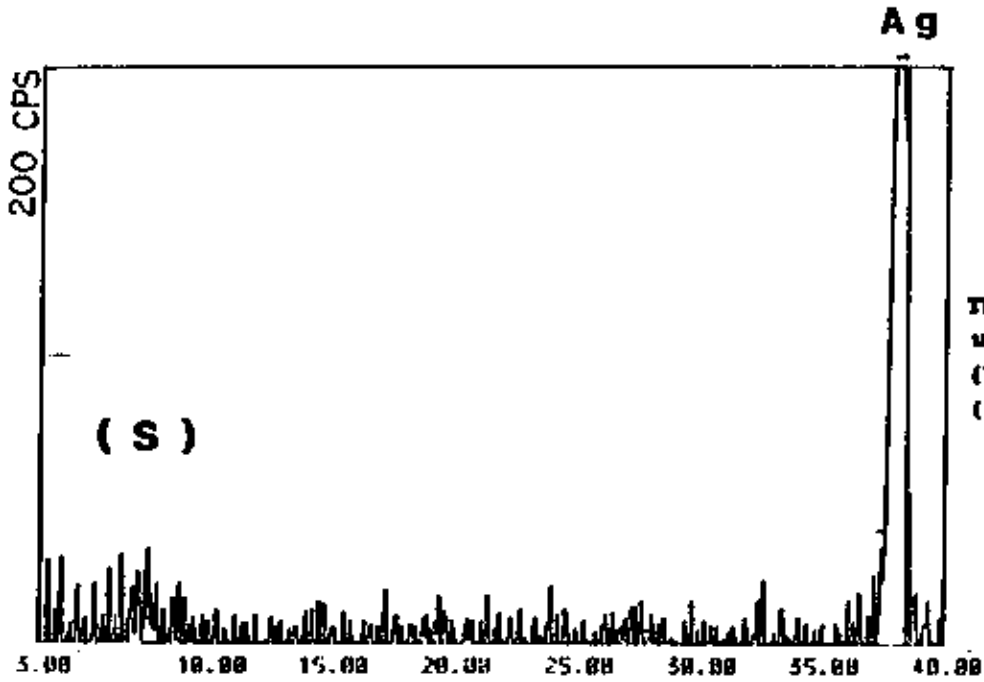
{JCPDS card no. 26-911}. In the BRT 1.3 X-ray diffractogram, (Figure 14) a faint smectite peak is discernable. In the BRT 1.4 (Figure 15) X-ray diffractogram a illite (003) peak is discernable. A less distinct broad smectite peak is also discernable. The X-ray diffractogram of secondary minerals removed from aliquot BRT 1.5 (Figure 16) contains one clearly discernable illite peak (003). The BRT 1.6 X-ray diffractogram in Figure 17 includes clearly discernable illite (001) and (003) peaks. Figure 17 also contains evidence of a distinguishable broad smectite peak. In Figure 18 (BRT 1.7) clearly discernable illite (002, 003), and smectite peaks were identified. The Figure 19 X-ray diffractogram of secondary minerals removed from the BRT 1.8 aliquot contains a faint illite (003) peak. In Figure 20 clearly distinguishable smectite and illite (002), (003) peaks were identified from the secondary mineral assemblage removed from the BRT 1.9 aliquot. In Figure 21 the secondary mineral fraction removed from aliquot BRT 1.10 produced distinct illite (001), (002), and (003) peaks (Figure 21).

SAMPLE NAME: BRT 1 S
 TREAT : Cu
 VOL. and CUR: 45KV 50mA
 SLITS : DS 1 KS .15 SS 1
 SCAN SPEED: 10 DEG/MIN.
 STOP/SAMPL: .02 DEG
 PRE-SET TIME: 0 SEC
 FILE NAME : M182100
 OPERATOR : GMYER
 COMMENT :

DATE : 08.04.26
 SMOOTHING NO. : 11
 REFRESH. INTER. : 25 CPS
 2nd DERIV. : 870 CPS/101.6*DEG
 WIDTH: .04 DEG
 B.G. (SAMP.) : 52
 B.G. (CYCLE) : 52
 OUTPUT FILE : M182100A

No.	2-Theta	INTEN.	2-Theta	INTEN.	WIDTH
1	32.12	5785	2.249	2.249	1.3
2	36.12	5785	2.249	2.249	1.3

Sample Name : BRT 1 S



Ag - SILVER
S - SMECTITE

This analysis was conducted
 using $CuK\alpha$ radiation
 ($K\alpha_1 = 1.5406 \text{ \AA}$, $K\alpha_2 = 1.5443 \text{ \AA}$)
 () = Possible faint peak

Figure 14: X-ray diffractogram of the secondary clay fraction removed from aliquot BRT 1.3.

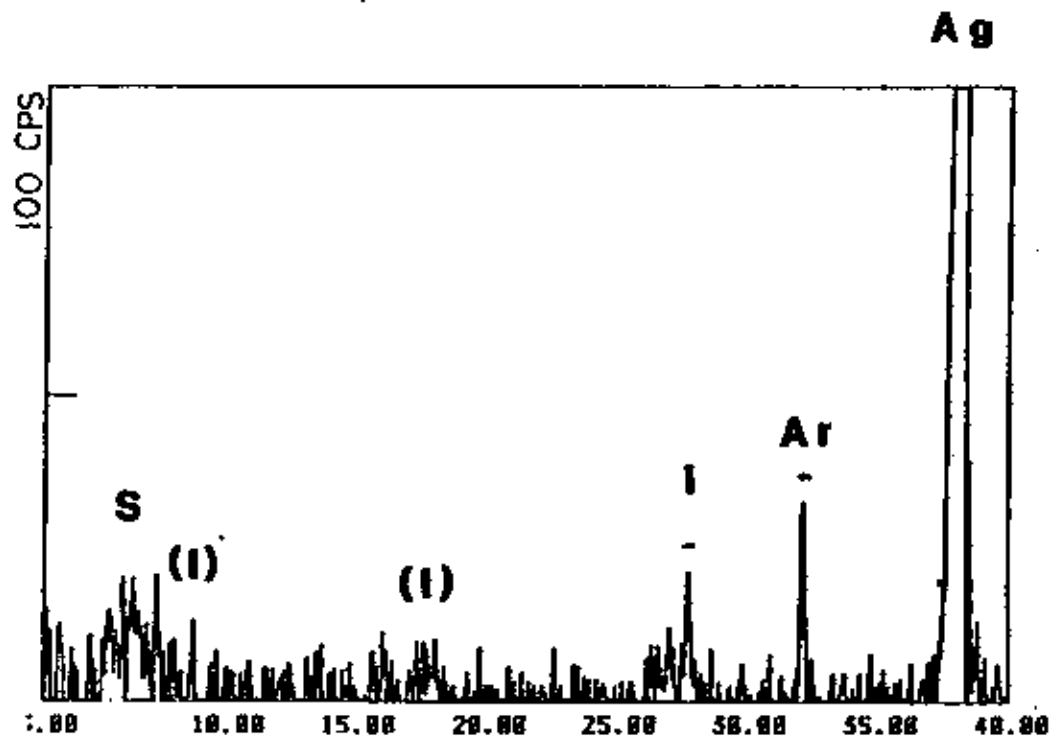
SAMPLE NAME: BRT 1.4
 TARGET : Cu
 VOL and CUR: 45KV 30mA
 SLITS : DS 1 RS .15 SS 1
 SCAN SPEED: 10 DEG/MIN.
 STEP/SAMPL.: .02 DEG
 PRESET TIME: 0 SEC
 FILE NAME : M181100
 OPERATOR : GMYER
 COMMENT :

DATE: 90.04.26

SMOOTHING NO.: 11
 THRESH. INTEN.: 24 CPS
 2nd DERIV.: 070 CPS/(DEG*DEG)
 WIDTH: .04 DEG
 B.G. (SAMP.): 52
 B.G. (CYCLE): 52
 OUTPUT FILE : M181100A

No.	2-Theta	INTEN.	d	WIDTH 1/10
1	27.0	142	3.296	.36
2	32.22	105	2.778	.35
3	38.1	5383	2.36	.3

Sample Name : BRT 1.4



S-SMECTITE

I-ILLITE

Ag-SILVER

Ar-SILVER

CHLORIDE

This analysis was conducted
 using $\text{CuK}\alpha_1$ radiation
 ($\lambda_1 = 1.5406 \text{ \AA}$, $\lambda_2 = 1.5443 \text{ \AA}$)
 () = Possible faint peak

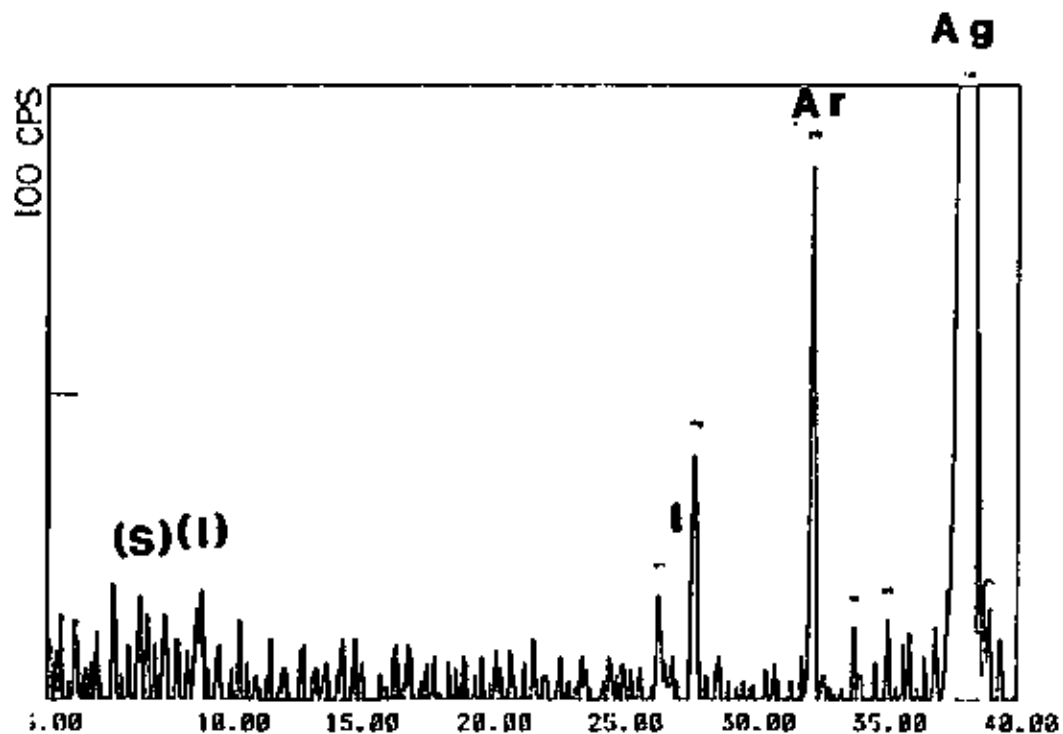
Figure 15: X-ray diffractogram of the secondary clay fraction removed from aliquot BRT 1.4.

SAMPLE NAME: BRT 1.5
 TARGET : Cu
 VOL and CUR: 45KV 30mA
 SLITS : DS 1 RS .15 SS 1
 SCAN SPEED: 10 DEG/MIN.
 STEP/SAMPL: .02 DEG
 PRESET TIME: 0 SEC
 FILE NAME : M180100
 OPERATOR : GMYER
 COMMENT :

DATE: 90.04.26
 SMOOTHING NO.: 17
 THRESH. INTEN.: 12 CPS
 2nd DERIV.: 95 CPS/(DEGxDEG)
 WIDTH: .14 DEG
 B.G. (SAMP.): 32
 B.G. (CYCLE): 32
 OUTPUT FILE : M18010P

No.	Th	Inten	Width	1/10
1	Ag	48		18
2	Ar			

Sample Name : BRT 1.5



S-SMECTITE
 I-ILLITE
 Ag-SILVER
 Ar-SILVER
 CHLORIDE

This analysis was conducted
 using $\text{CuK}\alpha$, α radiation
 ($\lambda_{K\alpha} = 1.5406 \text{ \AA}$, $\lambda_{K\beta} = 1.5443 \text{ \AA}$)
 () = Possible faint peak

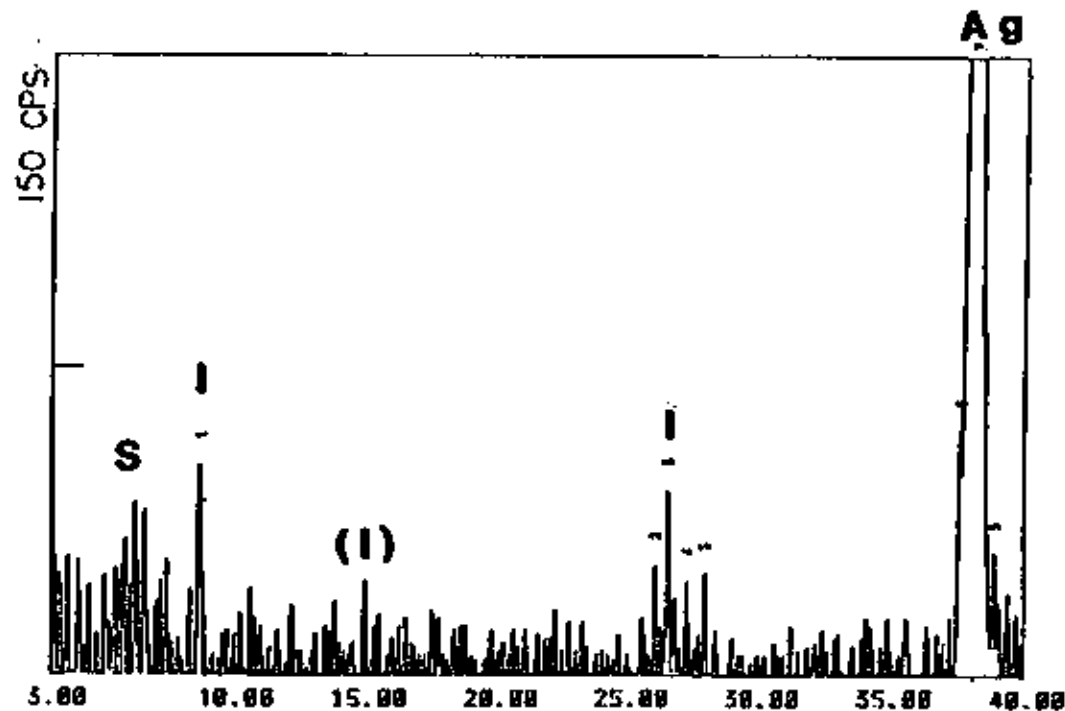
Figure 16: X-ray diffractogram of the secondary clay fraction removed from aliquot BRT 1.5.

SAMPLE NAME: BRT 1.6
 TARGET : Cu
 VOL and CUR: 45KV 30mA
 SLITS : DS 1 AS .15 SS 1
 SCAN SPEED: 10 DEG/MIN.
 STEP/SAMPL.: .02 DEG
 PRESET TIME: 0 SEC
 FILE NAME : M179100
 OPERATOR : GHWYER
 COMMENT :

DATE: 90.04.26
 SMOOTHING NO.: 9
 THRESH. INTEN.: 21 CPS
 2nd DERIV.: 2442 CPS/(DEGxDEG)
 WIDTH: .09 DEG
 B.G. (SAMP.) : 52
 B.G. (CYCLE) : 32
 OUTPUT FILE : M179100P

No.	2-Theta	INTEN.	WIDTH
1	10.00	100	0.10
2	15.00	100	0.10
3	26.00	100	0.10
4	38.00	100	0.10

Sample Name : BRT 1.6



I-ILLITE
Ag-SILVER

This analysis was conducted
 using $CuK\alpha_1$ radiation
 ($K\alpha_1 = 1.5406 \text{ \AA}$, $K\alpha_2 = 1.5443 \text{ \AA}$)
 () = Possible faint peak

Figure 17: X-ray diffractogram of the secondary clay fraction removed from aliquot BRT 1.6.

SAMPLE NAME: BRT 1.7
 TARGET : Cu
 VOL and CUR: 45KV 30mA
 SLITS : 05 I RS .15 SS I
 SCAN SPEED: 10 DEG/MIN.
 STEP/SAMPL.: .02 DEG
 PRE SLIT TIME: 0 SEC
 FILE NAME : M178100
 OPERATOR : GUYLER
 COMMENT :

DATE: 98.04.26
 SMOOTHING NO.: 9
 FRESH. INTEN.: 21 CPS
 2nd DERIV.: 2442 CPS/(DEG*DEG)
 WIDTH: .09 DEG
 B.G. (SAMP.) : 32
 B.G. (CYCLE1) : 32
 OUTPUT FILE : M178100P

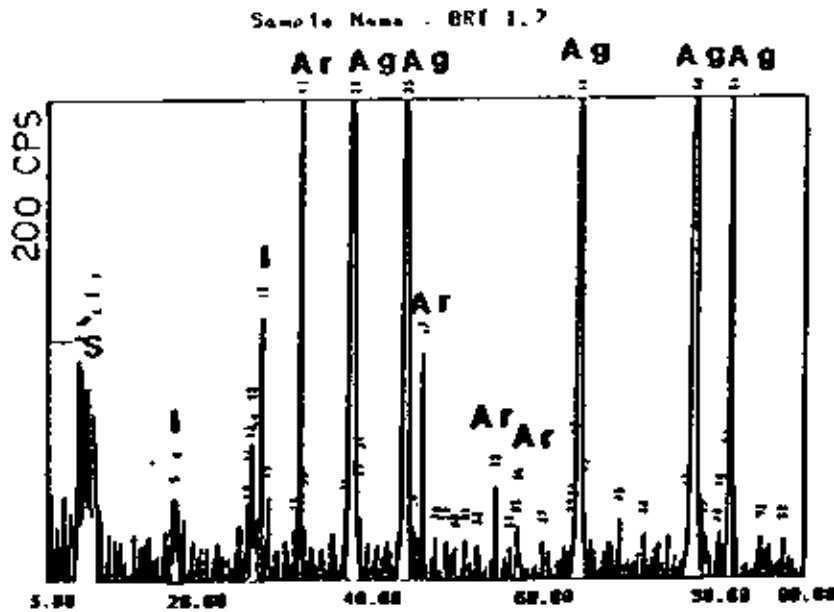
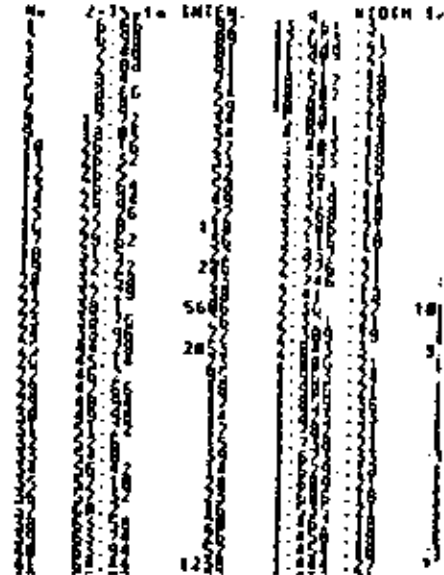


Figure 10: X-ray diffractogram of the secondary clay fraction removed from aliquot BRT 1.7.



ILLITE
 Ag-SILVER
 Ar-SILVER
 CHLORIDE

This analysis was conducted
 using $\text{CuK}\alpha$ radiation
 ($\lambda = 1.5406 \text{ \AA}$, $\text{K}\alpha_1 = 1.5443 \text{ \AA}$)

SAMPLE NAME: BRT 1.0
 TARGET : Cu
 VOL and CUR: 45KV 50mA
 SLITS : DS 1 RS .15 SS 1
 SCAN SPEED: 10 DEG/MIN.
 STEP/SAMPL: .02 DEG
 PRESET TIME: 0 SEC
 FILE NAME : M177100
 OPERATOR : GUYER
 COMMENT :

DATE: 98.04.26
 SMOOTHING NO.: 11
 THRESH. INTEN.: 15 CPS
 2nd DERIV.: 870 CPS/(DEG*DEG)
 WIDTH: .09 DEG
 B.G. (SRMP.): 32
 B.G. (CYCLE): 32
 OUTPUT FILE : M177100P

Sample Name : BRT 1.0

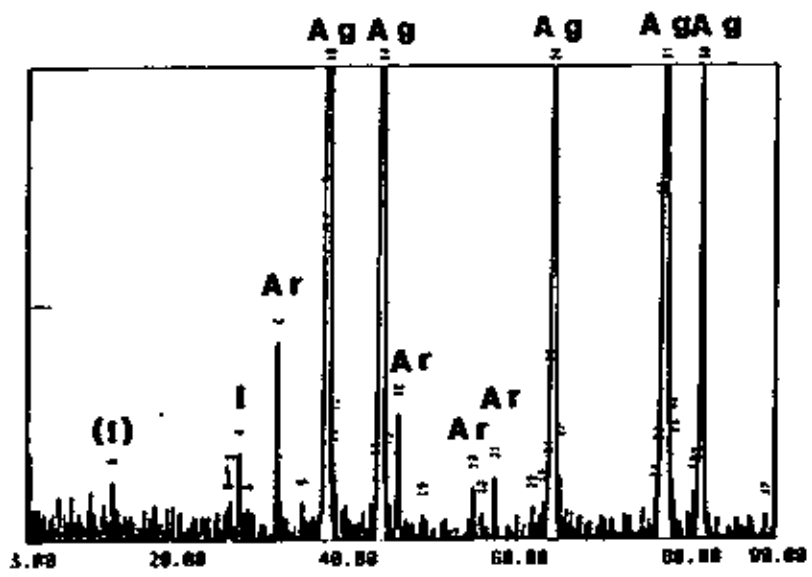
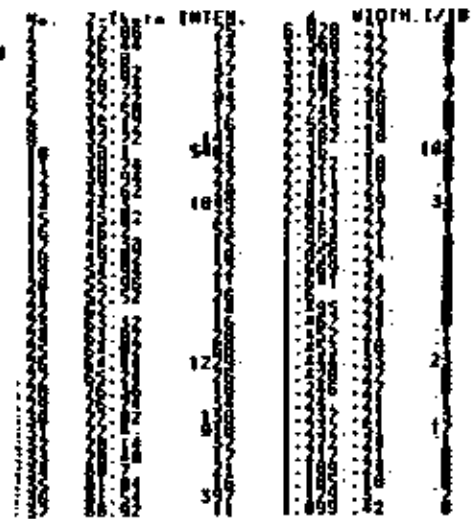


Figure 19: X-ray diffractogram of the secondary clay fraction removed from aliquot BRT 1.0.



I-ILLITE
Ag-SILVER
Ar-SILVER
CHLORIDE

This analysis was conducted using CuK α radiation (K α_1 =1.5406 Å, K α_2 =1.5443 Å)

(1) = Possible faint peak

SAMPLE NAME: BR7 1.9 DATE: 98.04.23
 TARGET : Cu SMOOTHING NO.: 9
 VOL and CUR: 45KV 50mA FRESH. INTEN.: 26 CPS
 SLITS : 0.5 (RS .15 SS 1) 2nd DERIV.: 2442 CPS/(DEG*DEG)
 SCAN SPEED: 10 DEG/MIN. WIDTH: .09 DEG
 STEP/SAMPL.: .02 DEG B.G. (SAMP.): 32
 PULSE TIME: 0 SEC B.G. (CYCLE): 52
 FILE NAME : M166100 OUTPUT FILE : M166100P
 OPERATOR : RICARDU
 COMMENT :

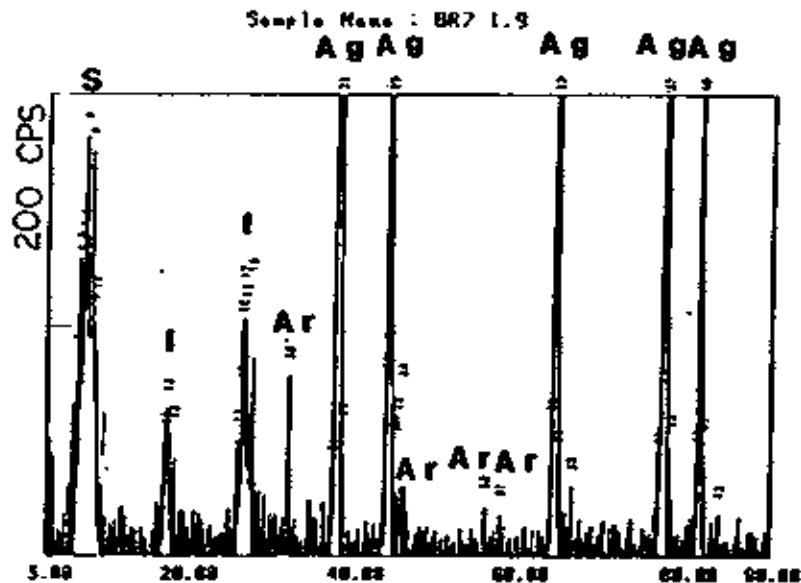
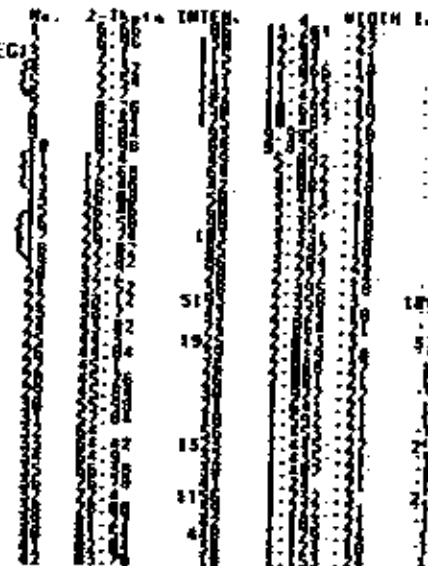


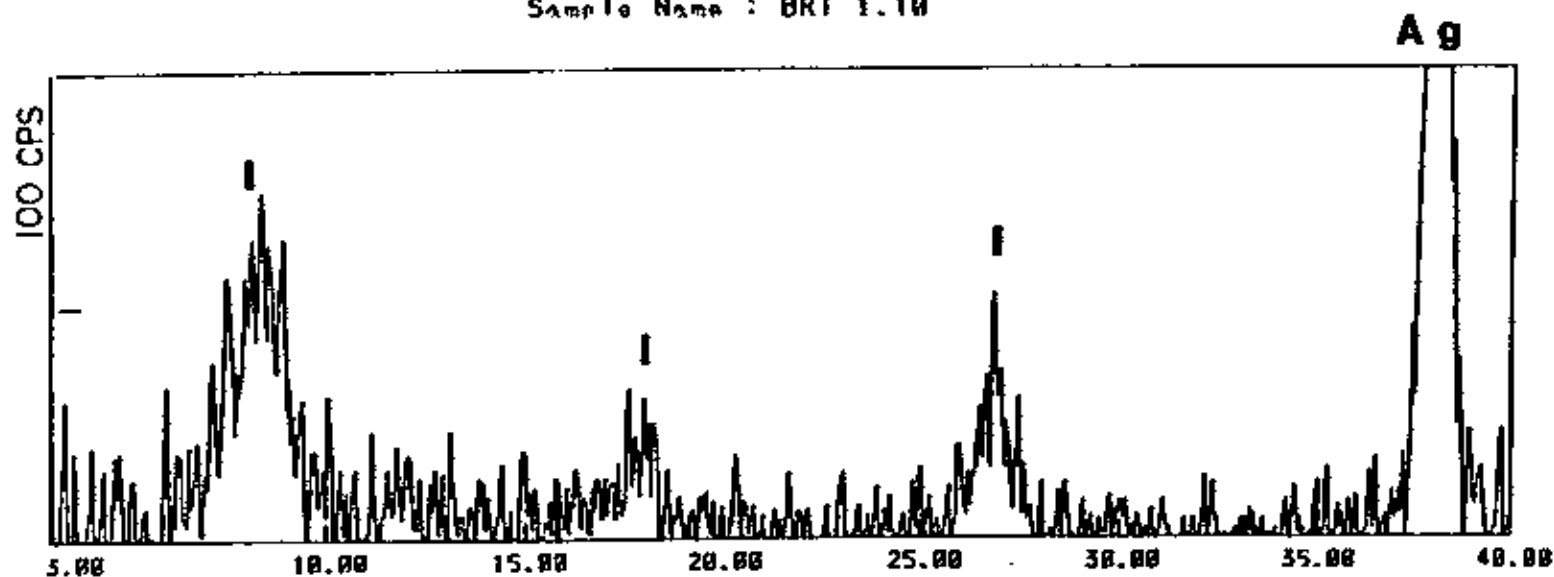
Figure 20: X-ray diffractogram of the secondary clay fraction removed from aliquot BR7 1.9.



I-ILLITE
 S-SMECTITE
 Ag-SILVER
 Ar-SILVER
 CHLORIDE

This analysis was
 conducted using CuK α radiation (K α = 1.5406 Å,
 K β = 1.3443 Å)

Sample Name : BRT 1.10



I-ILLITE

Ag-SILVER

This analysis was conducted using $\text{CuK}\alpha$ radiation ($K\alpha_1=1.5406\text{\AA}$, $K\alpha_2=1.5443\text{\AA}$)

Figure 21: X-ray diffractogram of the secondary clay fraction removed from aliquot BRT 1.10.

EXPERIMENT BRT:1 FURTHER XRD DATA INTERPRETATION (FIGURES 13-21): The XRD data indicate that illite was the dominant secondary mineral to precipitate from the tuff experiment solution. These results also suggest either that not enough illite had been formed within the first 30 minutes of the tuff experiment to produce discernable BRT 1.1 diffractogram peaks, or the illite and/or smectite formed within the first 30 minutes of the tuff experiment were not well crystallized and/or were not yet filterable. By the 3.3 hour sample illite and smectite had precipitated out of BRT:1 solution. It is clear that the general trend from BRT 1.1 to 1.10, is one of increasing illite and smectite peak intensity with aliquot succession. These results suggest that the mass of secondary clay minerals per unit volume of solution, and/or the degree of clay mineral crystallinity increased with time.

FIGURES 22-25: EXPERIMENT BRT:1 XRD DATA PRESENTATION (ETHYLENE GLYCOL): Figures 22-25 contain tuff X-Ray Diffractograms, (BRT 1.4, BRT 1.5, BRT 1.6, and BRT 1.10), with untreated secondary mineral data (top) and ethylene glycol treated secondary mineral data (bottom). In Figure

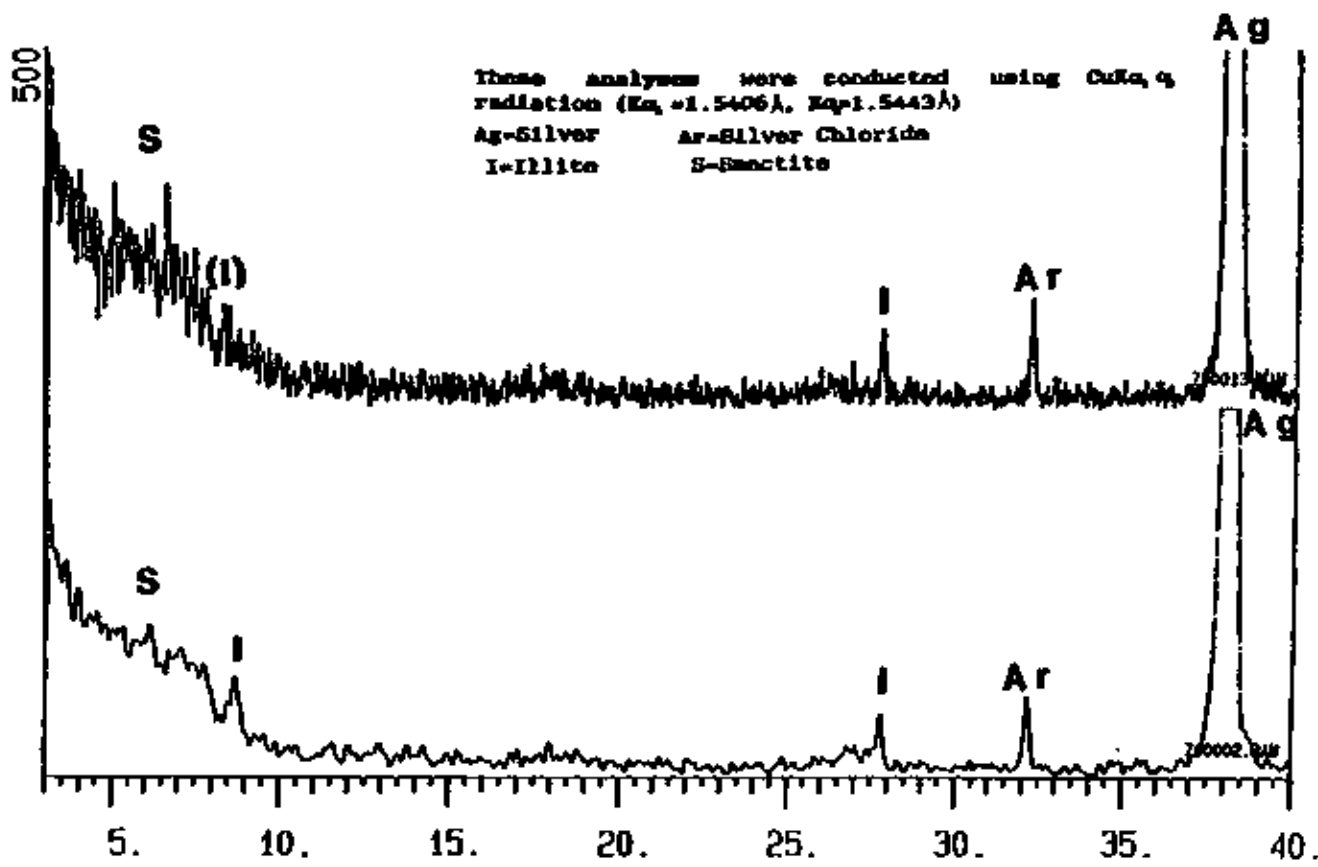


Figure 22: BRT 1.4 aliquot X-ray diffractograms used to determine the effect of ethylene glycolation treatment; unglycolated secondary mineral fraction diffractogram (top), and ethylene glycol treated secondary mineral fraction diffractogram (bottom).

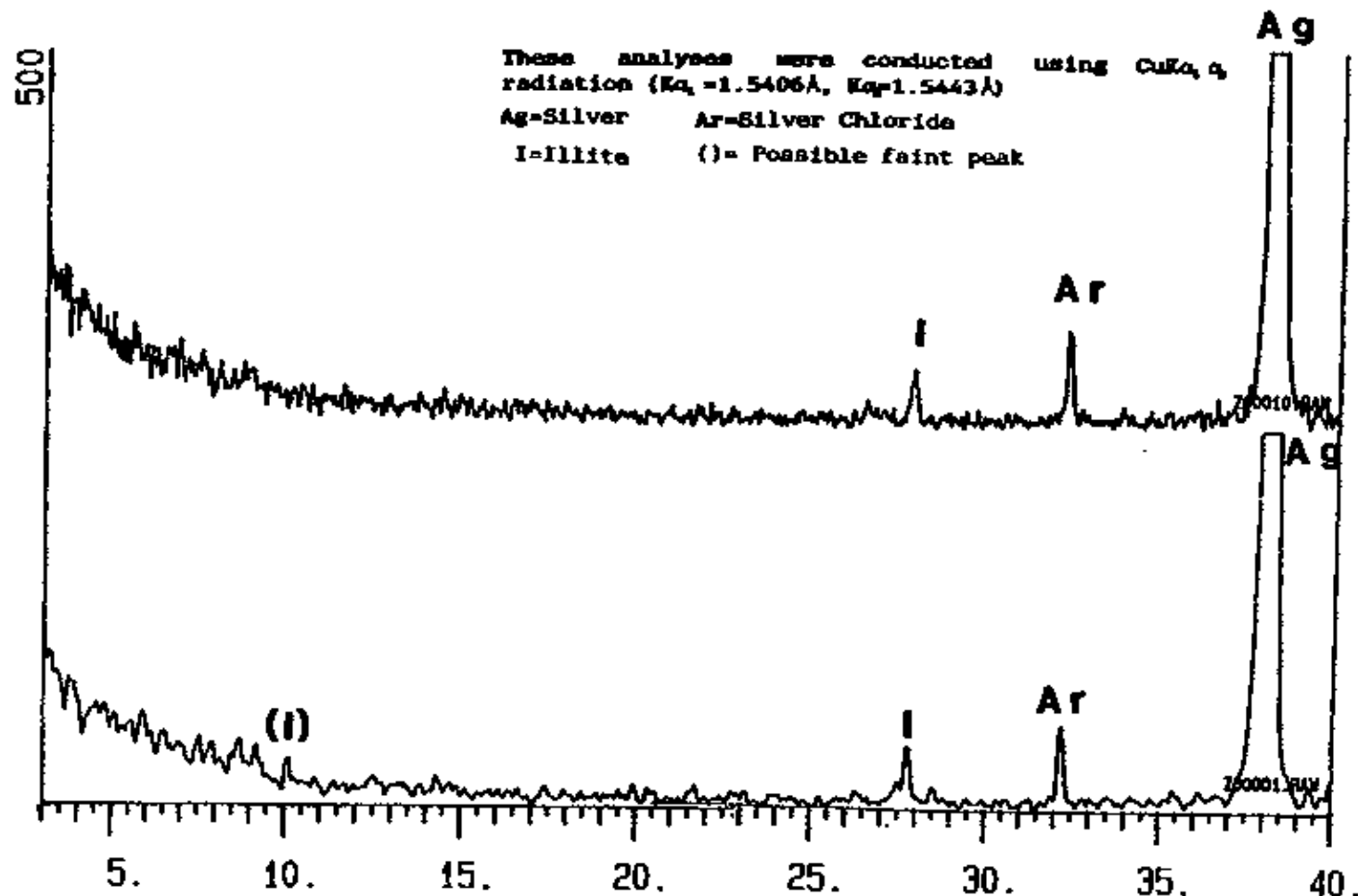


Figure 23: BRT 1.5 aliquot X-ray diffractograms used to determine the effect of ethylene glycolation treatment; unglycolated secondary mineral fraction diffractogram (top), and ethylene glycol treated secondary mineral fraction diffractogram (bottom).

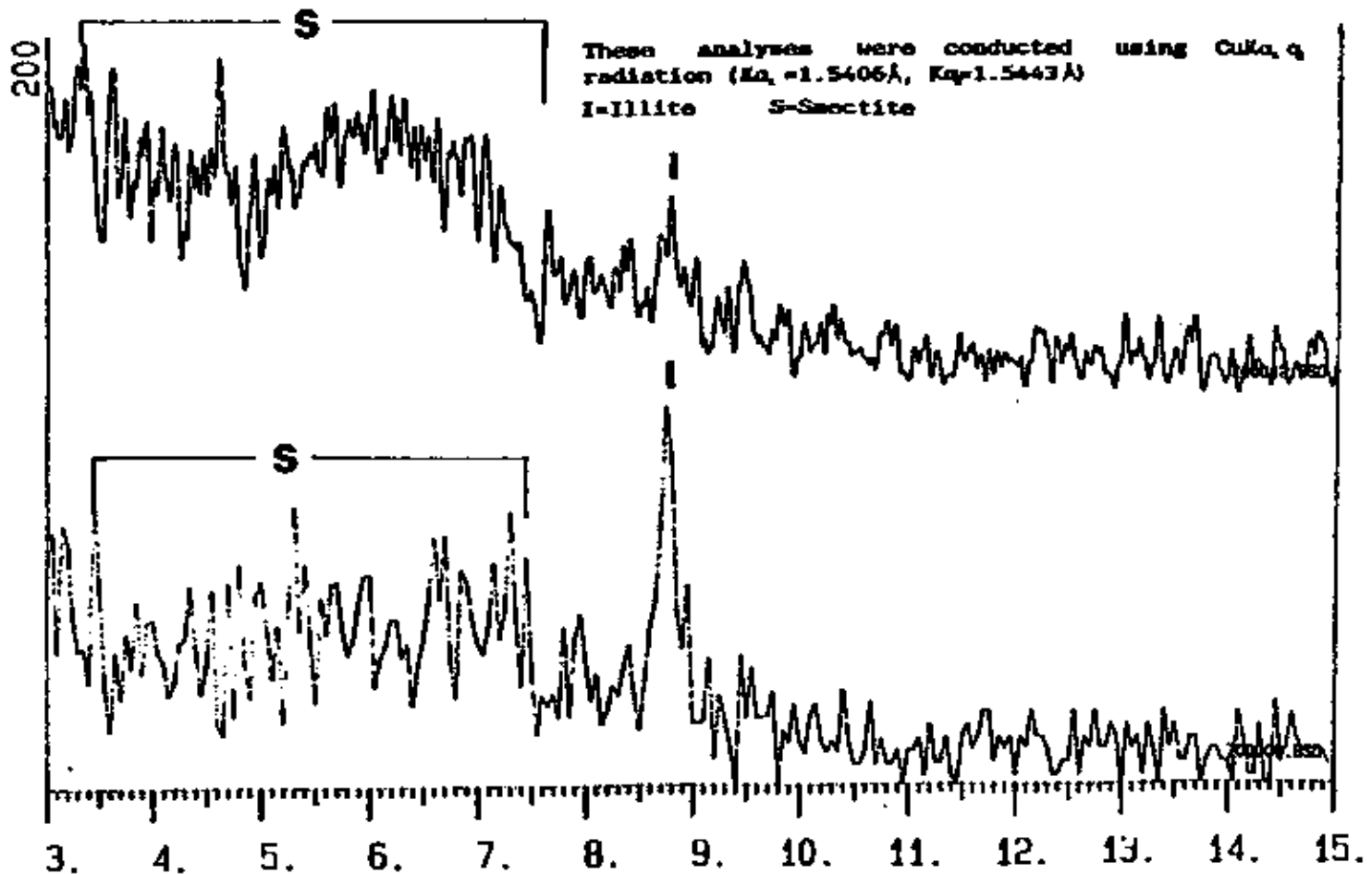


Figure 24: BRT 1.6 aliquot X-ray diffractograms used to determine the effect of ethylene glycolation treatment; unglycolated secondary mineral fraction diffractogram (top), and ethylene glycol treated secondary mineral fraction diffractogram (bottom).

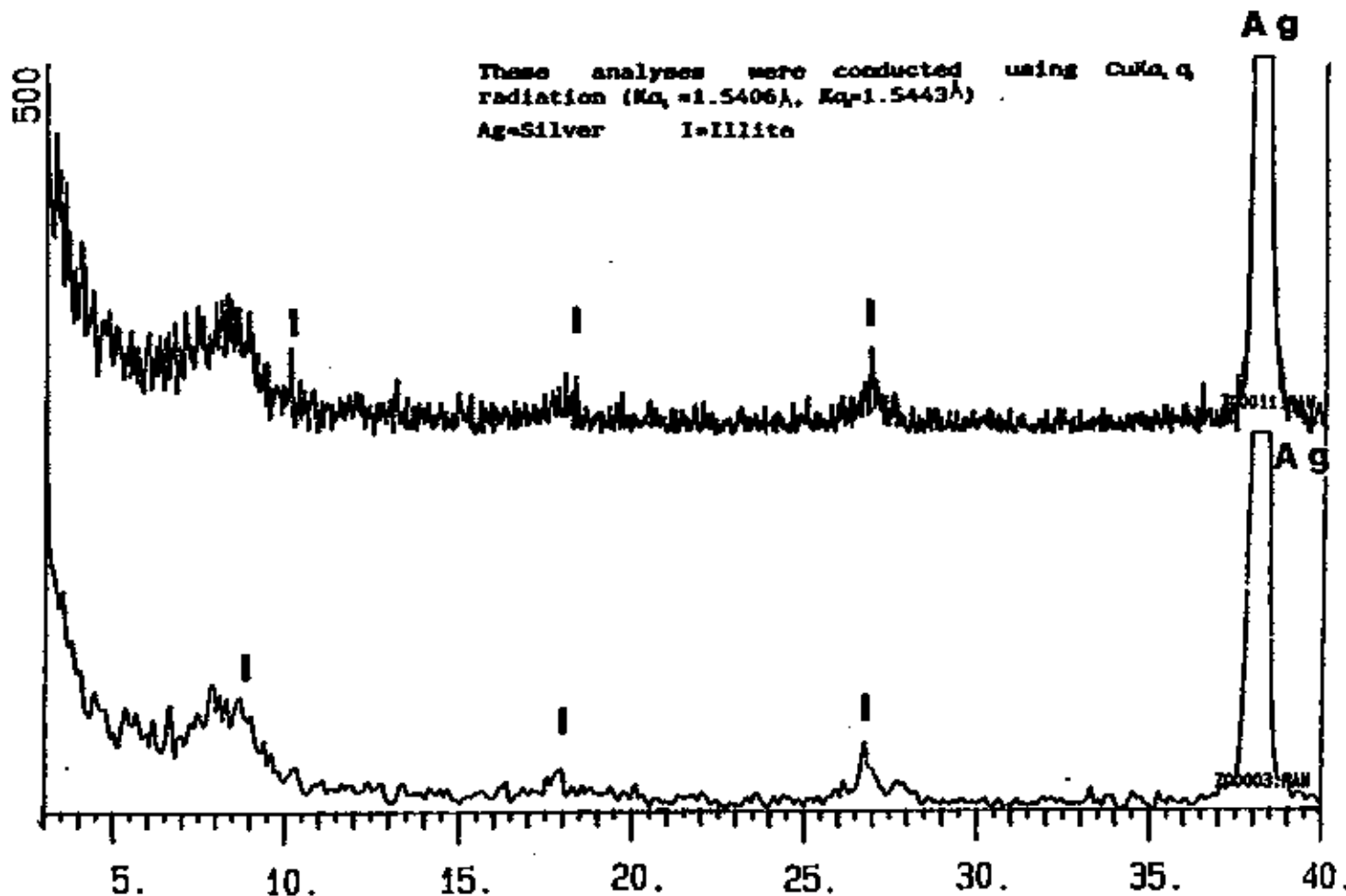


Figure 25: BRT 1.10 aliquot X-ray diffractograms used to determine the effect of ethylene glycolation treatment; unglycolated secondary mineral fraction diffractogram (top), and ethylene glycol treated secondary mineral fraction diffractogram (bottom).

22 the ethylene glycol treatment of the BRT 1.4 secondary mineral fraction resulted in a sharper illite (001) peak. The ethylene glycol treatment of the BRT 1.5 secondary mineral fraction (Figure 23) resulted in a slightly more distinct (001) illite peak. In Figure 24 the ethylene glycol treatment of the BRT 1.6 secondary mineral assemblage resulted in a clearly more distinct illite (001) peak. The smectite peak contained in the BRT 1.6 (Figure 24) untreated assemblage was widened and smoothed by the ethylene glycol treatment. The BRT 1.10 treated and untreated XRD data in Figure 25 are similar.

FIGURES 22-25: XRD DATA INTERPRETATION (ETHYLENE GLYCOL): Illite (001) peaks are slightly more distinct after the ethylene glycol treatment of the BRT 1.4 and 1.5 secondary mineral assemblages. After treatment of the BRT 1.6 secondary mineral assemblage the illite (001) peak is clearly more distinct. This comparison suggests that secondary illite was well crystallized by the 1264 hour sample. The smoothing and widening of the smectite peak after the ethylene glycol treatment of the BRT 1.6 secondary mineral assemblage, suggests that the smectites formed in the tuff experiment represent a

wide range of compositions. The surprising similarity between treated and untreated BRT 1.10 suggests that this sample was subjected to some human error in treatment, or that this assemblage did not contain smectite.

SUMMARY OF ANALYSES OF BRT:1 SECONDARY MINERALS: In summary (Table 3: Page 67), the secondary minerals identified in the tuff experiment using XRD and/or SEM/EDS techniques include illite, smectites, amorphous silica, and anhydrite. Illite was the dominant secondary mineral formed in the tuff experiment. Smectite chemical composition evolves during the experiment as Ca replaces other cations. Varying amounts of Fe, Ti, and Mn were incorporated into the illite and/or smectite structures. The smectites formed in experiment BRT:1 can be classified as beidellitic (see pH Trends vs. Time section).

GRANITE SECONDARY MINERALS

XDS/SEM IDENTIFICATION RESULTS FROM CG:1 AND CG:2 (FIGURES 26-29): Figure 26 contains a SEM photomicrograph of a large dark mineral encrusted

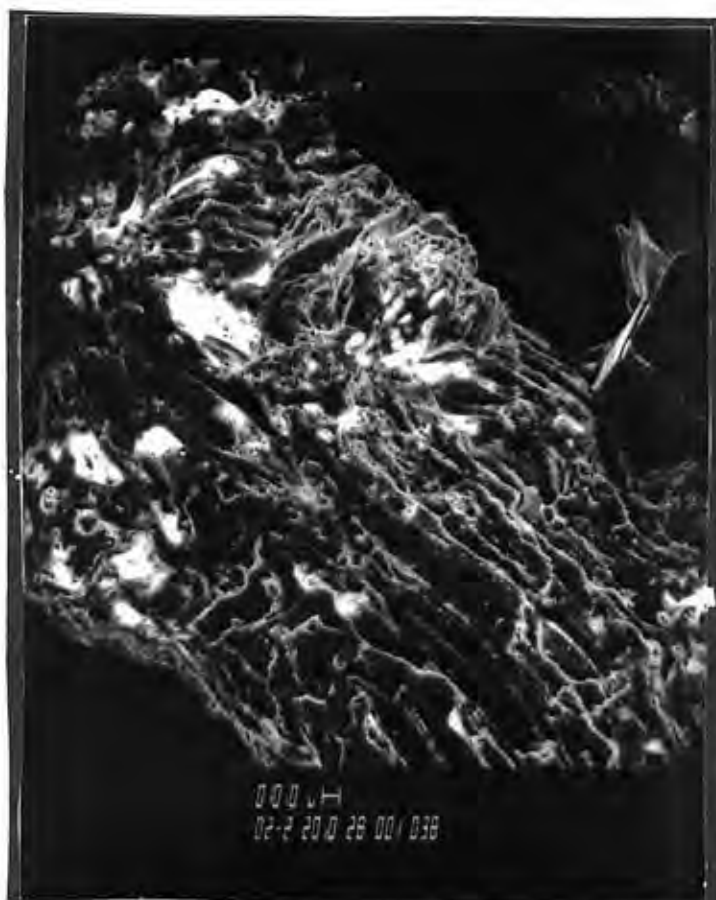


Figure 26: SEM photomicrograph showing a large dark primary K-feldspar grain encrusted by fine-grained illite (whitish) recovered from the CG:1 quench aliquot.

in places by a whitish clay mineral removed from CG:1 quench solution. On the basis of EDS spectra and morphology the white mineral was identified as illite, and the dark mineral was identified as primary K-feldspar (The EDS spectra of these minerals were not plotted). The Figure 27 EDS spectrum contains Si, Al, and Fe peaks used to identify secondary smectite removed from the CG:2 quench aliquot. The Si, Al, K, Fe, and Ti peaks contained in the CG:2 EDS spectrum (Figure 28) were used to identify a mixture of illite and smectite located on a different part of the silver filter. The Figure 29 EDS spectrum contains a large Si peak used to identify a diminutive secondary quartz grain removed from the CG:2 quench solution. Primary minerals identified from the CG:2 quench solution include microperthite, quartz, and hastingsite. In Figure 30 the included EDS spectrum was used to identify the large grain in the SEM photomicrograph as hastingsite. In summary, the secondary minerals identified from CG:1 and CG:2 quench solutions include; illite, quartz, and smectites.

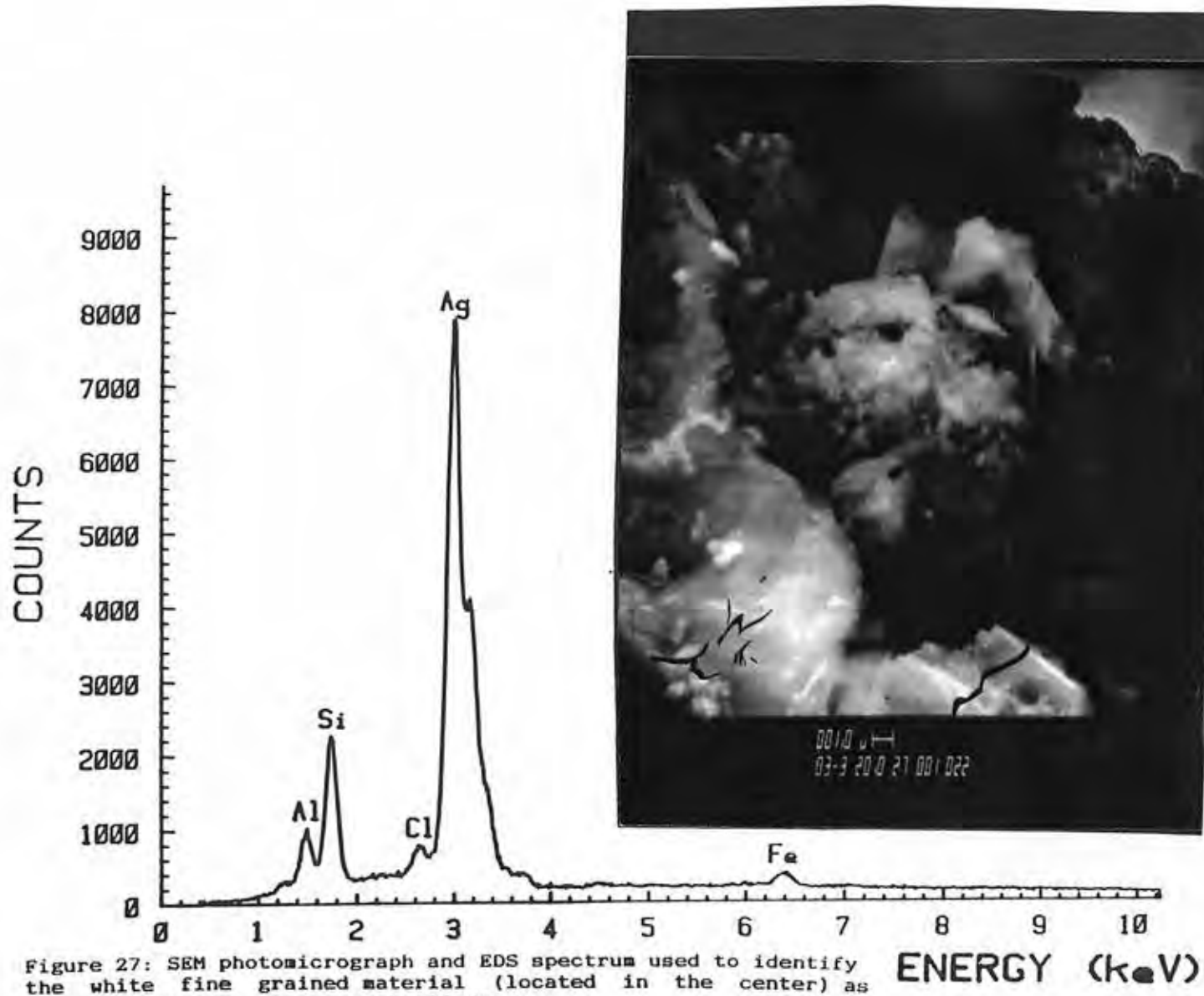


Figure 27: SEM photomicrograph and EDS spectrum used to identify the white fine grained material (located in the center) as smectite from the CG:2 quench aliquot.

ENERGY (keV)

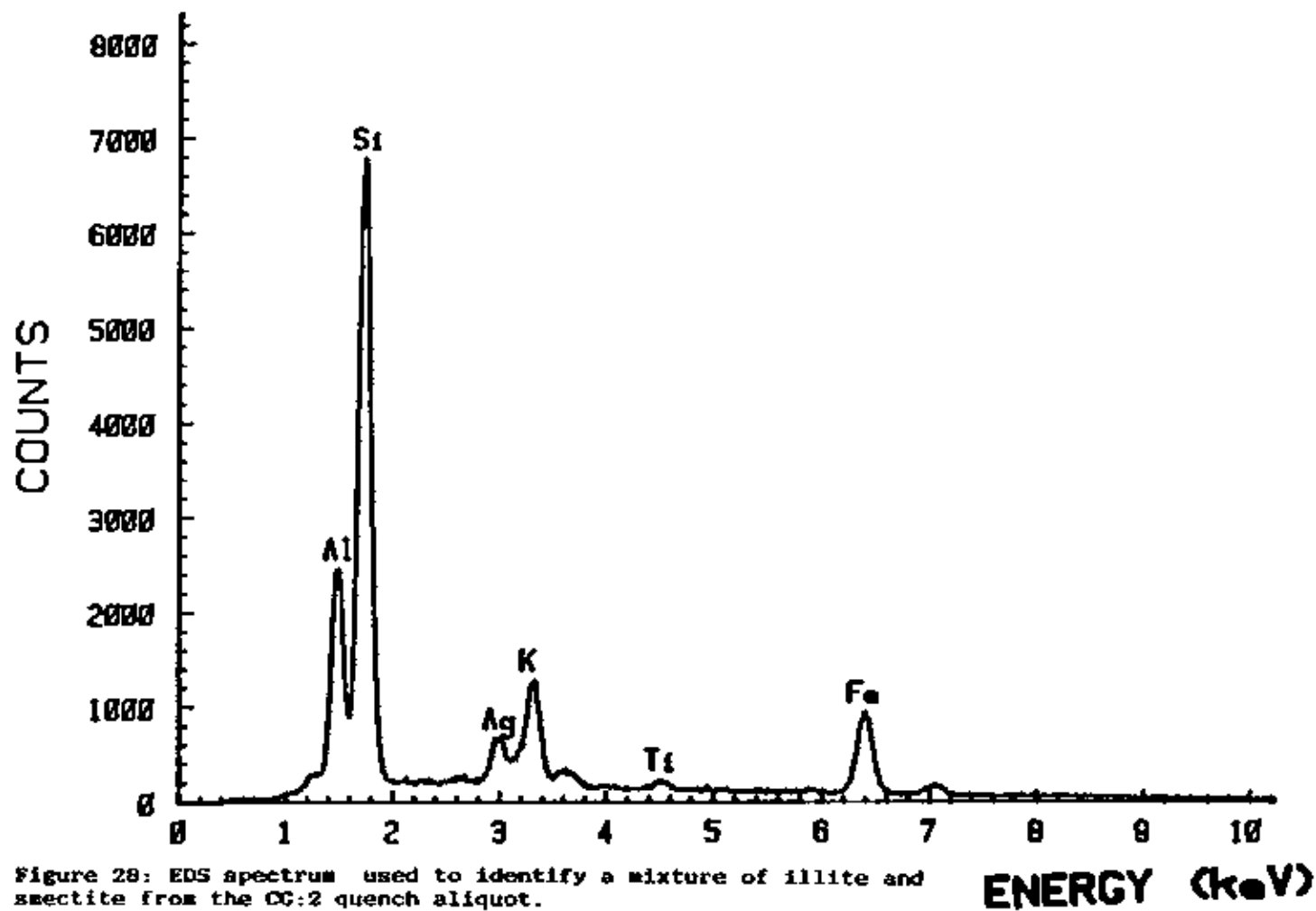
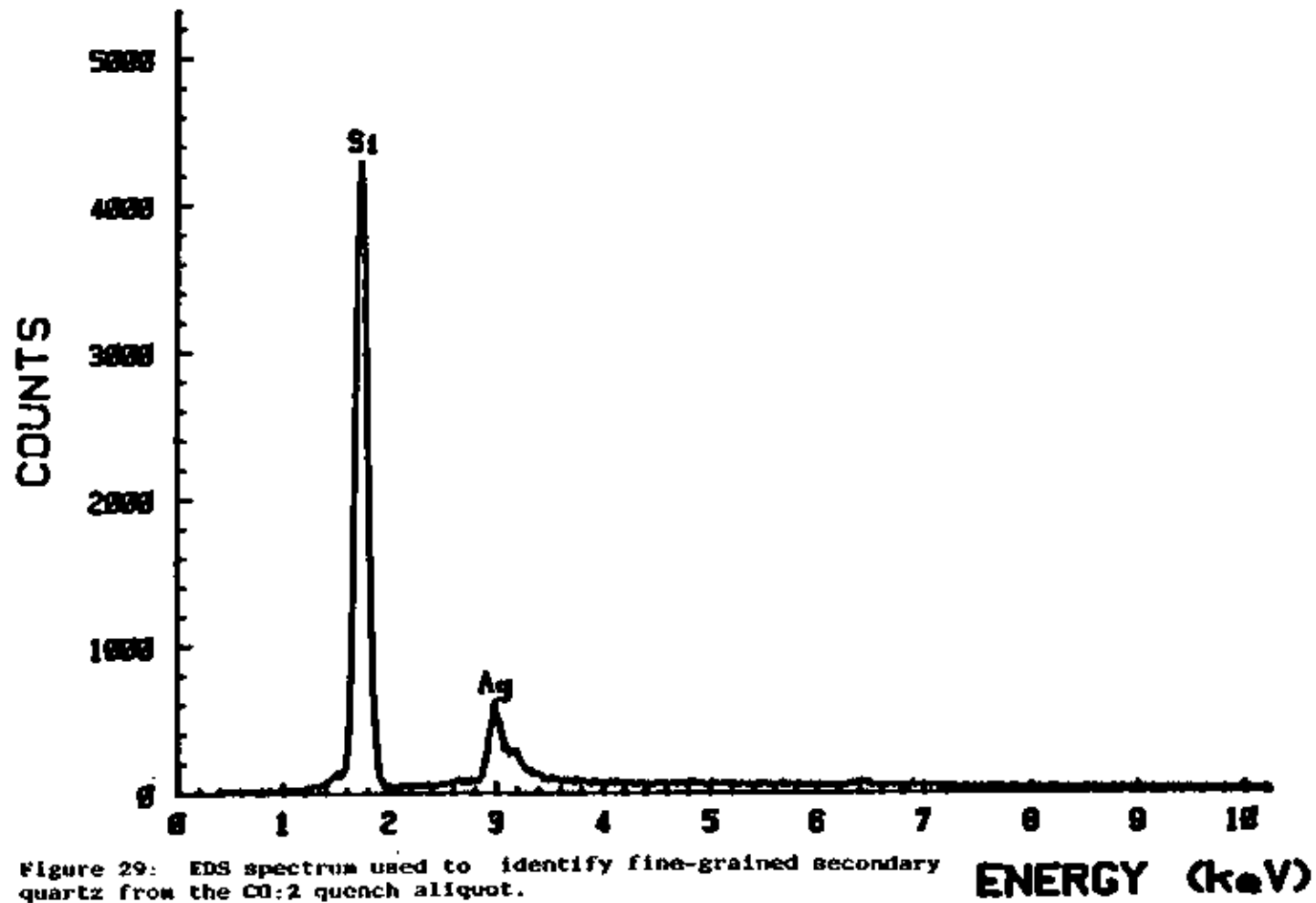


Figure 28: EDS spectrum used to identify a mixture of illite and smectite from the CC:2 quench aliquot.

LT= 60 SECS

EA70



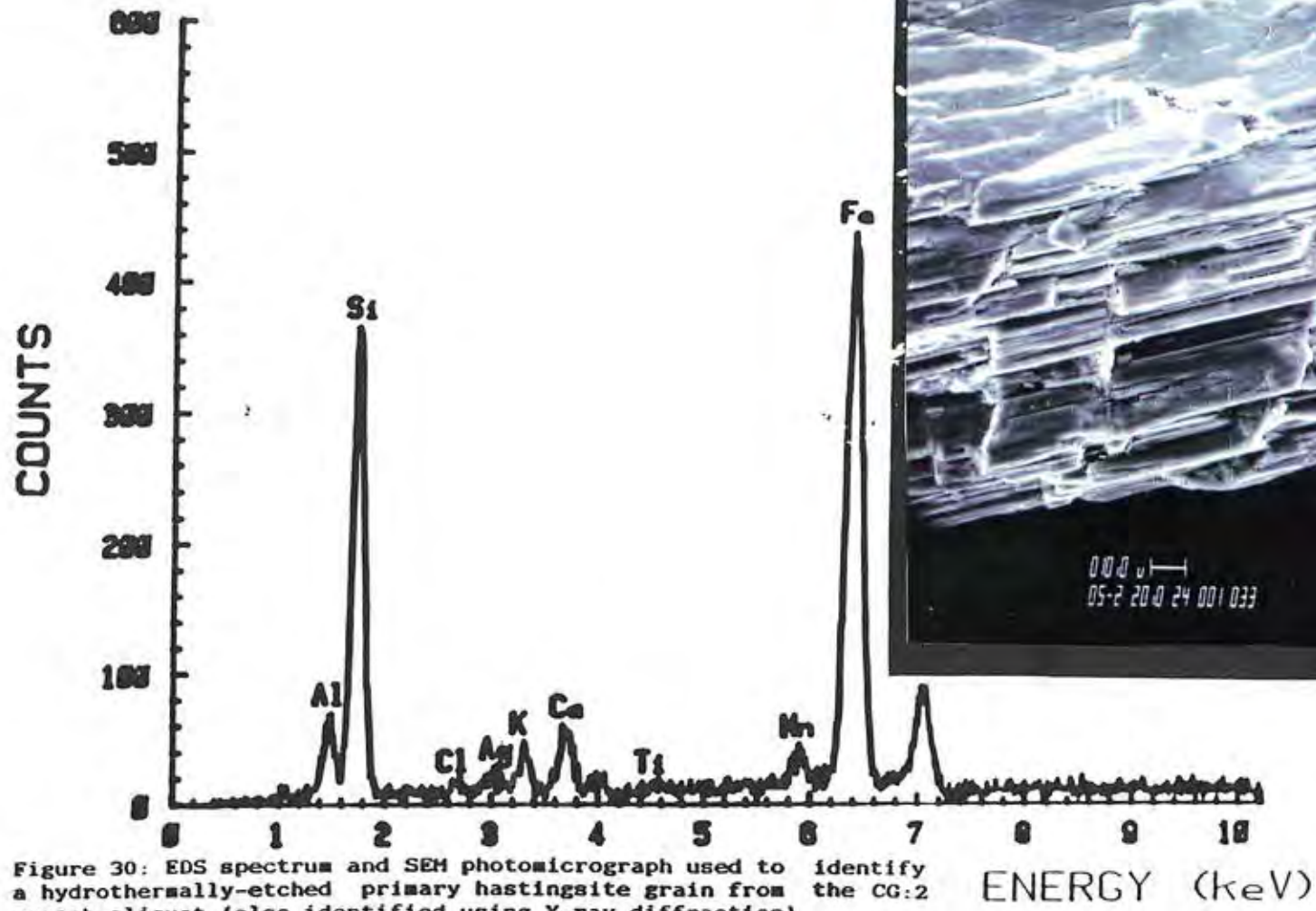


Figure 30: EDS spectrum and SEM photomicrograph used to identify a hydrothermally-etched primary hastingsite grain from the CG:2 quench aliquot (also identified using X-ray diffraction).

FIGURES 26-29: FURTHER INTERPRETATION OF CG:1 AND CG:2 EDS/SEM DATA: The Fe and Ti peaks contained within the EDS spectra in Figure 27-28, suggest that small amounts of Fe and Ti were incorporated into clay mineral structures (illite and/or smectite). The identification of secondary quartz from the CG:2 quench aliquot (Figure 29) suggests that secondary quartz formation controlled dissolved SiO₂ concentrations in this experiment.

FIGURES 31-32: XRD IDENTIFICATION RESULTS FROM EXPERIMENTS CG:1 AND CG:2: Figure 31 is a labeled X-ray diffractogram of the secondary and primary minerals recovered from the CG:1 quench aliquot. Secondary minerals identified from the CG:1 quench aliquot include: illite, quartz, albite and hematite. The d-spacings of the Figure 31 albite peaks do not match those of the primary albite peaks contained in Figure 6a. However the d-spacings of Figure 31 albite peaks match those of high albite (JCPDS card no. 20-572) to within 0.01 Å. The illite peak d-spacings best match those of illite (2M₁) (JCPDS card no. 26-911). Hastingsite and microcline are believed to be primary since they have identical d-spacings when compared with peaks produced by the granite primary material

200 CPS

This analysis was conducted using $\text{CuK}\alpha_1$ radiation ($K\alpha_1 = 1.5406\text{\AA}$, $K\alpha_2 = 1.5443\text{\AA}$)

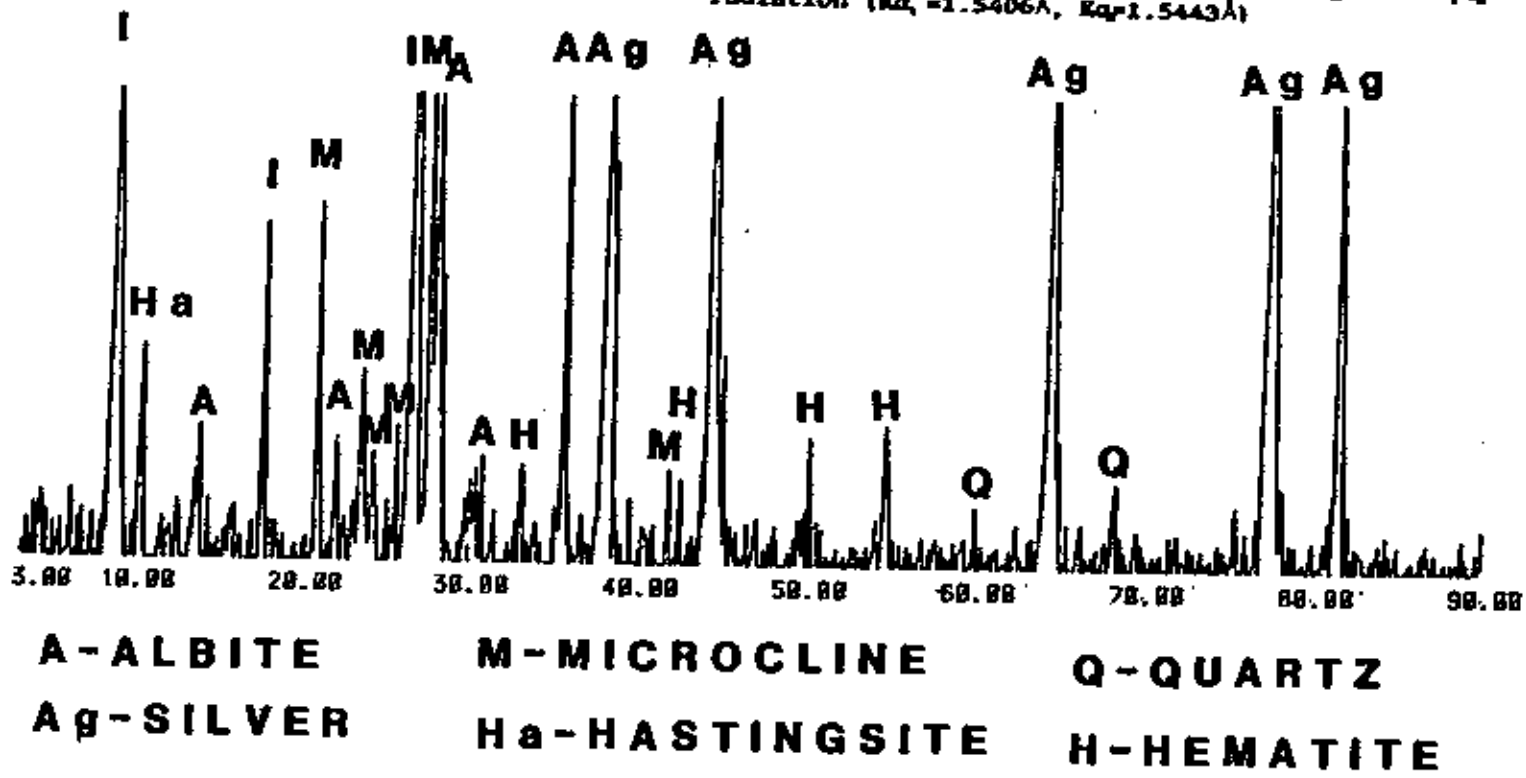


Figure 31: X-ray diffractogram of secondary and primary minerals removed from the CG:1 quench aliquot.

This analysis was conducted using $\text{CuK}\alpha_1$ radiation ($\lambda_1=1.5406\text{\AA}$, $\lambda_2=1.5443\text{\AA}$)

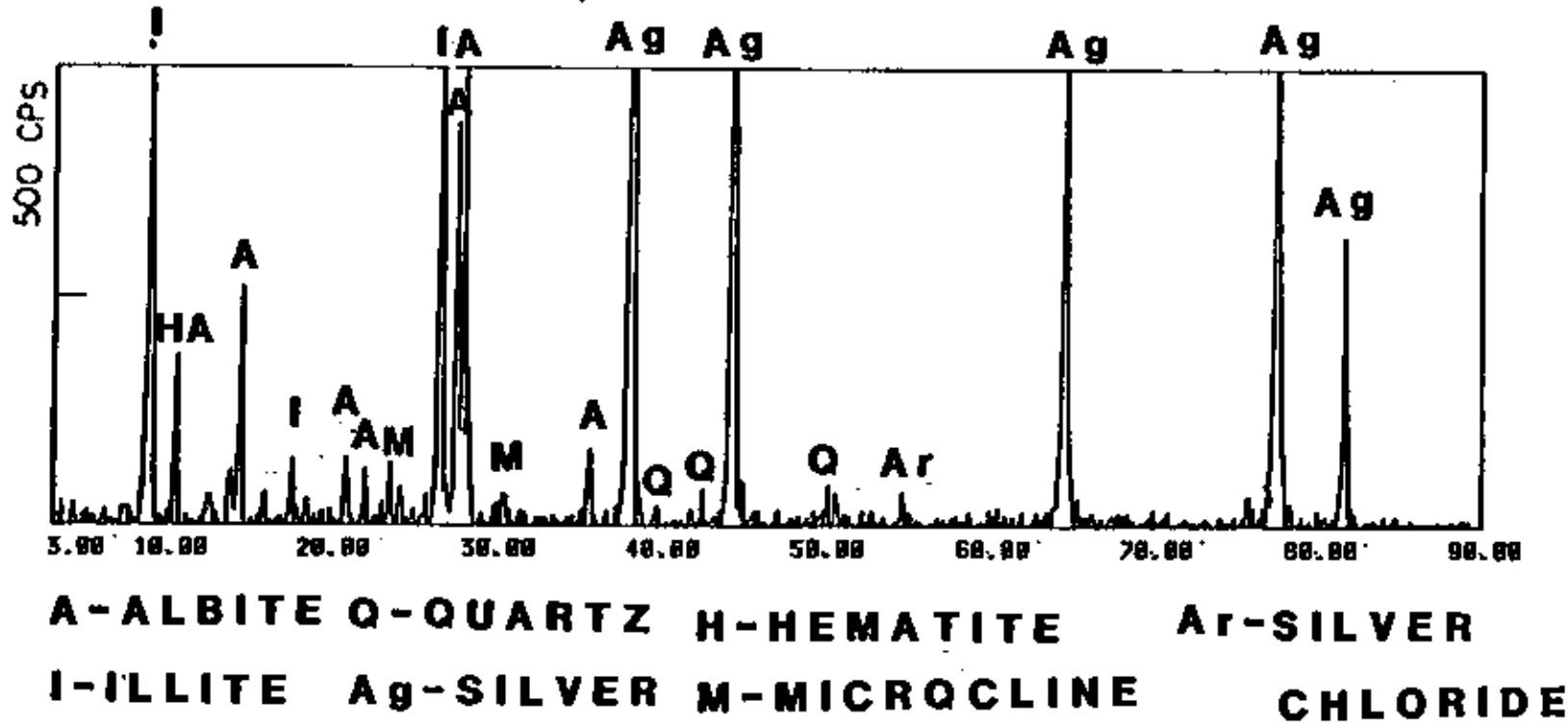


Figure 32: X-ray diffractogram of secondary and primary minerals removed from the CU:2 quench aliquot.

(Figure 6a). Secondary illite, quartz, and high albite were also identified from the CG:2 quench solution (Figure 32). Primary hastingsite and microcline are also identified in the CG:2 diffractogram (Figure 32).

FIGURES 31-32: FURTHER INTERPRETATION OF CG:1 AND CG:2 XRD DATA: The CG:1 and CG:2 quench secondary mineral data clearly indicate that illite was the dominant secondary mineral formed in the granite experiments. Hematite was identified in the secondary assemblage removed from the CG:1 experiment quench solution (terminated after 108 hours). A visual examination of the CG:1 mineral assemblage reveals a thin red hematite coating. However hematite was not identified in the secondary mineral assemblage removed from the CG:2 quench solution (terminated after 2762 hours). No red hematite coating can be seen on the CG:2 mineral assemblage. This comparison suggests that as O_2 was removed from the CG:2 autoclave solution, secondary hematite became unstable. The Fe released by the dissolution of secondary hematite was probably incorporated into secondary illite and/or smectites.

FIGURES 33-34: EXPERIMENTS CG:1 AND CG:2 XRD DATA PRESENTATION (ETHYLENE GLYCOL): The ethylene glycolation of the CG:1 and CG:2 quench minerals produced no discernable smectite peaks.

FIGURES 33-34: EXPERIMENTS CG:1 AND CG:2 XRD DATA INTERPRETATION (ETHYLENE GLYCOL): The CG:1 and CG:2 quench smectites identified using SEM/EDS are poorly crystallized and/or sparse.

SUMMARY OF ANALYSES OF CG:2 SECONDARY MINERALS: In summary (Table 3: Page 67), the secondary minerals identified in the granite experiment using XRD and/or SEM/EDS include illite, high albite, quartz, and smectite. Illite was clearly the dominant secondary mineral to form from the granite autoclave solutions. Varying amounts of Fe and Ti were incorporated into illite and/or smectite structures. The smectites formed in experiments CG:1 and CG:2 can be classified as beidellitic (see pH Trends vs. Time section).

This analysis was conducted using $\text{CuK}\alpha$, θ radiation ($\lambda_1 = 1.5406 \text{ \AA}$, $\lambda_2 = 1.5443 \text{ \AA}$)

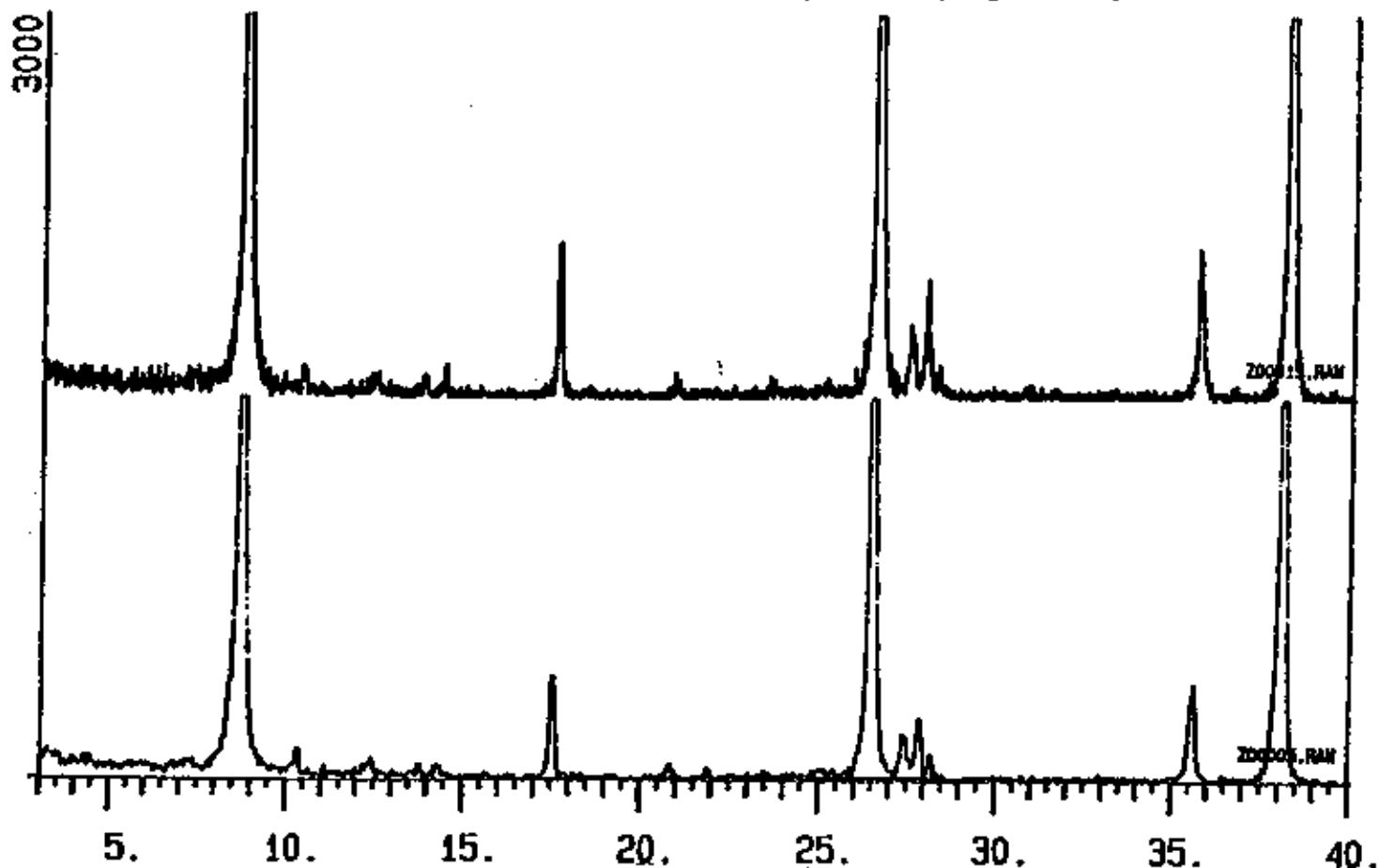


Figure 13: CG:1 quench solution X-ray diffractograms used to determine the effect of ethylene glycolation treatment; unglycolated secondary mineral fraction diffractogram (top), and ethylene glycol treated secondary mineral fraction diffractogram (bottom).

This analysis was conducted using $\text{CuK}\alpha_1$ radiation ($K\alpha_1 = 1.5406\text{\AA}$, $K\alpha_2 = 1.5443\text{\AA}$)

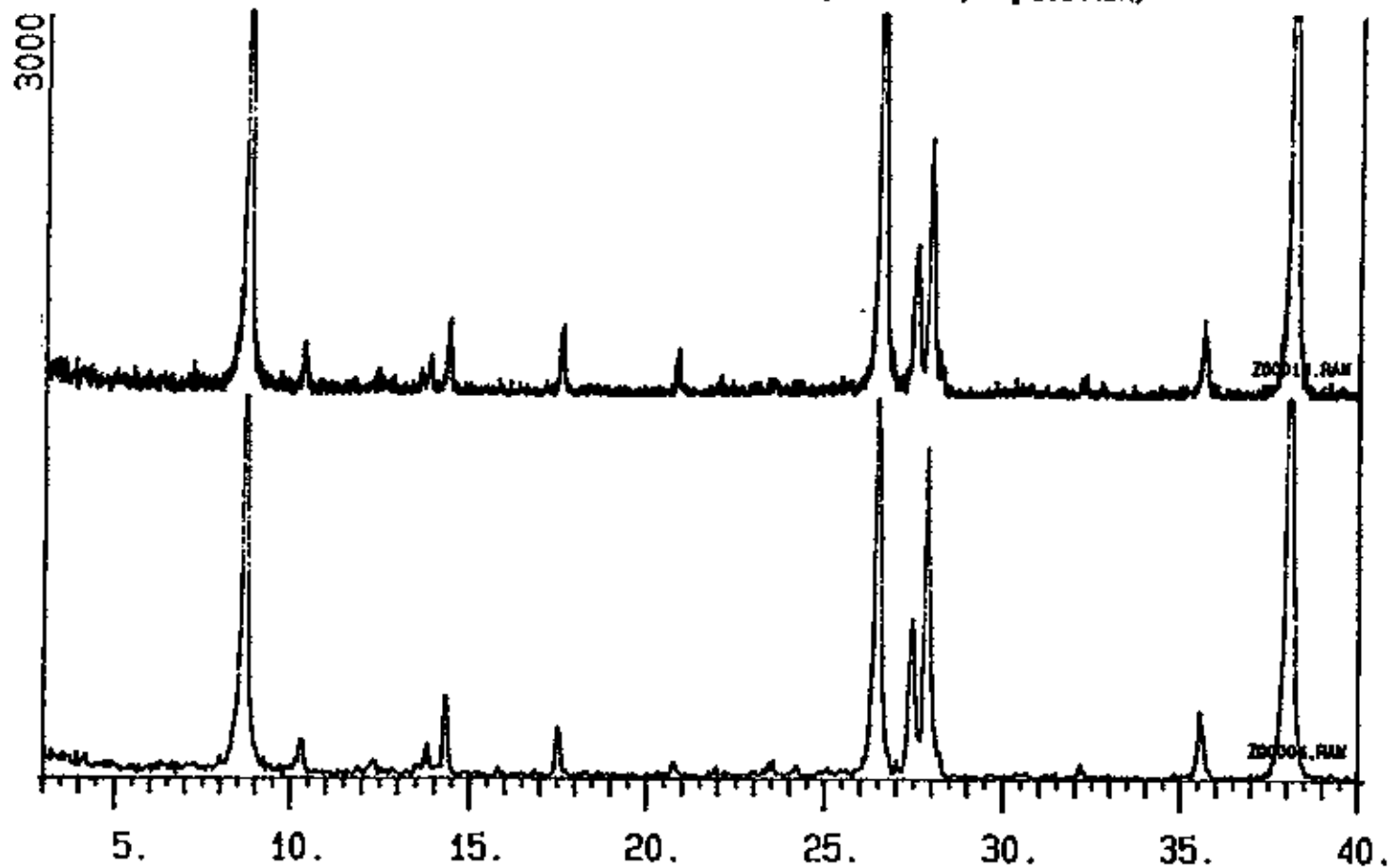


Figure 34: X-ray diffractogram of secondary and primary minerals removed from the CO₂ quench aliquot.

TABLE 3: SECONDARY MINERALS IDENTIFIED IN THE TUFF (BRT:1), AND GRANITE EXPERIMENTS (CG:1, CG:2), USING, XRD, SEM/EDS, AND SUPPORTING LOG IAP/K DATA AT 300° C AND 30 MPa

ALIQUOT	SEM/EDS	XRD	SEE FIGURE
BRT 1.2	I,A*,S	S,I?	8,9,13
BRT 1.3	-----	S?	14
BRT 1.4	-----	I*,S*	15
BRT 1.5	-----	I*,S?	16
BRT 1.6	-----	I,S	17
BRT 1.7	I,AN*,S	I,S	10,11,18
BRT 1.8	-----	I*	19
BRT 1.9	S	I,S	12,20
BRT 1.10	-----	I*	21
CG 1.K	I	I,Q*,HA,H*	26,31,33
CG 2.E	I,Q*,HA	I,Q*,HA	27,28,29 32,34

I=ILLITE, S=SMECTITE (BEIDELLITE), HA=HIGH ALBITE
 A=AMORPHOUS SILICA, AN=ANHYDRITE, Q=QUARTZ
 *=IDENTIFICATION SUPPORTED BY LOG IAP/K DATA
 ?=VERY FAINT XRD PEAK(S)

NOTES:

- 1) TOPOLOGIC MINERAL STABILITY DIAGRAMS INDICATE THAT THE SMECTITES FORMED IN EXPERIMENT CG:1, CG:2, AND BRT:1 ARE BEIDELLITES.
- 2) ILLITE PEAKS BEST MATCH THOSE OF DIOCTAHEDRAL ILLITE (2M1) (JCPDS CARD NO. 26-911).
- 3) QUENCH SOLUTION Ca CONCENTRATION (TABLE 5) AND LOG IAP/K DATA SUGGEST THAT SMALL AMOUNTS OF CALCITE FORMED DURING EXPERIMENT CG:2.
- 4) CLAY (ILLITE AND SMECTITE) AND HIGH ALBITE THERMOCHEMICAL DATA ARE NOT CONSIDERED RELIABLE.

DISCUSSION OF SECONDARY MINERAL DATA: PHASE
DIAGRAM DATA AND THE EFFECT OF SECONDARY
MINERAL PRECIPITATION ON SOLUTION
PARAMETERS

Experiment BRT:1 and CG:2 aliquot data were plotted on log Na/H vs. log K/H diagrams (Figures 33-36). High albite, muscovite, and microcline phase boundaries were constructed using thermodynamic data calculated of Helgeson *et al.* (1981). Smectite and illite phase boundaries were not plotted due to lack of 300°C clay thermochemical data. Experiment CG:2 and BRT:1; Na/H and K/H ratios were calculated using the computer program HIPHPR2 (Kacandes and Grandstaff, 1989; Grandstaff *et al.*, 1990). In Figure 35 italic numbers are used to represent the sequence of tuff experiment aliquots (*i.e.* an italic 1 refers to aliquot BRT:1). Amorphous silica saturation is used to define SiO₂ activities in Figure 35. Plain numbers are used to represent the sequence of granite experiment aliquots in Figure 36. Quartz saturation is used to define SiO₂ activity in Figure 36. Experiment BRT:1 and CG:2 cation/proton ratios are listed in Appendices 1a and 1b, respectively.

FIGURES 35-36 DATA PRESENTATION: The data point distribution in Figure 35 shows that the tuff solution is saturated with respect to microcline. The tuff experiment data point scatter is near-linear. Figure 36 indicates that the granite solution is saturated with respect to microcline during the beginning of the experiment (CG 2.1-2.4), and with muscovite towards the end (CG 2.5-2.8). The granite data point scatter is also near-linear.

FIGURES 35-36 DATA INTERPRETATION: In hydrothermal systems the formation of secondary minerals controls solution parameters (*i.e.* SiO_2 , K, Na, Mg, Fe, Ca, pH, etc.). A near-linear data point distribution would indicate the presence of a secondary mineral phase boundary.

Secondary microcline was not identified from tuff experiment aliquots. The major source of Na in the tuff is rhyolitic glass. The EDS spectra of smectites removed from experiment BRT:1 solution aliquots suggest that Na was incorporated into smectite structures. The major source of K in the tuff is rhyolitic glass. Illite is the only identified K-bearing secondary mineral. Tuff aliquot X-ray diffractograms suggest that illite

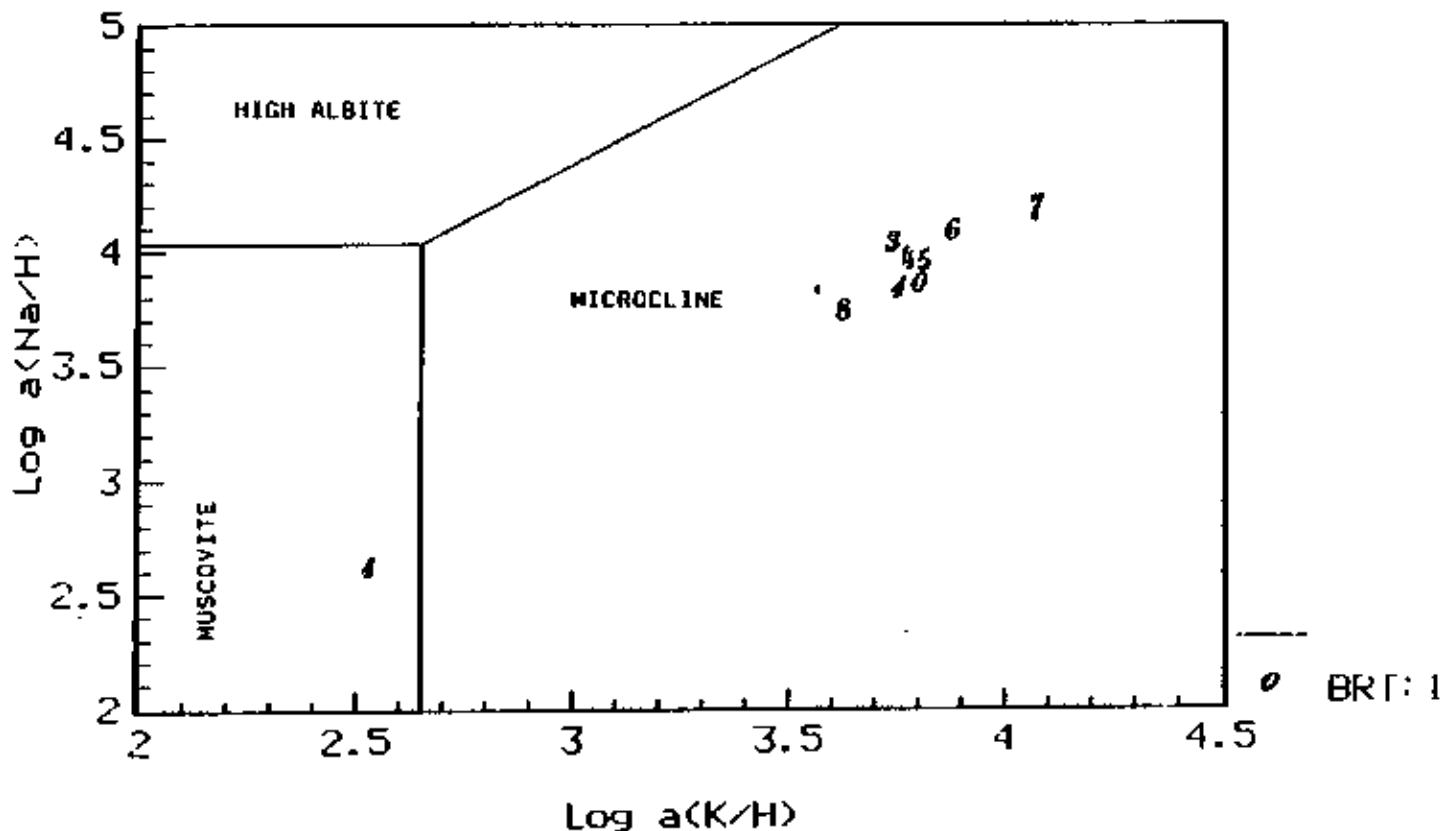


Figure 35: A log Na/M vs. log K/M plot used to show a near-linear trend indicating a probable dioctahedral illite:beidellite phase boundary (BRT:1 aliquot data points).

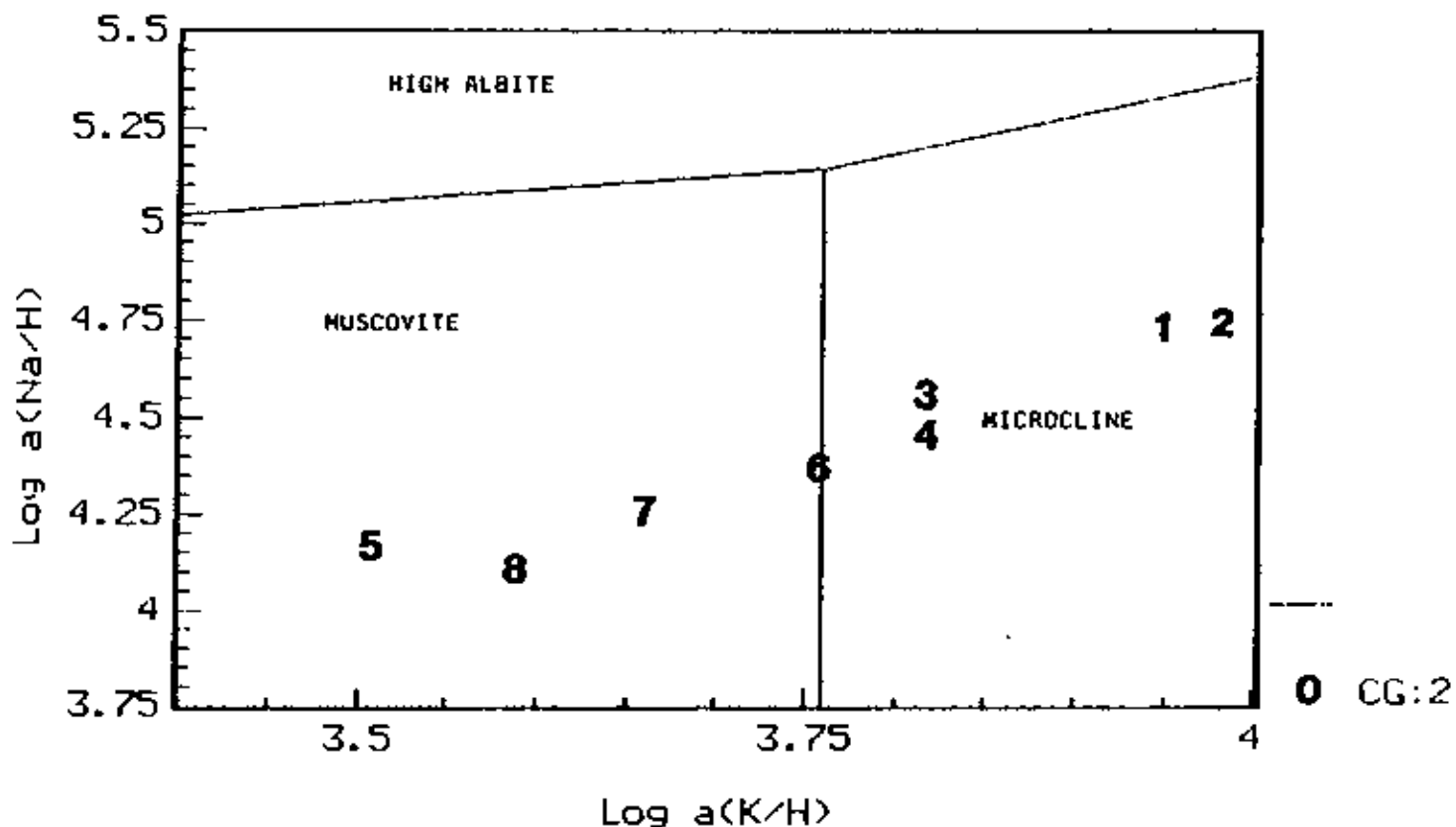


Figure 36: A log Na/H vs. log K/H plot used to show a near-linear trend indicating a possible high albite:di-octahedral illite phase boundary (CG:2 aliquot data points).

started to remove K from solution by the 3.25 hours sample. These results suggest that the near-linear clustering of experimental points in this phase diagram fall along a illite:smectite equilibrium boundary. Secondary microcline and muscovite were not identified in EDS/SEM and XRD analyses of CG:1 and CG:2 quench secondary minerals. Dissolution of primary microcline supplied the granite solution with K. The precipitation of secondary illite removed K from the granite experiment solutions. In the granite experiments Na was primarily released by dissolution of primary albite (see Solution Parameters vs. Time section). The main Na-bearing secondary mineral formed was high albite. The overall linear trend of these data therefore should approximate the illite-high albite phase boundary at 300°C and 30 MPa.

The near-linear distribution of granite (CG 2.1-2.6) and tuff (BRT 1.2-1.10) experiment data points in these diagrams suggests that the equilibrium between secondary minerals control solution parameters in these experiments.

LOG IAP/K SUPPORTING DATA

Figures 37-42 contain log IAP/K vs. time diagrams of secondary minerals with stable log IAP/K values (values are from Tables 4-5) between -1 and 1, and which have been identified using SEM/EDS and/or XRD. The time scale refers to hours elapsed since the start of the experiment. This scale is in hours raised to the 0.40 power and is used to analyze short-term trends in the initial samples of our experiments. Dotted lines are used to demarcate the area (i.e., $-1 \leq \log \text{IAP/K} \leq 1$) which is used to represent saturation with respect to the secondary minerals considered in these diagrams. The solid line in the center of each log IAP/K diagram represents a log IAP/K of exactly 0. The dashed lines represent the log IAP/K trends vs. time.

The granite experiment log IAP/K trend diagrams support the SEM/EDS and/or XRD identification analyses for quartz (Figure 37) and hematite (Figure 38).

The tuff experiment log IAP/K trend diagrams suggest the presence of amorphous silica (Figure 39), anhydrite (Figure 40), illite (Figure 41) and beidellites (Figure 42). Calcite was not

TABLE 4: CO:2 LOG IAP/K Activity ratios for selected minerals

RUN	1	2	3	4	5	6	7	8
ANHYDRITE	-1.08	-0.96	-0.53	-0.24	-0.45	-0.33	-0.31	-0.47
CALCITE	1.37	1.54	1.31	1.22	0.42	1.02	1.22	0.35
CHALCEDONY	-0.33	-0.19	-0.09	-0.10	-0.11	-0.13	-0.09	-0.17
SEPIOLITE	1.32	2.20	2.73	0.98	-0.55	0.08	-0.37	-3.64
DOLOMITE	3.46	3.63	3.44	2.83	1.61	2.47	2.59	0.86
A. SILICA	-0.62	-0.48	-0.38	-0.39	-0.39	-0.41	-0.38	-0.46
QUARTZ	-0.19	-0.05	0.05	0.04	0.03	0.01	0.05	0.03
FLUORITE	-2.10	-1.60	-1.19	-1.30	-1.38	-0.97	-0.81	-1.14
ILLITE	-2.31	-2.17	-1.91	-2.17	-1.96	-2.32	-2.06	-2.20
PREHNITE	0.94	1.39	1.14	1.01	-0.09	0.50	1.03	-0.35
WAIKAKITE	-0.91	-0.49	-0.36	-0.51	-0.86	-0.82	-0.36	-1.11
7A CLIN.	6.98	7.10	7.34	5.11	3.63	4.08	3.57	0.14
HEMATITE	----	----	----	----	0.13	-0.08	0.56	-0.07
MAGNETITE	----	----	----	----	0.17	0.08	0.39	0.07
GOETHITE	----	----	----	----	0.17	0.08	0.39	0.07
14 A CLIN.	9.38	9.50	9.73	7.50	6.03	6.48	5.96	2.54

Clin.= Clinoclone

Table 5: BRT;1 log IAP/K activity ratios for selected minerals

RUN	1	2	3	4	5	6	7	8	10
ADULARIA	1.08	0.30	0.58	0.64	0.54	0.16	-0.14	0.84	0.55
ANHYDRITE	-0.28	-0.32	-0.07	-0.13	0.28	-0.15	-0.31	0.07	-0.03
CHALCEDONY	0.21	0.32	0.29	0.34	0.30	0.27	0.28	0.31	0.27
AM. SILICA	-0.07	0.03	0.01	0.05	0.02	-0.01	0.00	0.03	-0.02
QUARTZ	0.35	0.46	0.43	0.48	0.45	0.41	0.43	0.46	0.41
CA-BEIDEL.	4.22	3.53	0.36	0.27	0.13	-0.87	-1.92	1.15	0.22
MG-BEIDEL.	3.91	1.24	-1.85	-0.05	-0.22	-3.05	-2.25	0.83	-0.09
NA-BEIDEL.	3.43	2.68	-0.35	-0.44	-0.65	-1.56	-2.56	0.47	-0.43
MICROCLINE	1.09	0.31	0.59	0.65	0.55	0.17	-0.13	-0.85	0.56
MUSCOVITE	3.90	2.34	-0.49	-0.64	-0.82	-1.92	-3.16	-0.47	-0.50
K-BEIDELL.	2.00	1.24	-1.85	-1.92	-2.12	-3.05	-4.06	-4.00	-1.91
7A CLIN.	-4.31	-11.53	2.17	2.84	4.06	3.73	1.67	0.80	1.41
FLUORITE	-4.64	-5.06	-1.00	-1.01	-0.56	-0.69	-0.51	-1.80	-1.48
SEPIOLITE	-5.06	-13.62	-0.27	0.61	1.53	1.73	0.87	-1.84	-0.94
HAIRAKITE	1.69	0.38	0.45	0.35	0.61	-0.54	-1.44	0.58	-0.06
ILLITE	2.37	1.07	-0.60	-0.63	-0.75	-1.62	-2.63	0.08	-0.68
HEMATITE	----	----	----	1.28	0.92	2.03	2.44	----	1.95
MAGNETITE	----	----	----	1.70	0.77	2.44	3.05	----	2.32
GOETHITE	----	----	----	0.74	0.56	1.12	1.32	----	1.08
CALCITE	-1.95	2.48	0.29	0.23	0.76	0.49	0.48	-0.35	-0.12

Clin. = Clinocllore

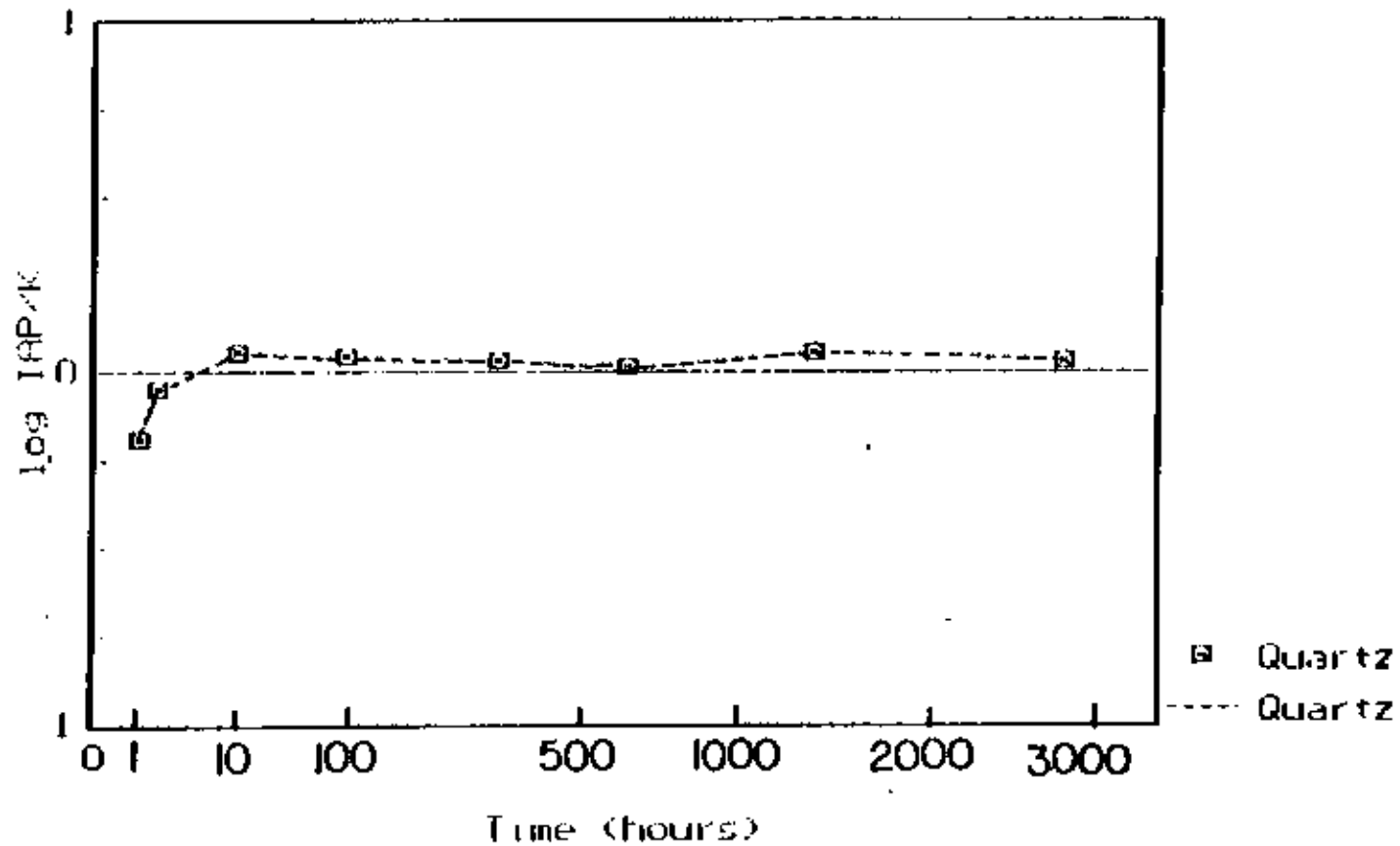


Figure 37: Granite experiment (CG:2) quartz saturation indices (log IAP/K) as calculated by the computer program NIPHR2

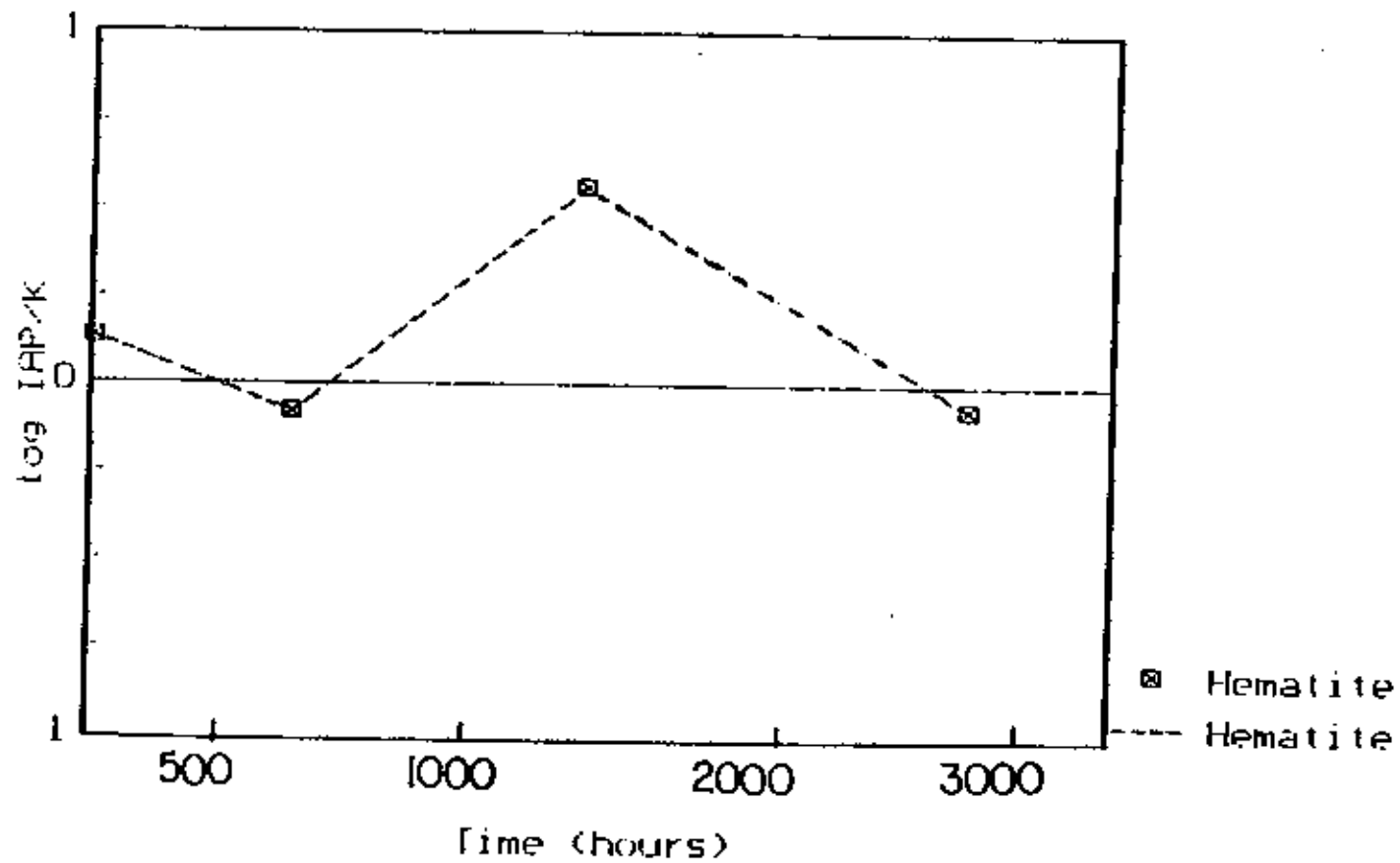


Figure 38: Granite experiment (CO₂) hematite saturation indices (log IAP/K) as calculated by the computer program NIPHR2.

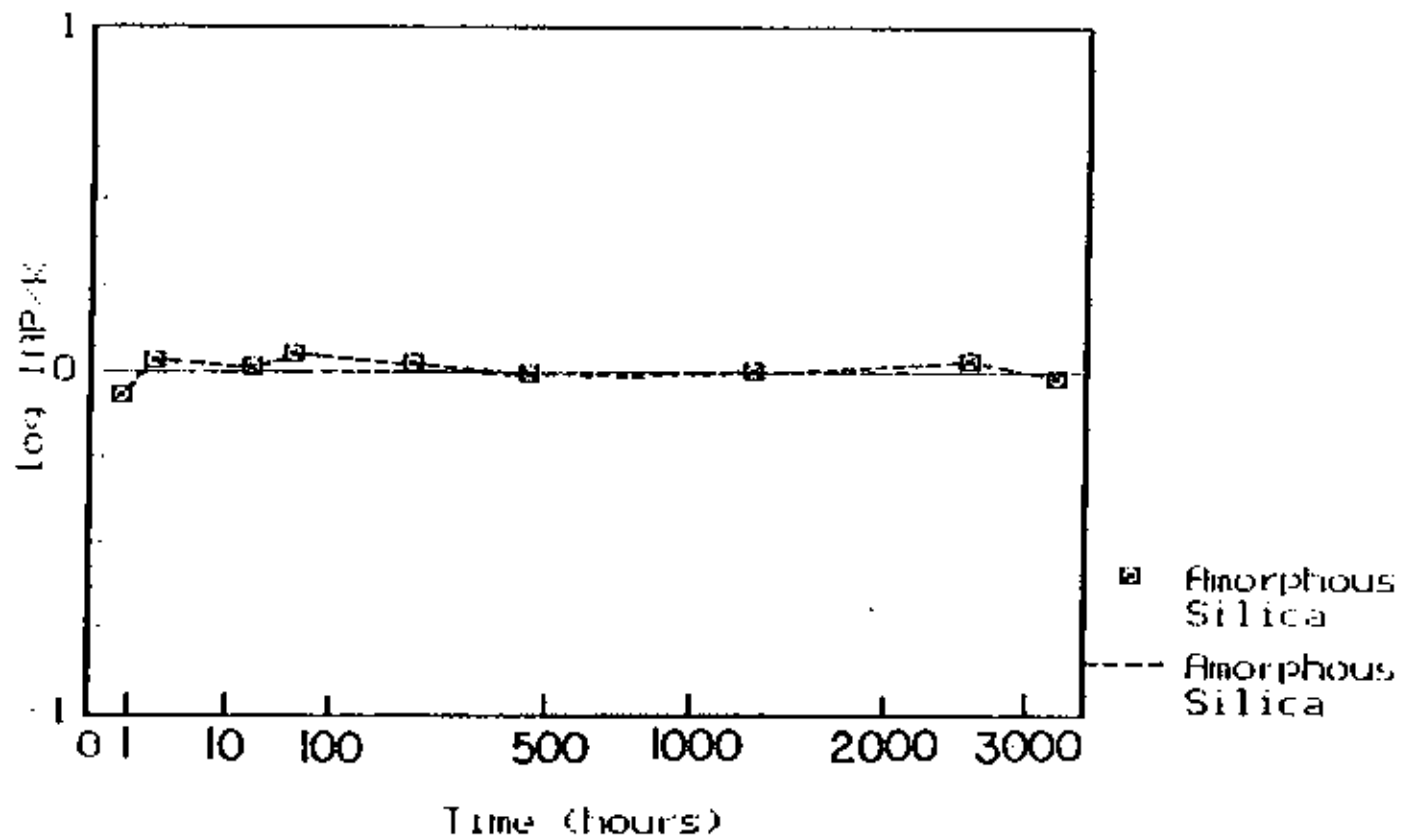


Figure 39: Tuff experiment (BRT:1) amorphous silica saturation indices (log IAP/K) as calculated by the computer program HIPNPR2

TUFF (BRT 1) LOG IAP/K FOR
ANHYDRITE
300 DEGREES (C), 30 MPa

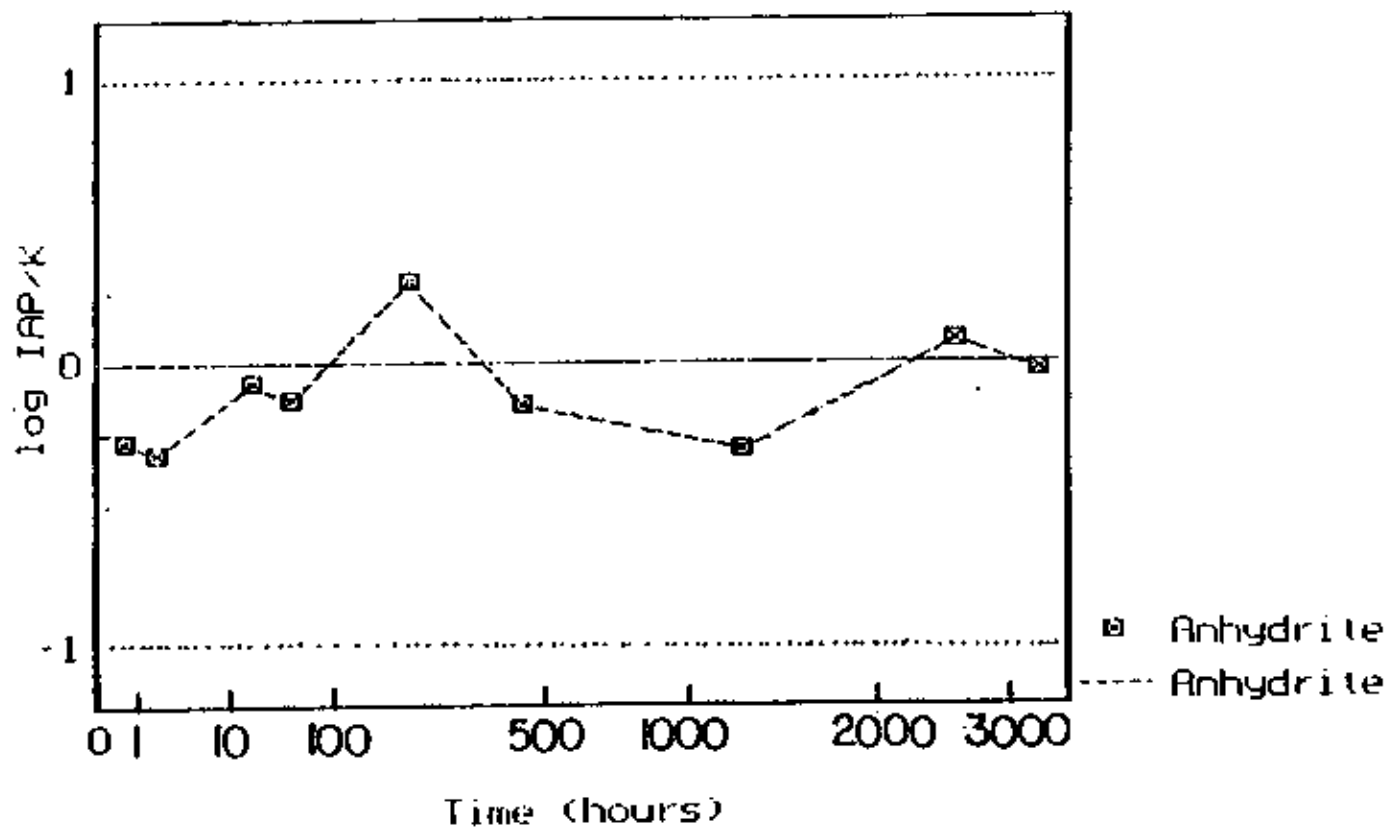


Figure 40: Tuff experiment (BRT:1) anhydrite saturation indices (log IAP/K) as calculated by the computer program HIPHR2

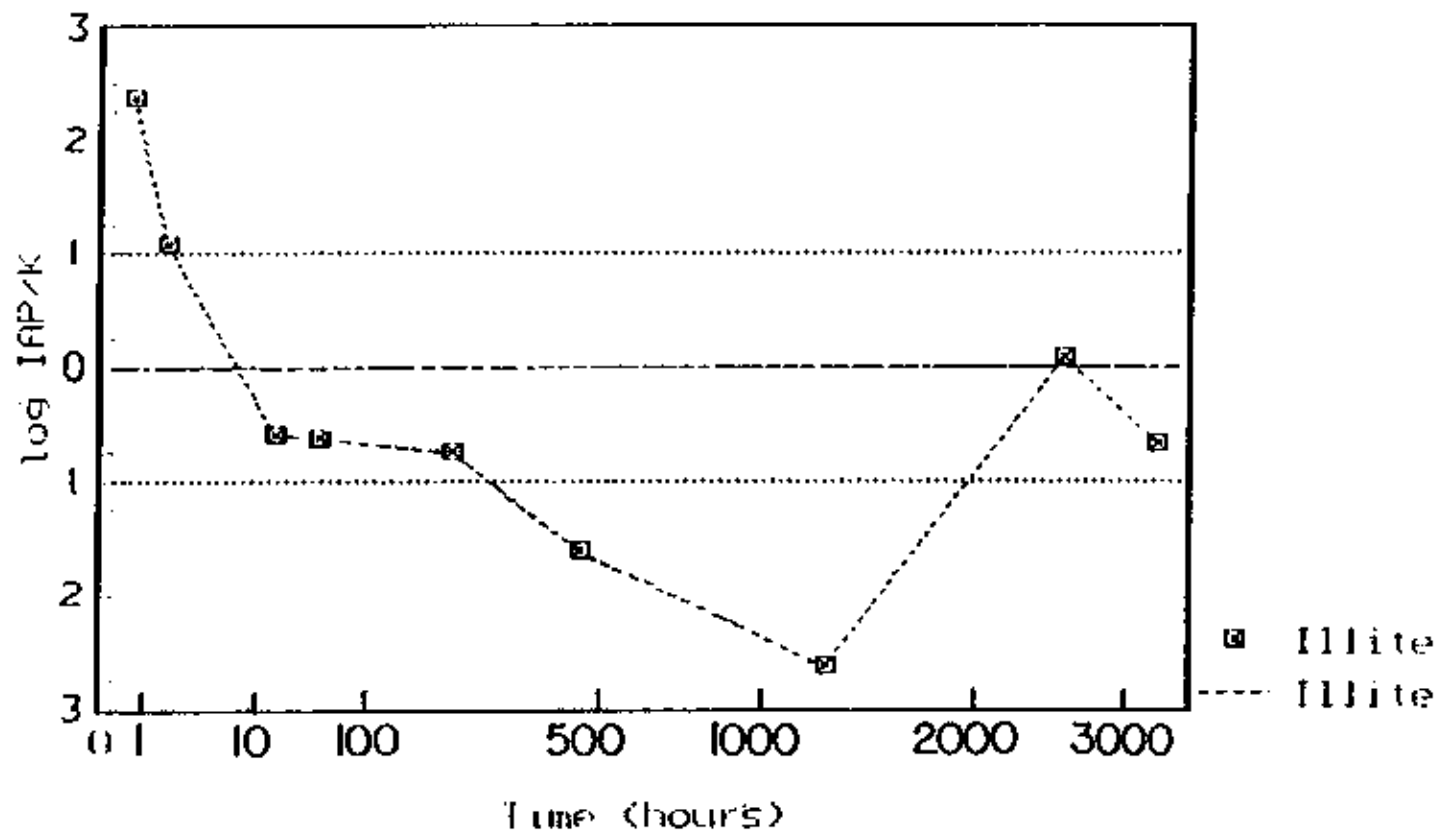


Figure 41: Tuff experiment (BRT:1) illite saturation indices (log IAP/K) as calculated by the computer program HIPHR2

TUFF (BRT 1) LOG IAP/K FOR
 Ca, Na, AND Mg BEIDELLITE
 300 DEGREES (C), 30 MPa

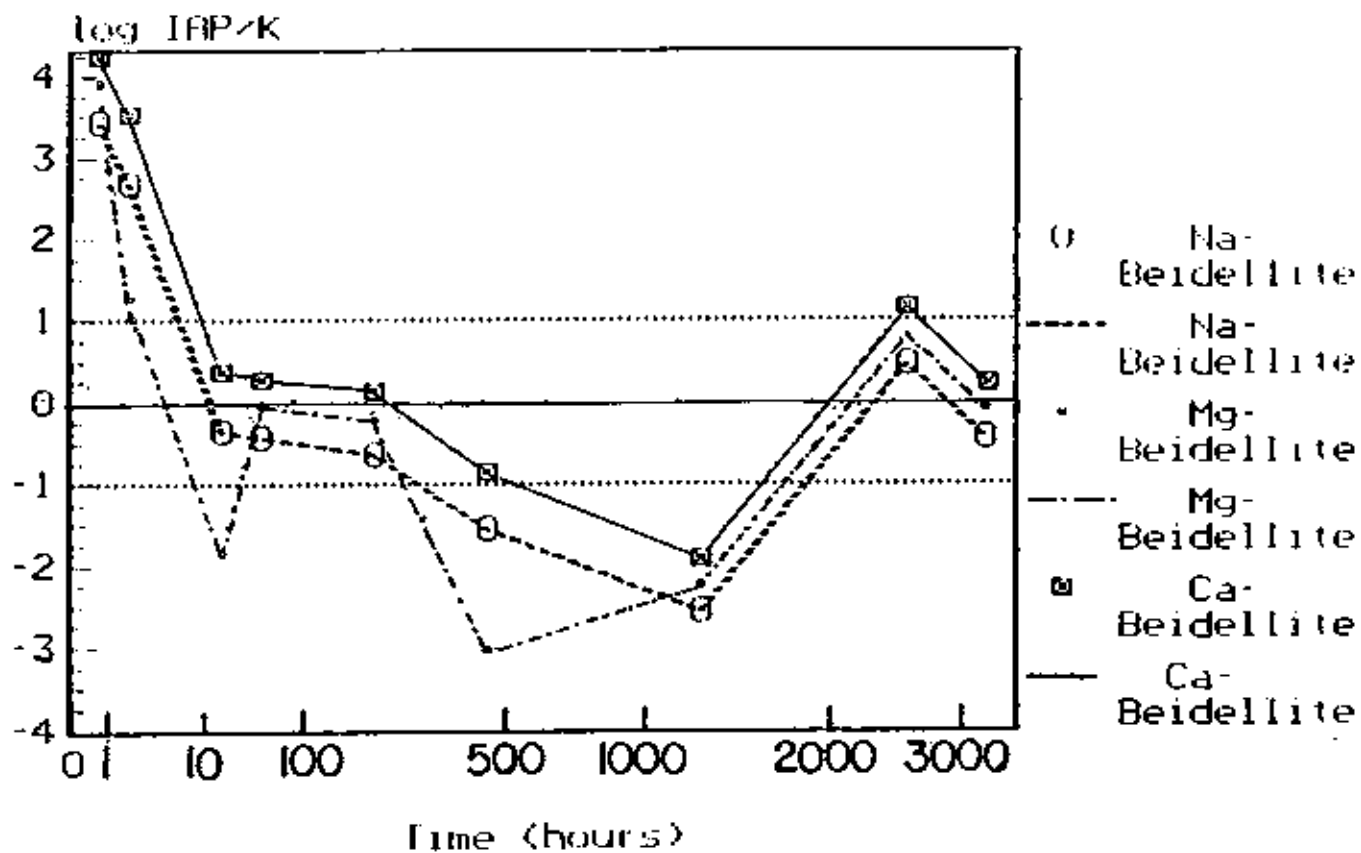


Figure 42: Tuff experiment (BRT:1) Ca, Na, Mg, Beidellite saturation indices (log IAP/K) as calculated by the computer program HIPMPR2

identified from CG:2 quench solution secondary minerals using XRD/EDS techniques. However Ca quench solution concentrations (see Solution Parameters vs. Time section) and log IAP/K data (Table 4) suggest that secondary calcite may have formed. It is possible that secondary calcite became unstable during the cooling of quench solution CG:2 releasing Ca into solution.

It should be mentioned that the clay mineral and high albite thermochemical data are not considered to be reliable.

A COMPARISON OF THE CLAY MINERALS FORMED IN
THE GRANITE (CG:2), TUFF (BET:1), AND TEMPLE
300°C BASALT EXPERIMENTS AND POSSIBLE EFFECTS
ON RADIONUCLIDE MOBILITY

DATA PRESENTATION: Profuse amounts of 15Å smectite (i.e. saponite), which expand to 17Å upon glycolation are the dominant secondary mineral formed during most 300°C basalt:water experiments (Gardiner, 1988). Illite has also been identified in small quantities from 300°C basalt:water experiments. It is significant that the major secondary mineral formed in these 300°C high-SiO₂

rock experiments is 10A non-expanding illite (beidallitic smectites were also identified in lesser amounts). These comparisons indicate that the illite/smectite mass ratio of the granite and tuff experiment are higher, when compared to the basalt:water experiments.

A visual examination of the secondary minerals removed from CG:1, CG:2, and Temple basalt:water experiment quench solutions was undertaken. These comparisons clearly indicate that the total mass of secondary minerals recovered from basalt experiment quench solutions, is much higher than those removed from the granite experiments (CG:1 and CG:2). These comparisons suggest that lesser amounts of secondary minerals (total mass) formed in the granite experiments (compared to the basalt experiments).

The quench solution from experiment BRT:1 has not been removed, due to the use of this autoclave run for a reinjection experiment (see Introduction section). A redox buffering capacity calculation based on the amount of FeO contained within the tuff, suggests that approximately 16% of the tuff glass dissolved during experiment BRT:1 (see Redox Comparisons section). The total weight of Conway Granite sample powder added to experiment CG:2 was

16.20 grams. After the removal of the CG:2 quench solution primary and secondary minerals were removed from the CG:2 quench solution and separated (see Experimental Techniques section). The total weight of CG:2 quench primary minerals was measured as 15.64 grams. These inventory calculations indicate that approximately 2% of the total Conway Granite sample mass dissolved during experiment CG:2 (in comparison to approximately 16% of the rhyolitic glass in BRT:1). These calculations indicate that lesser amounts (total mass) of secondary minerals formed in the granite experiment (compared to tuff).

DATA INTERPRETATION: If these data are useful in determining the effect of rock type and crystallinity on illite/smectite mass ratio and secondary mineral precipitation rates in lower temperature repository solutions, then the following conclusions can be made:

- 1) Illite would be the predominant secondary mineral to precipitate out of high-SiO₂ rock (i.e. granite and tuff) repository solutions.

2) Secondary smectite would be the dominant mineral to precipitate from basalt repository solutions.

3) Lesser amounts of secondary minerals would form in granite repository solutions.

Smectites have superior sealing and sorption capabilities (when compared to illites). The formation of larger amounts of sorptive smectite in basalt repository solutions should result in comparatively lower radionuclide mobility (for some radionuclides) and lower porosity, near waste containers (when compared to granite and basalt). The formation of lesser amounts of secondary minerals in granite repository solutions would result in comparatively higher porosity near waste container packages (compared to basalt and granite). Higher porosity near granite repository waste containers, would result in comparatively higher radionuclide mobility (compared to basalt and tuff sites). The results of these secondary mineral analyses suggest that radionuclide mobility may be comparatively lower in a basalt enclosed high-level nuclear waste repository (compared to granite and tuff).

SOLUTION PARAMETER TRENDS VS. TIME.

Results of aliquot and quench solution analyses from the granite (CG:1, CG:2), and tuff (ERT:1) experiments are listed Tables 6, 7, and 8. These results were used to construct log concentration (mg/l) vs. time (exponential hours) diagrams (Figures 43-46, 48-50, and 52-54). The scale used in these diagrams is identical to the scale selected by previous Temple basalt autoclave researchers (Kacandes, 1988; Gardiner, 1987; Korn, 1986; McKeon, 1984; and Moore, 1983) for convenience of comparison. The logarithmic concentration scale was selected so that a large range of concentration measurements could be included on the same diagram. The exponential time scale refers to the amount of hours elapsed since the start of the experiment. This scale is in hours raised to the 0.40 power, and is useful to allow us to analyze trends representing initial intervals of the tuff and granite experiments.

Major species concentration vs. time curves for the three autoclave experiments are shown in Figures 43-45. These curves were plotted to compare the concentration trends of major species

TABLE 6: CG:2 SOLUTION PARAMETER VALUES FOR 125-250 MICRON CONWAY GRANITE AND $3.4 \times 10^{-3} \text{M}$ NaCl SOLUTION IN DICKSON ROCKING AUTOCLAVE EXPERIMENTS AT 300°C AND 300 MPa

SAMPLE HOURS	0	1	2	3	4	5	6	7	8	9
	0	1.36	3.17	24	96	313	623	1324	2761	2765
pH(m)	5.64	6.44	6.60	6.35	6.34	6.10	6.21	6.13	6.09	6.11
pH(c)	5.59	7.18	7.24	7.02	6.96	6.67	6.89	6.85	6.70	----
HCO ₃	0.2	62.6	64.2	67.3	53.0	45.2	54.8	66.6	45.0	52.1
H ₂ S(T)	N/D	N/D	N/D	N/D	DET	0.08	1.46	1.32	1.50	1.51
Cl	132.0	114.1	120.2	138.6	126.5	124.9	122.3	120.2	133.1	194.1
SO ₄	0.50	0.51	0.51	1.02	1.52	1.52	1.53	1.02	2.02	5.85
F	0.00	1.02	1.64	2.55	2.03	3.36	3.60	3.68	5.52	6.10
SiO ₂	2.1	434	604	753	728	719	691	748	617	655
Ca	0.04	0.69	0.84	1.08	1.30	0.73	1.04	1.62	0.57	7.98
Na	82.2	93.1	84.3	87.4	86.8	100.4	79.5	76.2	88.3	85.6
K	2.5	27.0	25.6	29.5	34.5	35.2	36.6	32.4	45.1	27.5
Mg	0.00	0.07	0.06	0.11	0.05	0.05	0.04	0.03	0.01	0.02
Al	0.00	4.16	3.05	1.94	1.48	1.56	1.47	1.72	2.17	0.60
Fe	0.00	0.18	0.16	0.10	0.14	0.16	0.08	0.18	0.12	0.54
Mn	0.00	----	----	0.04	0.06	----	0.04	----	0.03	0.15
Li	0.00	0.16	----	0.27	0.37	0.51	0.36	0.61	----	0.51
DHEM	----	----	----	----	----	-26.4	-29.0	-29.3	-30.0	----
Log fO ₂	----	----	----	----	----	-29.9	-31.5	-31.6	-31.2	----

pH(m)= Measured pH pH(c)= Calculated pH N/D= Not Detected DET= Detected (>0.08 mg/l)
 DHEM= Dissolved H₂ Evolution Method T=Total

TABLE 7: BRT:1 SOLUTION PARAMETER VALUES FOR 125-250 MICRON BANNOCK RHYOLITE TUFF AND $3.4 \times 10^{-3}M$ NaCl SOLUTION IN DICKSON ROCKING AUTOCLAVE EXPERIMENTS AT 300°C AND 300 MPa

SAMPLE HOURS	0	1	2	3	4	5	6	7	8	9	10
	0	0.5	3.3	36	63	204	449	1264	2559	2582	3531
pH(m)	5.74	5.96	5.52	5.52	5.48	5.45	5.25	5.28	5.40	----	5.46
pH(c)	5.74	5.29	4.57	6.51	6.53	6.56	6.64	6.76	6.28	----	6.49
HCO ₃	0.2	73.9	63.0	61.8	64.0	73.9	76.0	77.5	64.4	64.1	64.0
H ₂ S(T)	N/D	N/D	N/D	N/D	N/D	N/D	N/D	N/D	N/D	N/D	N/D
Cl	138.5	134.1	136.2	134.1	139.7	154.6	131.3	130.0	154.4	----	145.9
SO ₄	1.00	4.09	4.09	4.34	5.10	5.09	5.12	6.39	10.19	----	12.69
F	0.00	3.32	8.08	19.80	21.54	19.73	22.02	26.07	15.34	----	16.47
SiO ₂	2.1	1493	1900	1796	1997	1854	1723	1771	1894	----	1699
Ca	0.12	0.87	2.60	0.92	0.69	1.91	0.72	0.45	0.49	----	0.39
Na	76.2	52.6	60.2	83.3	68.2	66.8	77.4	81.9	75.2	----	74.9
K	0.25	81.5	85.5	83.4	83.7	85.8	85.7	88.1	92.0	----	94.7
Mg	0.01	0.03	0.03	0.03	0.04	0.07	0.07	0.03	0.03	----	0.03
Al	0.00	7.42	6.75	6.10	6.37	5.65	5.49	5.47	5.44	----	5.01
Fe	0.12	0.45	0.82	0.37	0.82	0.51	1.58	1.91	2.41	----	1.95
Mn	0.02	----	----	0.02	----	----	----	----	0.02	----	0.02
Li	0.00	----	----	----	----	----	----	----	0.06	----	0.18
DHEM	----	----	----	----	-28.92	-27.34	-27.32	-27.32	----	----	-27.32
log fO ₂	----	----	----	----	----	----	----	----	----	----	----

pH(m)= Measured pH pH(c)= Calculated pH N/D= Not Detected DET= Detected (<0.08 mg/l)
DHEM= Dissolved H₂ Evolution Method T=Total

TABLE 8: CG-1 SOLUTION PARAMETER VALUES FOR 125-250 MICRON CONWAY GRANITE AND $3.4 \times 10^{-3}M$ NaCl SOLUTION IN DICKSON ROCKING AUTOCLAVE EXPERIMENTS AT 300°C AND 300 MPa

SAMPLE HOURS	0	1	2	3	4
	0.0	1.4	3.0	21.4	108.3
pH(m)	5.64	6.31	6.43	6.14	6.20
pH(c)	5.56	6.53	6.54	6.55	6.54
HCO ₃	0.00	22.6	22.6	33.4	29.7
H ₂ S(T)	N/D	N/D	N/D	N/D	N/D
Cl	145.0	180.7	168.6	171.6	175.7
SO ₄	0.50	8.2	4.1	5.6	7.1
F	0.00	0.86	2.43	0.87	3.11
SiO ₂	0.50	400	562	718	734
Ca	0.04	0.57	0.79	1.06	1.00
Na	72.1	94.4	95.3	97.5	86.7
K	0.04	44.0	23.8	26.3	62.5
Mg	0.00	0.02	0.03	0.05	0.05
Al	0.00	3.16	2.94	1.69	1.57
Fe	0.04	0.02	0.08	0.08	0.08
Mn	----	----	----	----	----
Li	----	----	----	----	----
DHEM	----	----	----	----	----
Log fO ₂	----	----	----	----	----

pH(m)= Measured pH pH(c)= Calculated pH N/D= Not Detected DET= Detected (<0.08 mg/l)
DHEM= Dissolved H₂ Evolution Method Y=Total

(stable concentration values greater than 2 ppm in all 3 experiments) present in the three experiments.

Each of the trend comparison diagrams (Figures 46, 48-50, 52-54) contain both granite (CG:2) and tuff (BRT:1) concentrations for two species in solution. These diagrams were constructed to make detailed uncluttered comparisons of major and minor solution parameter trends in the tuff and granite experiments. In the comparison diagrams, dotted lines represent the tuff experiment and solid lines represent the granite experiment. Values of $\log IAP/K$ (from Tables 4-5), calculated using the computer program NIPHPR2 (Kacandes and Grandstaff, 1989; Grandstaff *et al.*, 1990) will be utilized to determine which secondary minerals controlled solution parameters.

MAJOR SPECIES

FIGURES 43 AND 44: EXPERIMENTS CG:1 AND CG:2

MAJOR SPECIES DATA COMPARISON

FIGURES 43 AND 44 DATA PRESENTATION: Autoclave experiment CG:1 and CG:2, zero to one hundred hour interval major species concentration trends are

TABLE 8: CG:1 SOLUTION PARAMETER VALUES FOR 125-250 MICRON CONWAY GRANITE AND $3.4 \times 10^{-3}M$ NaCl SOLUTION IN DICKSON ROCKING AUTOCLAVE EXPERIMENTS AT 300°C AND 300 MPa

SAMPLE HOURS	0	1	2	3	4
	0.0	1.4	3.0	21.4	108.3
pH(m)	5.64	6.31	6.43	6.14	6.20
pH(c)	5.56	6.53	6.54	6.55	6.54
HCO ₃	0.00	22.6	22.6	33.4	29.7
H ₂ S(T)	N/D	N/D	N/D	N/D	N/D
Cl	145.0	180.7	168.6	171.8	175.7
SO ₄	0.50	8.2	4.1	5.6	7.1
F	0.00	0.86	2.43	0.87	3.11
SiO ₂	0.50	400	562	718	734
Ca	0.04	0.57	0.79	1.06	1.00
Na	72.1	94.4	95.3	97.5	86.7
K	0.04	44.0	23.8	26.3	62.5
Mg	0.00	0.02	0.03	0.05	0.05
Al	0.00	3.16	2.94	1.69	1.57
Fe	0.04	0.02	0.08	0.08	0.08
Mn	----	----	----	----	----
Li	----	----	----	----	----
DHEM	----	----	----	----	----
Log fO ₂	----	----	----	----	----

pH(m)= Measured pH pH(c)= Calculated pH N/D= Not Detected DET= Detected (<0.08 mg/l)
DHEM=Dissoved H₂ Evolution Method T=Total

similar (Figures 43-44). The concentration of Cl in the CG:1 solution is slightly higher.

FIGURES 43 AND 44 DATA COMPARISON: This comparison suggests that the data gathered from the Granite experiments are reproducible. The higher Cl concentrations present in experiment CG:1 are probably due to the slightly higher concentration of Cl in the CG:1 starting solution.

FIGURES 44 AND 45: EXPERIMENTS CG:2 AND BRT:1

MAJOR SPECIES DATA PRESENTATION: The concentration of SiO_2 , K, Al, HCO_3 , and F in solution increased sharply during the 0 to 1 hour interval of the Granite (Figure 44) and Tuff experiment (Figure 45). Figures 44 and 45 were used to calculate the minimum rate of major species release during the first hour of the completed Granite and Tuff experiments. The actual rate of species release is higher due to the incorporation of some of these species into secondary mineral structures. The BRT:1 experiment, SiO_2 , K, F, and Al slopes from zero to one hours are approximately 1060, 80, 5, and 7 ppm/hour, respectively. The CG:2 experiment SiO_2 , K, F, and Al slopes from zero to one hours are approximately 300, 28, 1, and 3 ppm/hour,

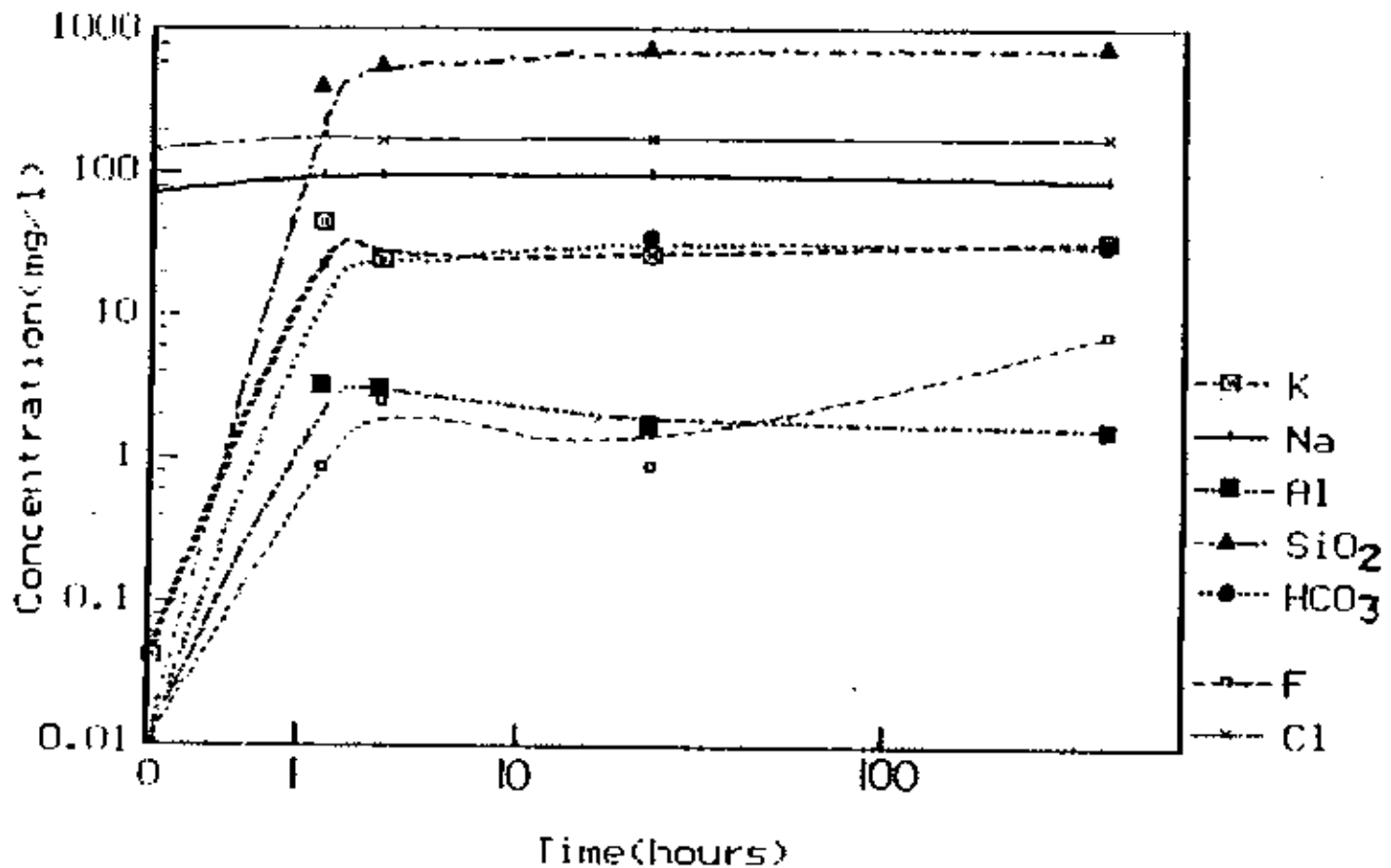


Figure 43: Concentration-time trends for major dissolved species in solution from the first terminated Conway Granite experiment (CG:1) conducted at 300°C and 300 bars.

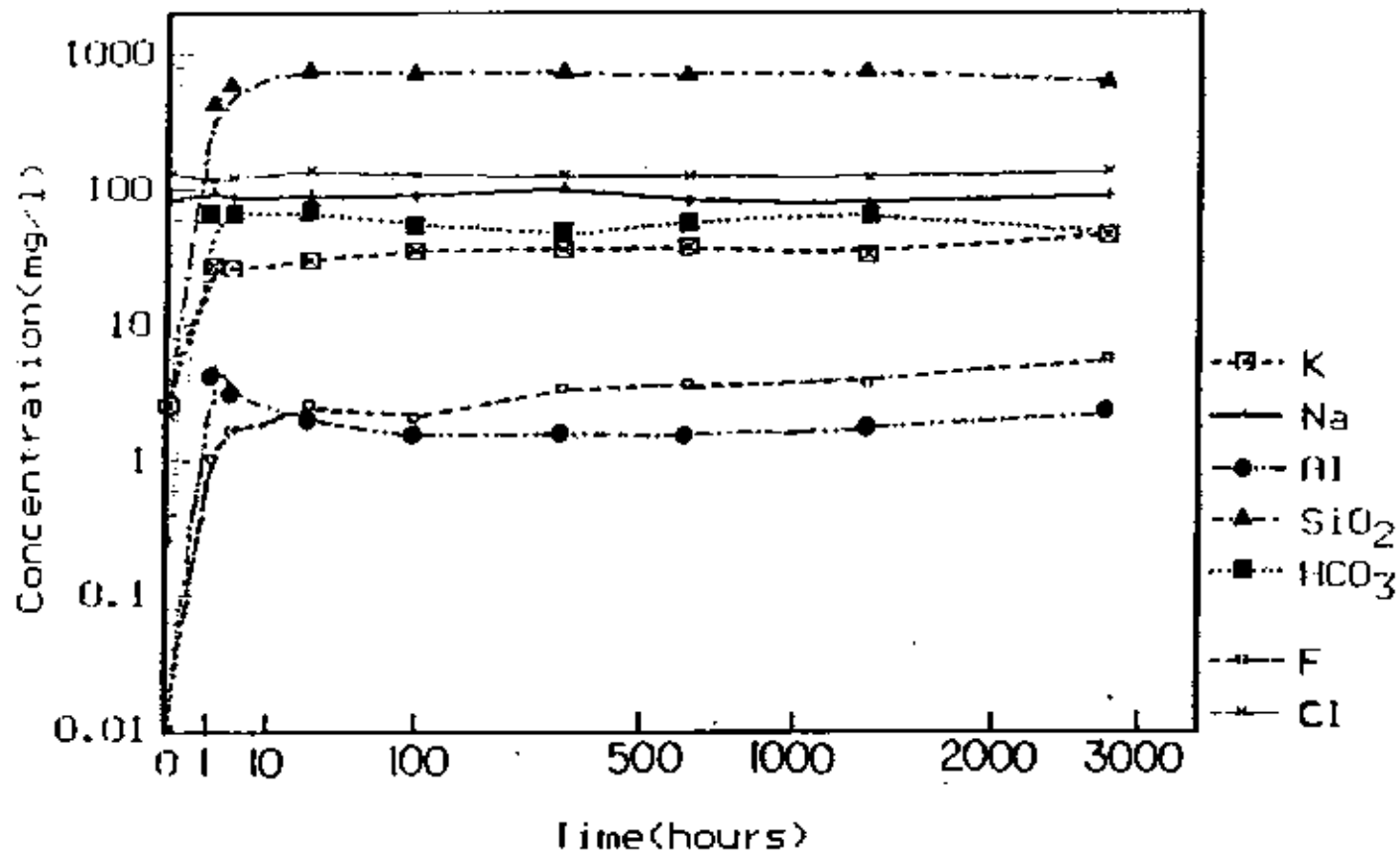


Figure 44: Concentration-time trends for major dissolved species in solution from the completed Conway Granite experiment (CO-2) conducted at 300°C and 300 bars.

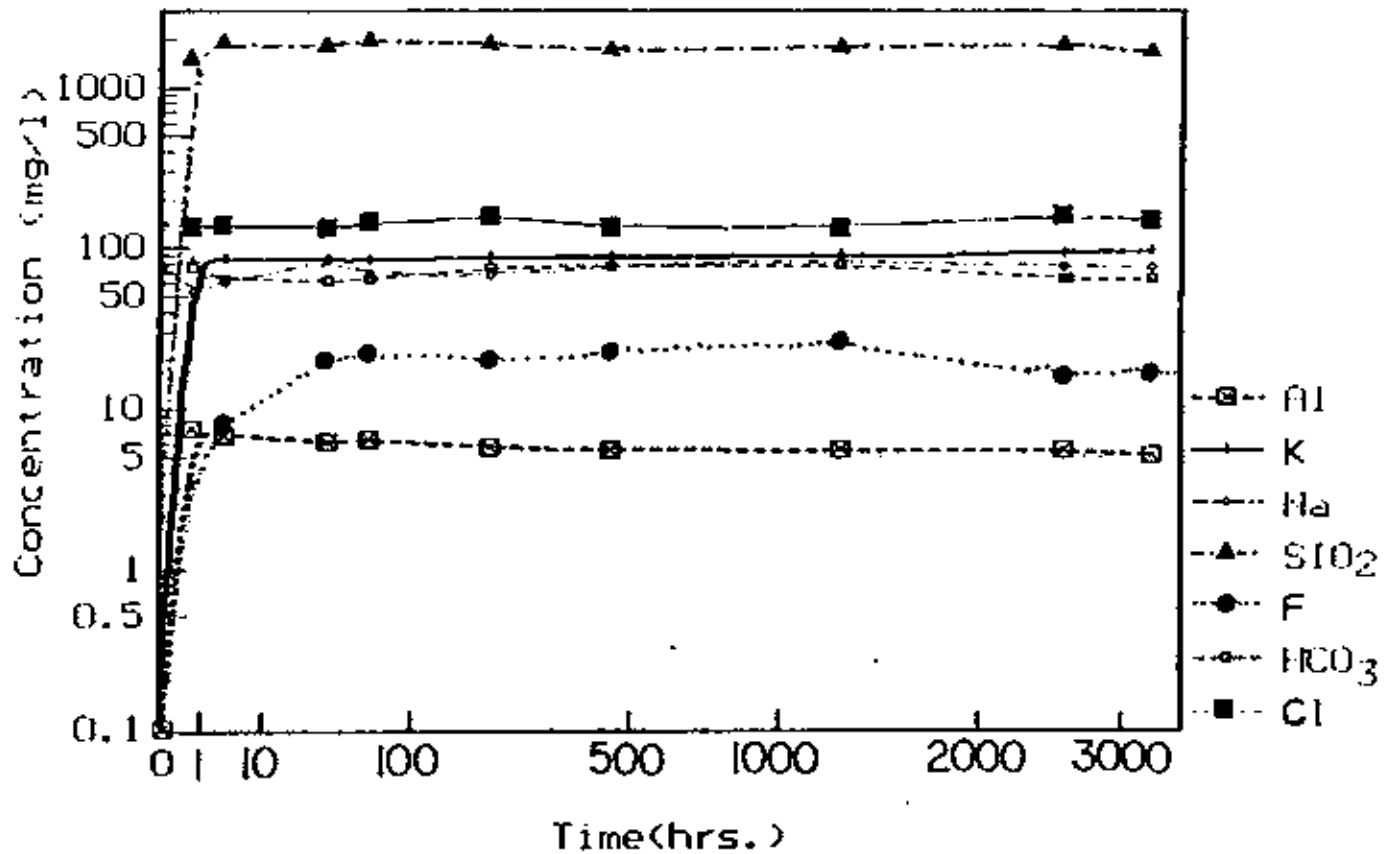


Figure 45: Concentration-time trends for major dissolved species in solution from the Bannock Rhyolite Tuff experiment (BRT:1) conducted at 300°C and 300 bars.

respectively. Figures 44-45 also show that during the 1 to 10 hour interval of both experiments, SiO_2 , K, Al, HCO_3 , and F trends approach stability (herein defined as species slopes \rightarrow 0 ppm/hour). The concentration of SiO_2 , K, F, and Al in BRT:1 solution was comparatively high during all time intervals (compared to CG:2).

FIGURES 44 AND 45: EXPERIMENTS CG:2 AND BRT:1

MAJOR SPECIES DATA COMPARISON: Two inferences can be drawn from the above data:

- 1) Zero to one hour minimum rate of major species release slopes are higher for experiment BRT:1. Assuming surface areas are equal, the rhyolitic glass contained within the tuff dissolved more rapidly than the quartz and feldspars in the granite (CG:2).
- 2) In both experiments, major species release slopes approach zero after the 10 hour interval. These results indicate that concentration trends for most species in both experiments are controlled by secondary mineral formation.

TREND COMPARISON

FIGURE 46: SiO₂ and K

SiO₂ DATA PRESENTATION: In experiment CG:2 the concentration of SiO₂ in solution rose sharply to 434 mg/l at one hour (CG 1.1). The concentration of SiO₂ in solution increased gradually to 604 mg/l by the 190 minute sample (CG 1.2). After sample CG 1.2 dissolved SiO₂ concentrations remained relatively constant (ranging from 617-753 mg/l).

In experiment BRT:1 the concentration of dissolved SiO₂ in solution sharply increased to 1493 ppm by the 30 minute sample. The concentration of SiO₂ in solution increased gradually to 1900 mg/l by the 190 minute sample (BRT 1.2). Following the 190 minute sample dissolved SiO₂ concentrations remained relatively constant (ranging from 1699-1997 mg/l).

SiO₂ DATA INTERPRETATION: The concentration of dissolved SiO₂ in CG 2.1 suggests that the granite solution had become slightly undersaturated with respect to quartz (CG 2.1: log IAP/K= -0.19) by the 1.4 hour sample. By the 3.2 hour sample SiO₂ concentrations stabilized near values consistent with quartz saturation (CG 2.2: log IAP/K= -0.05).

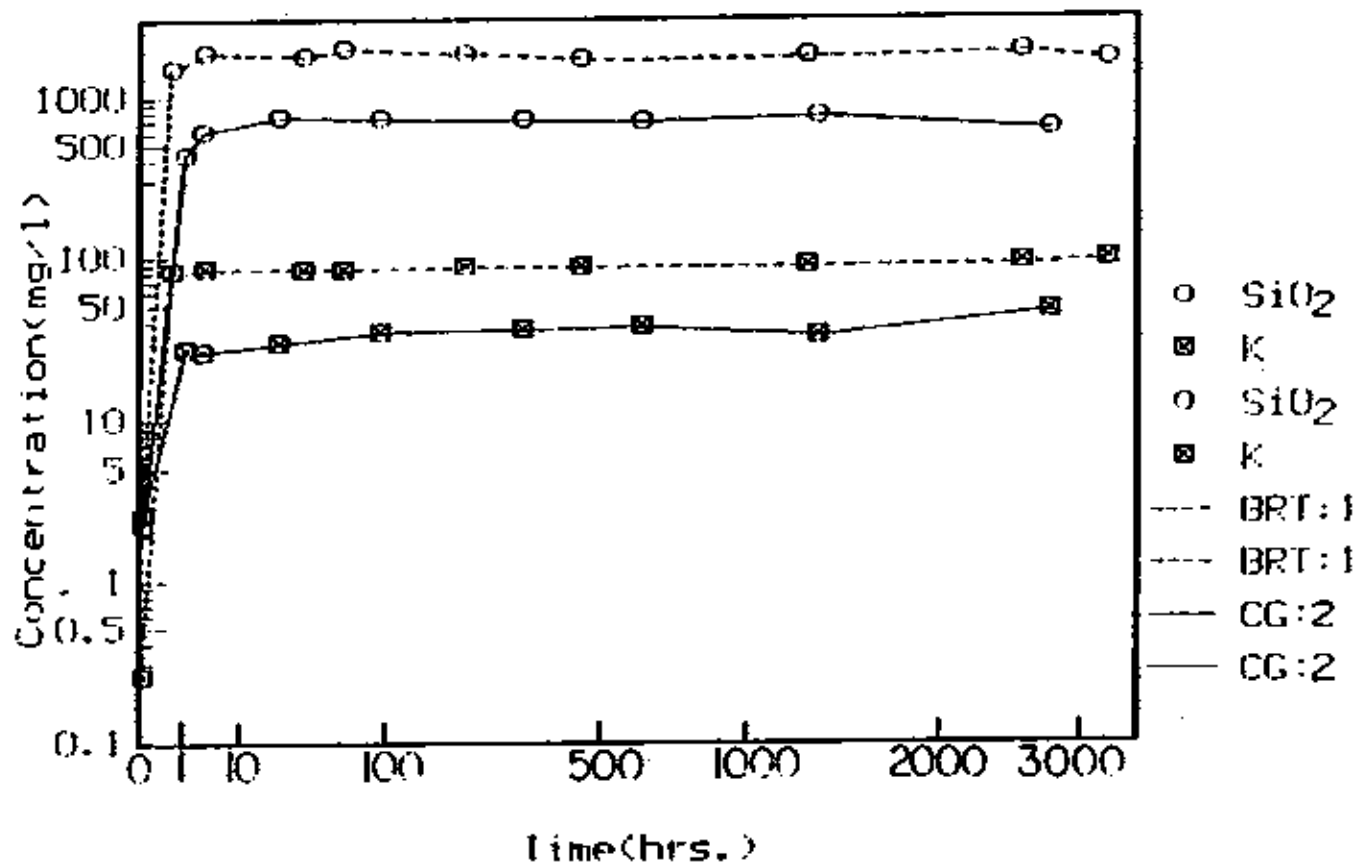


Figure 46: K and SiO₂ Concentration-time trends from the completed Conway Granite (CG:2), and Bannock Rhyolite Tuff (BRT:1) experiments conducted at 300°C and 300 bars.

Values measured throughout the rest of the granite experiment suggest that secondary quartz formation controlled dissolved SiO_2 concentrations (CG 2.3-2.8: $0.01 \leq \log \text{IAP/K} \leq 0.05$). The identification of secondary quartz (see Figure 29) in the CG:2 quench secondary mineral assemblage, and the above mentioned $\log \text{IAP/K}$ data, suggest that secondary quartz formation controlled dissolved SiO_2 concentrations in the granite experiments.

The concentration of dissolved SiO_2 in aliquot BRT 1.1 suggests that the tuff solution had become slightly undersaturated with respect to amorphous silica (BRT 1.1: $\log \text{IAP/K} = -0.07$) by the 1.4 hour sample. Within the first 3.3 hours of the tuff experiment dissolved SiO_2 concentrations stabilized near values consistent with amorphous silica saturation (BRT 1.2: $\log \text{IAP/K} = 0.03$). Values measured throughout the remainder of the tuff experiment suggest that amorphous silica formation controlled dissolved SiO_2 concentrations (BRT 1.3-1.10: $-0.01 \leq \log \text{IAP/K} \leq 0.05$). The identification of secondary amorphous silica (see Figure 8) in the BRT 1.2 secondary mineral assemblage, and the above mentioned $\log \text{IAP/K}$ data, suggest that amorphous silica formation controlled dissolved SiO_2 concentrations in the Tuff experiment.

A SEM photomicrograph (Figure 47) of a CG:2 quench solution etch-pitted primary quartz grain implies that quartz dissolution added SiO_2 to the granite solutions. The dissolution of primary feldspar is also thought to have contributed dissolved SiO_2 to the granite solutions. The dissolution of highly soluble rhyolitic glass is thought to have contributed the vast majority of dissolved SiO_2 added to the BRT:1 autoclave solution. Since the tuff glass is more soluble than the quartz and feldspars contained within the granite, the concentration of SiO_2 in solution is higher in experiment BRT:1. The effect of higher SiO_2 concentrations in experiment BRT:1 on solution pH, is discussed in the pH trends vs. time section.

K DATA PRESENTATION: In experiment CG:2 the concentration of K in solution increased rapidly to 27.0 mg/l (CG 1.1). After this initial sample dissolved K concentrations remained relatively constant (ranging from 26-45 mg/l).

In experiment BRT:1 the concentration of K in solution increased rapidly to 27.0 mg/l (BRT 1.1). The concentration of K in solution remained relatively constant throughout the rest of the experiment (ranging from 83.4 to 94.7 mg/l).



Figure 47: SEM photomicrograph of a etch-pitted primary quartz grain from the CG:2 quench aliquot.

K DATA INTERPRETATION: The concentration of K in solution, was comparatively higher in the tuff experiment. The EDS spectrum of a primary BRT glass fragment (Figure 5) suggests that rhyolitic glass dissolution added K into the tuff autoclave solution. Modal mineralogy analyses of primary Conway Granite (see Table 2) indicate that K-feldspar is the only possible contributor of K to the granite autoclave solutions. These comparisons suggest that the K-rich tuff glass is more soluble than the K-feldspar contained within the Conway Granite sample.

In both experiments illite formation is primarily responsible for removing K out of solution. In experiments BRT:1 and CG:2 K concentration trends stabilise by the 10 hour sample. These data indicate that secondary illite formation controlled K concentrations in both experiments.

FIGURE 48: F and Al

F DATA PRESENTATION: In experiment CG:2 the concentration of F in solution increased from 0.0 mg/l to 1.0 mg/l by the 1.36 hour sample (CG 2.1). After this sample F concentrations steadily

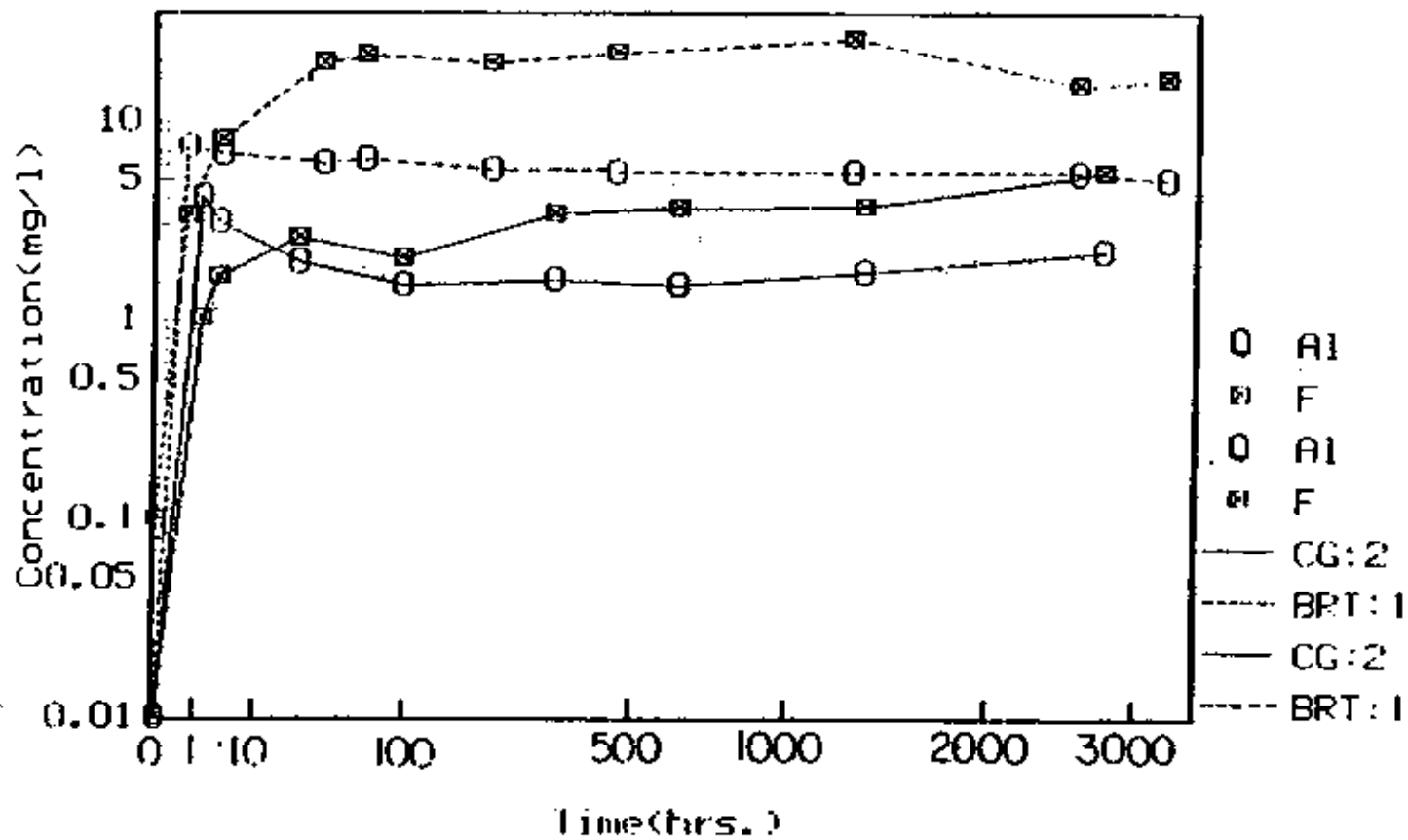


Figure 48: F and Al Concentration-time trends from the completed Conway Granite (CG:2), and Bannock Rhyolite Tuff (BRT:1) experiments conducted at 300°C and 300 bars.

increased, reaching 5.5 mg/l by the end of the granite experiment.

In experiment BRT:1 the concentration of F in solution steadily increased reaching a maximum of 26.07 mg/l by the 1264 hour sample. Afterwards the concentration of F in solution gradually decreased to 16.47 mg/l, by the 3531 hour sample (BRT 1.10).

F DATA INTERPRETATION: Fluorite is the only identifiable source of F in the Conway Granite sample. No fluoride-bearing minerals were identified in the CG:1 and CG:2 quench solution secondary mineral assemblages. Fluorite saturation indices suggest this mineral did not precipitate from the granite solution (see Table 4). The above mentioned data and the gradual increasing F trend suggest that the dissolution of primary trace fluorite continued throughout experiment CG:2. These data also indicate that fluoride-bearing secondary minerals may not have formed during the granite experiments.

The Bannock Rhyolite tuff sample contained no identifiable fluoride-bearing primary minerals. Therefore in the BRT:1 experiment the increasing F trend indicates that the dissolution of tuff glass was the source of this element in solution.

Fluorite saturation indices suggest this mineral did not precipitate from the tuff solution (see Table 4). Thus, the decreasing F concentration trend representing the latter segment of experiment BRT:1, is probably due to F substitution for hydroxyl ions in secondary smectite structures.

POSSIBLE NUCLEAR WASTE IMPLICATIONS: The concentration of F in repository solutions may be important in determining the reactions may responsible for controlling the solubility of UO_2 in spent fuel rods. If solution fluoride concentrations are high, and redox conditions are relatively oxidizing then uranium fluoride complexes may form (according to a phase diagram by McKeon (1984). In the redox comparisons section, $UO_2F_3^-$ is predicted to be the stable uranium complex formed in experiment BRT:1 (assuming solid UO_2 spent fuel were immersed in the tuff solution). These results suggest that uranium fluoride complex formation may occur if F-rich-glass-influenced repository solutions react with solid UO_2 spent fuel. If uranium fluoride complexes are stable in tuff repository solutions (i.e. Yucca Mountain, Nevada), then the solubility of solid UO_2 spent fuel will depend on the influence of F-rich rhyolitic

glass dissolution. If solutions are strongly influenced by F-rich rhyolitic glass dissolution, then solid UO_2 spent fuel should be more soluble.

Al DATA PRESENTATION: In experiment CG:2 the concentration of Al in solution increased from 0.0 mg/l to 4.2 mg/l during the 0.0 to 1.36 hour interval. After this interval F concentrations steadily decreased, reaching 2.2 mg/l by the end of the granite experiment.

The concentration of Al in BRT:1 solution rose to 7.4 mg/l by the 30 minute sample. After the 30 minute sample the concentration of Al in BRT:1 solution gradually decreased to 5.0 mg/l, by the 3531 hour sample (BRT 1.10).

Al DATA PRESENTATION: The source of Al in the granite solution is primarily microcline and albite. The EDS spectrum in Figure 5 suggests that rhyolitic glass dissolution is primarily responsible for the release of Al into BRT:1 solution. The concentration of Al in CG:2 solution is comparatively lower (than BRT:1) during all time intervals. The higher BRT:1 Al concentration trend are a result of the greater solubility of tuff glass (compared to CG:2 microcline and albite).

The general decreasing trend in both aluminum concentration curves is likely due to the incorporation of Al into aluminosilicate secondary mineral structures.

FIGURE 49: Cl and HCO₃.

Cl DATA PRESENTATION: The concentration of Cl in solution varies little when compared with starting values in both experiments.

Cl DATA INTERPRETATION: Since we found that none of the identified secondary minerals incorporate Cl into their structures, it is apparent that there is not a significant reactive Cl source in the tuff and granite samples.

HCO₃ DATA PRESENTATION: In experiment CG:2 the concentration of HCO₃ in solution increased from 0 mg/l to 63 mg/l by the 1.36 hour sample. After this sample, HCO₃ concentrations remained relatively constant (ranging from 45-67 mg/l).

The concentration of HCO₃ in BRT:1 solution increased from 0 to 75 mg/l by the 30 minute sample. The concentration of HCO₃ in BRT:1 solution

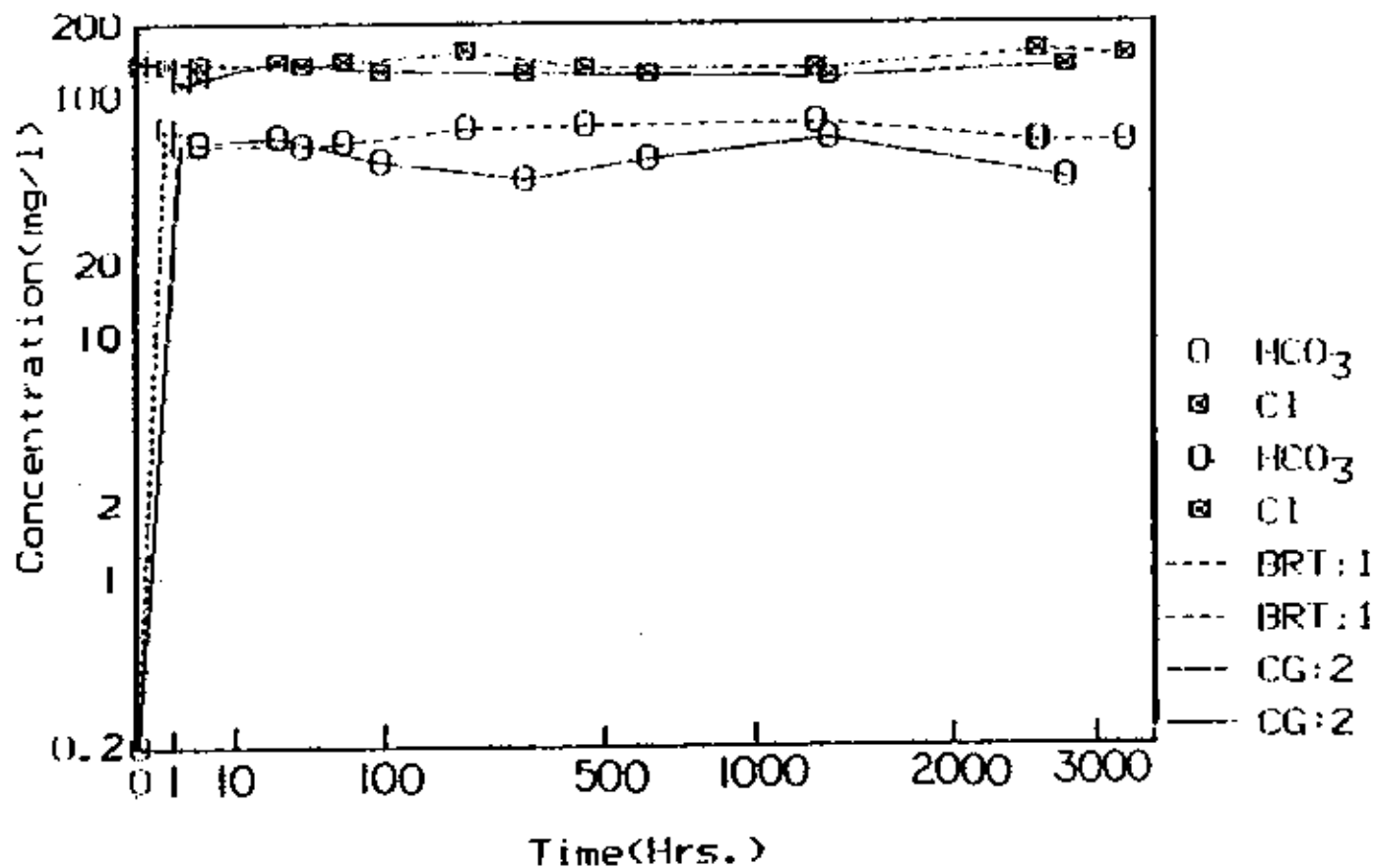


Figure 49: Cl and HCO₃ Concentration-time trends from the completed Conway Granite (CG:2), and Bannock Rhyolite Tuff (BRT:1) experiments conducted at 300°C and 300 bars.

remained relatively constant throughout the remainder of the experiment (ranging from 62 to 78 mg/l).

HCO₃ DATA INTERPRETATION: The increase in total dissolved carbonate concentrations during the initial intervals of experiments CG:2 and BRT:1 are probably due to the rapid dissolution of trace amounts of calcite.

FIGURE 50: Ca and Na

Ca DATA PRESENTATION: In experiment CG:2 the concentration of Ca in solution increased from 0 to 0.7 mg/l during the 0 to 1.4 hour interval. After the 1.36 hour sample Ca concentrations stabilized, fluctuating around a CG 2.4 to 2.8 average of 1.1 mg/l.

The concentration of Ca in BRT:1 solution increased from 0 to 2.6 mg/l during the 0 to 3.3 hour interval. After this initial increase Ca concentrations steadily decreased to 0.4 mg/l, by the 3531 hour sample (BRT 1.10).

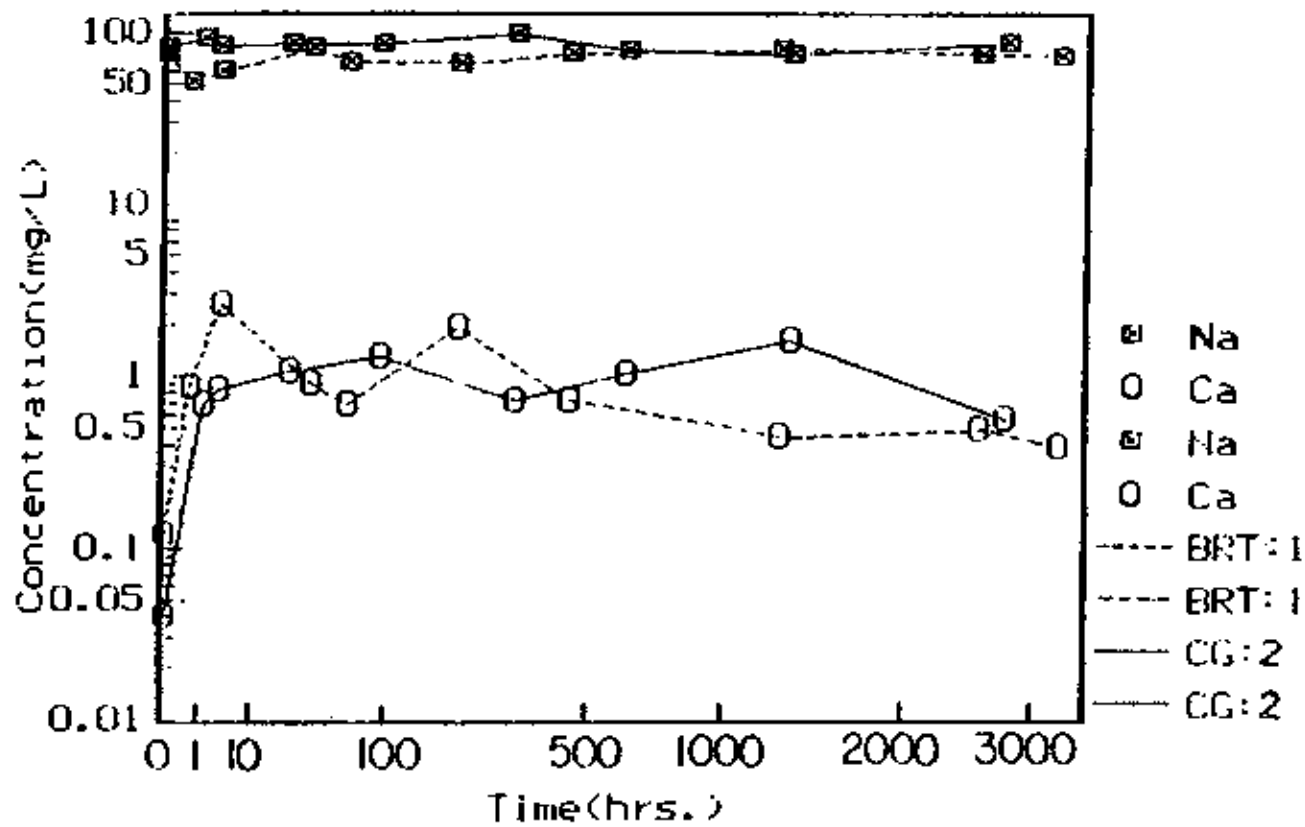


Figure 50: Ca and Na Concentration-time trends from the completed Conway Granite (CG:2), and Bannock Rhyolite Tuff (BRT:1) experiments conducted at 300°C and 300 bars.

Ca DATA INTERPRETATION: The initial Ca increase in the granite experiment was probably due to rapid dissolution of trace amounts of calcite identified in thin section analyses. There is not a detectable decreasing or increasing CG:2 Ca trend in Figure 50. From this it can be inferred that the rate of Ca release by albite, trace hastingsite, and fluorite is approximately equal to the rate of incorporation of Ca into secondary minerals. None of the EDS spectra of secondary smectites removed from the granite quench aliquots contain discernable Ca peaks (see Secondary Mineral Analyses Section; Figure 27-28). However, Ca concentrations in the CG:2 quench solution are approximately 8 times higher than the CG 2.4 to 2.8 average of 1.05 mg/l (see Table 5). These results suggest that Ca-bearing minerals may have become unstable during the quench process releasing Ca into solution. Calcite log IAP/K values stabilize close to zero implying that calcite may have been at equilibrium with the granite experiment solution.

Stable Ca tuff concentration trends are relatively low, and the EDS pattern of a rhyolitic glass fragment in Figure 5 does not contain a discernable Ca peak, suggesting that the rhyolitic

glass contains little calcium. The sharp increase in HCO_3^- during the initial intervals of BRT:1, suggest that the initial Ca increase in the tuff experiment was probably due to the rapid dissolution of trace amounts of calcite within the tuff. It is also possible that small amounts of Ca may have been released by the shattered plagioclase grains. The general downward trend in tuff solution Ca concentrations seems to be due to the precipitation of secondary anhydrite, and the incorporation of increasingly greater amounts of Ca into smectite structures (see Secondary Mineral Analyses section).

Na DATA PRESENTATION: The concentration of Na in solution varied little when compared with starting values throughout experiment CG:2.

In experiment BRT:1 the concentration of Na in solution decreases from 76.2 mg/l to 60.2 mg/l, from the 0.0 to 3.3 hour sample (BRT 1.2). After the 3.3 hour sample Na concentrations fluctuate between 66.6 to 83.3 mg/l (BRT 1.3-1.10).

Na DATA INTERPRETATION: The relatively constant CG:2 Na concentration trend slope suggests that the rate of Na removal from secondary mineral

precipitation, was approximately equal to the rate of Na release by the primary rock. In the secondary mineral assemblages removed from CG:1 and CG:2 quench aliquots, the only Na-bearing secondary mineral identified was high albite (see Secondary Mineral Analyses section). The only major Na-bearing secondary mineral identified from the primary Conway Granite sample powder was low albite (see Characterization of Secondary Minerals section). The EDS spectrum in Figure 51 was used to identify the reacted grain in the included SEM photomicrograph as micropertthite. EDS analyses of this grain, indicate that the valleys consist of albite (ridges are K-feldspar). This SEM photomicrograph suggest that primary low albite dissolution added Na into the CG:2 solution. The relatively constant Na slope, and these observations indicate that the rate of primary low albite dissolution, is approximately equal to the rate of secondary high albite formation.

Rhyolitic glass and shattered plagioclase grains contained within the tuff are probably responsible for the release of Na into the tuff autoclave solution. Some of the secondary clay minerals formed in the tuff experiment are Na-bearing (see Secondary Mineral Analyses section).

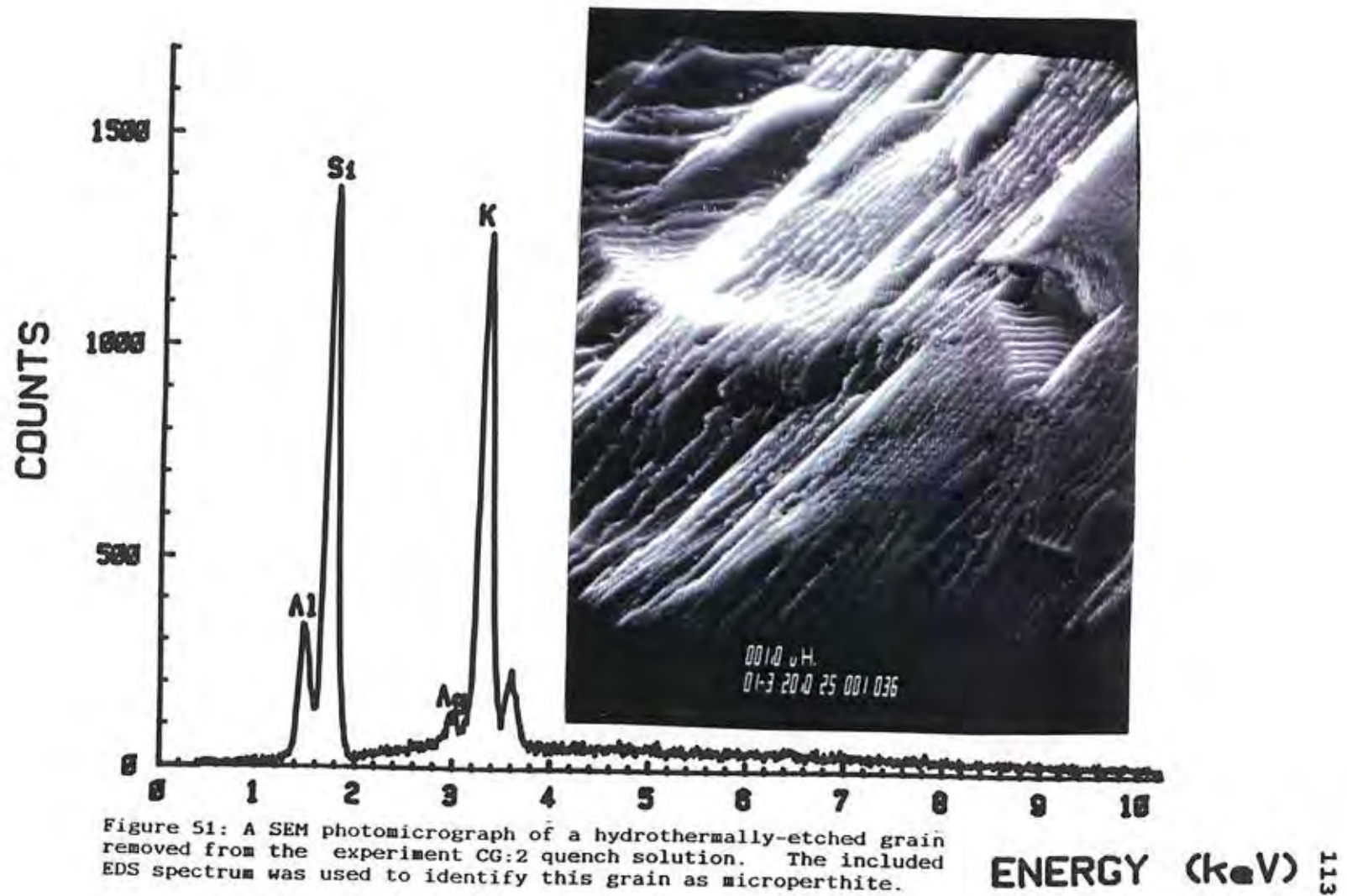


Figure S1: A SEM photomicrograph of a hydrothermally-etched grain removed from the experiment CG:2 quench solution. The included EDS spectrum was used to identify this grain as micropertthite.

The initial decrease in tuff experiment Na concentrations (BRT 1.0-1.2) indicates that during the 0 to 3.3 hour interval, the rate of Na removal by clay mineral precipitation was greater than the rate of Na addition by rhyolitic glass and plagioclase. The BRT 1.3 to 1.10 fluctuating trend (66.6 to 83.3 mg/l) indicates that the difference the low albite Na addition rate and high albite Na removal rate differed during the course of the tuff experiment.

FIGURE 52: SO₄ and H₂S

SO₄ DATA PRESENTATION: In the granite experiment SO₄ concentrations gradually increased from 0.5 mg/l in the starting solution, to 2.0 mg/l by aliquot CG 2.8 (2761 hour sample).

In the tuff experiment SO₄ concentrations rose sharply from 1 ppm in the starting solution, to approximately 4 mg/l by the 30 minute sample. After this initial sample, tuff experiment SO₄ concentrations gradually increased to 12.7 mg/l by BRT 1.10 (3531 hour sample).

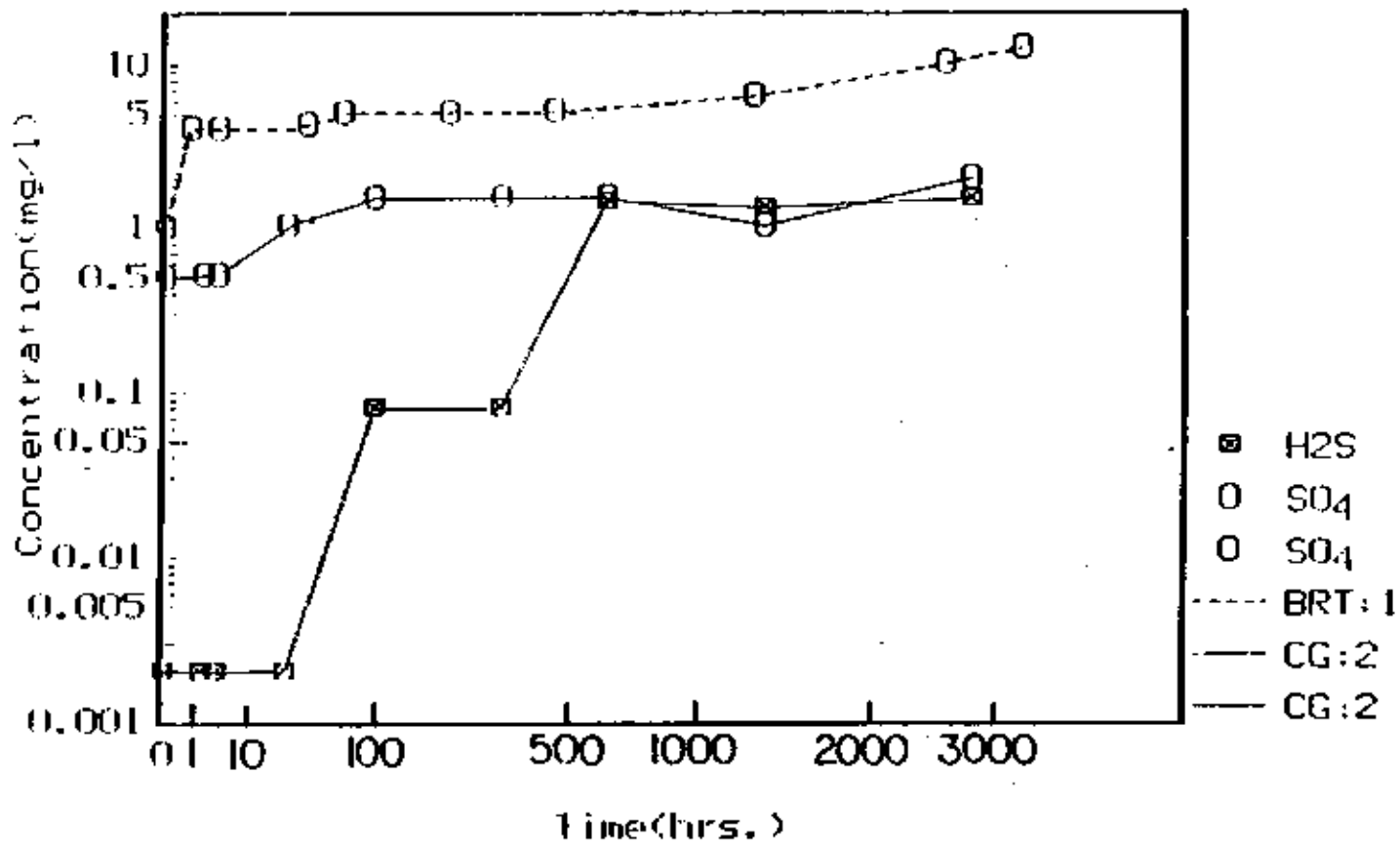


Figure S2: SO₄ and H₂S Concentration-time trends from the completed Conway Granite (CG:2), and Bannock Rhyolite Tuff (BRT:1) experiments conducted at 300°C and 300 bars.

SO₄ DATA INTERPRETATION: The only sulphur-bearing mineral identified in the primary Conway Granite sample is pyrite. The gradual increasing SO₄ concentration trend suggests that the trace amounts of pyrite contained within the granite sample had not been exhausted by the end of experiment CG:2.

No primary sulfide or sulphate minerals were identified in the unreacted tuff sample, suggesting that rhyolitic glass dissolution was responsible for the release of sulphate into the tuff solution. Experiment BRT:1 anhydrite saturation indices (log IAP/K values) increased from -0.68 to -0.04 during the 3.3 to 3531 hour interval. The identification of secondary anhydrite in aliquot BRT 1.7 (see Secondary Mineral Analyses section), suggests that secondary anhydrite had formed by the 1264 hour sample. These data indicate that secondary anhydrite precipitation controlled the concentration of SO₄ in the tuff autoclave solution.

H₂S DATA PRESENTATION: No H₂S was not detectable in the starting solution, and the first three sample aliquots removed from experiment CG:2. The lack of H₂S in these samples indicates that during the first twenty four hours of experiment BRT:1 the granite solution was too oxidized to allow for SO₄

reduction. The concentration of H_2S in CG:2 solution increased from 0.08 to 1.46 mg/l, during the 313 to 623 hour time interval. During this same interval the granite solution became 400 times more reduced with $\log fO_2$ decreasing from -26.4 to -29.0 (Table 6; see DHEM values). The concentration of H_2S in CG:2 solution reached 1.51 mg/l by the 2762 hour sample, as $\log fO_2$ decreased to -30.0. The oxidation of ferrous iron is thought to be primarily responsible for the removal of O_2 from autoclave solutions. These results suggest that SO_4 reduction primarily occurred due to the removal O_2 from the granite autoclave solution by ferrous iron. Throughout the course of the tuff experiment H_2S was not detected. The lack of detectable H_2S in the tuff solution indicates that conditions were too oxidizing throughout to allow for SO_4 reduction.

FIGURE 53: Fe and Mg

Fe DATA PRESENTATION: In experiment CG:2 Fe concentrations increase to 0.18 mg/l by the 1.4 hour sample. Throughout the rest of the granite experiment Fe concentrations remain relatively constant (ranging from 0.08 to 0.18 mg/l).

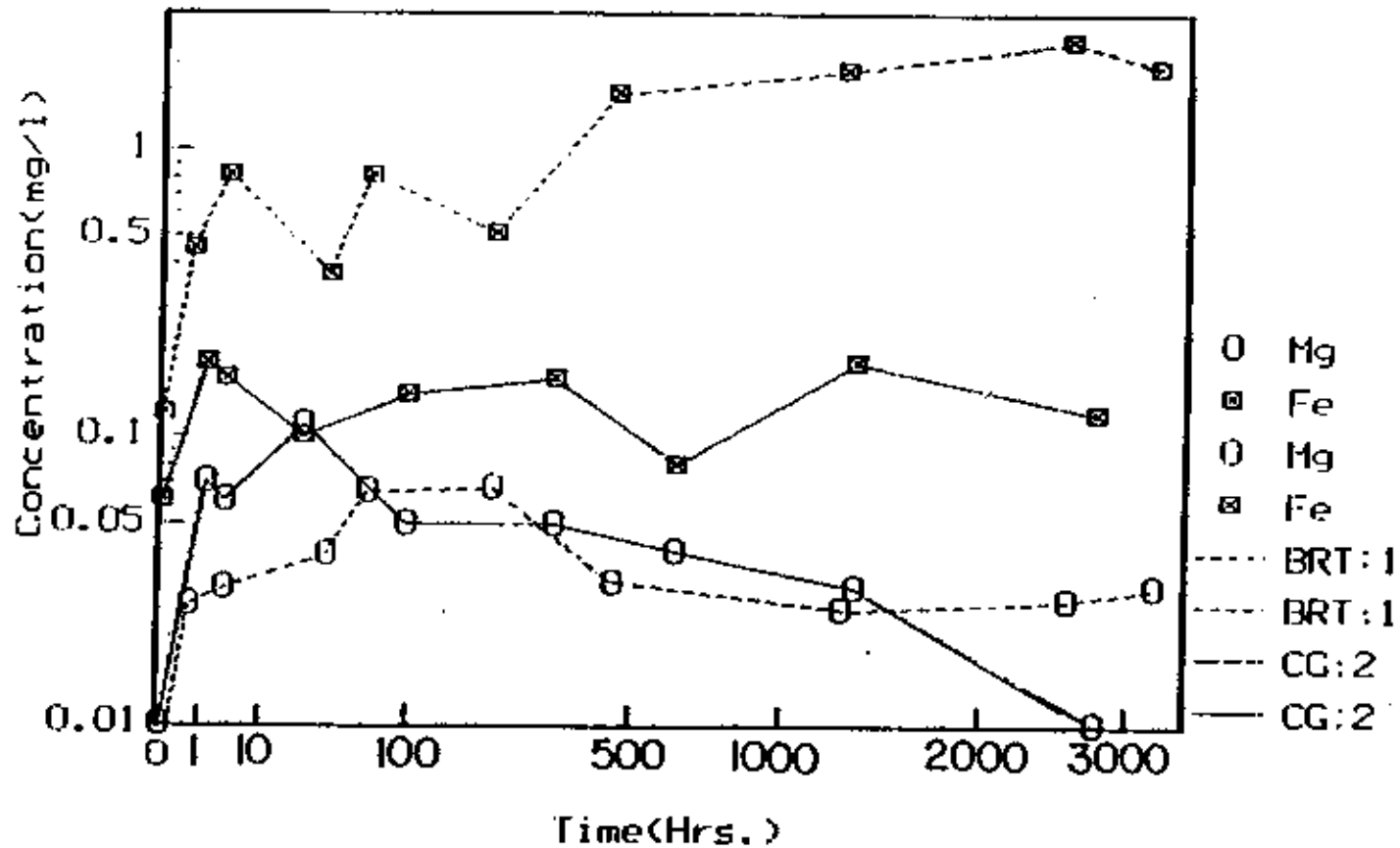


Figure S3: Fe and Mg Concentration-time trends from the completed Conway Granite (CG:2), and Barnock Rhyolite Tuff (BRT:1) experiments conducted at 300°C and 300 bars.

Tuff experiment Fe concentrations gradually increased from 0.1 ppm to 2.0 ppm (BRT 1.10).

Fe DATA INTERPRETATION: Biotite is the main Fe-bearing mineral contained within the Conway Granite sample. Trace amounts of other Fe-bearing minerals were also identified (hastingsite, magnetite and allanite). The relatively constant stable Fe concentration trend indicates that the rate of Fe release by biotite, hastingsite (tr.), magnetite (tr.), and allanite (tr.), is approximately equal to the rate of Fe incorporation, by hematite and clay minerals (illite and smectite).

In experiment BRT:1 Fe is primarily released into solution by the dissolution of rhyolitic glass. The gradual increasing Fe trend indicates that other cations (e.g. Ca, Na, K, Mg) replaced minor amounts of Fe contained within clay mineral structures (i.e. illite and smectites).

Mg DATA PRESENTATION: The concentration of Mg in solution was low throughout the tuff experiment (ranging from 0.01 to 0.07 mg/l).

Throughout the granite experiment the concentration of Mg in solution was also low (ranging from 0 to 0.11 mg/l).

Mg DATA INTERPRETATION: No Mg-bearing secondary minerals were identified from CG:2 and BRT:1 solutions using EDS/SEM and XRD techniques. These results suggest that little Mg was added to or removed from the tuff and granite solutions.

FIGURE 54: Mn and Li

Mn DATA PRESENTATION: In experiment BRT:1 the concentration of Mn in solution was low (0.02-0.03 mg/l).

The concentration of Mn in solution was also low throughout CG:2 (0.03 to 0.06 mg/l).

Mn DATA INTERPRETATION: No Mn peaks were discernable in the EDS spectra of clay minerals removed from the granite quench aliquots. These results are not surprising since the Conway Granite contained no appreciable Mn source.

The SEM/EDS spectra of some clay minerals removed from BRT:1 solution aliquots contain small Mn peaks. From this we can infer that the small amounts of Mn released from the initial rapid dissolution of rhyolitic glass, were rapidly incorporated into clay structures.

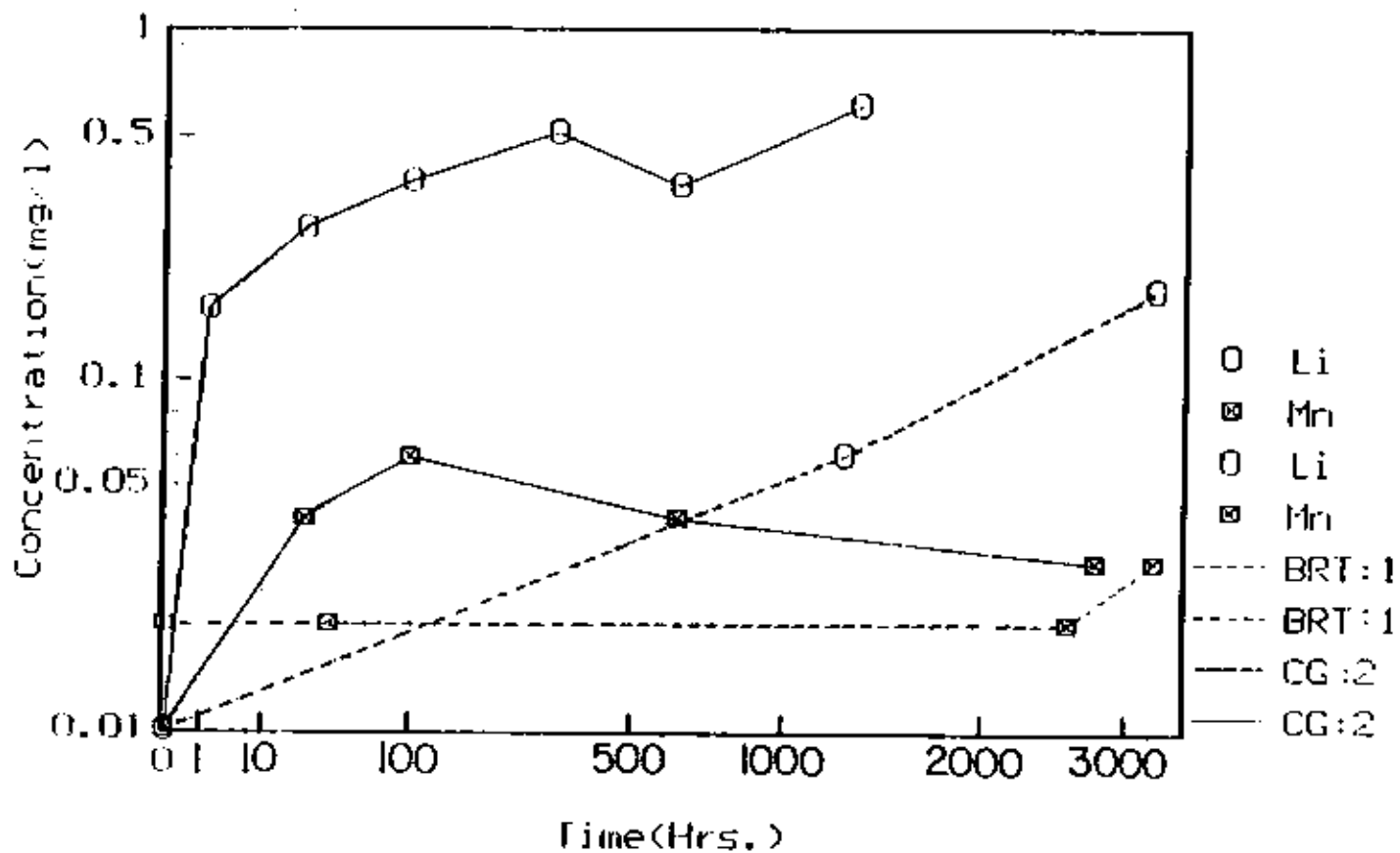


Figure 54: Mn and Li Concentration-time trends from the completed Conway Granite (CG:2), and Bannock Rhyolite Tuff (BRT:1) experiments conducted at 300°C and 300 bars.

Li DATA PRESENTATION: In experiment BRT:1 the concentration of Li in solution increased from 0.00 mg/l (CG 2.0) to 0.18 mg/l by the 3531 hour sample. In experiment Li CG:2 concentrations slowly but gradually rose from an initial value of 0 mg/l to 0.5 mg/l by the 2761 hour sample.

Li DATA INTERPRETATION: Gradual increasing Li concentration trends have also been observed in other granite autoclave experiments (i.e., Dickson, 1977; Savage, 1987). The small increase in CG:2 Li concentrations is probably the result of feldspar dissolution.

Li-bearing primary minerals were not identified in the composition analyses of the Bannock Rhyolite Tuff sample rock. Consequently, rhyolitic glass dissolution seems to be responsible for releasing minor amounts of Li into the tuff autoclave solution.

REDOX COMPARISONS**GRANITE EXPERIMENT (CG:2): DHEM AND SO₄/H₂S****REDOX TREND COMPARISON**

Figure 55 compares CG:2 log fO₂ values calculated using the SO₄/H₂S and dissolved hydrogen evolution (DHEM) methods. The SO₄/H₂S method assumes that redox equilibrium exists between the sulphur species (SO₄ + 2H⁺ = H₂S + 2O₂). The source of SO₄ and H₂S released into CG:2 solution is probably trace pyrite (identified during thin section analyses). The DHEM method (Kishima and Sakai, 1984, Ulmer *et al.*, 1985, Grandstaff *et al.*, 1985) assumes that dissolved H₂ is in equilibrium with oxygen and water. Granite log fO₂ values were calculated from CG 2.5-2.8 (313 to 2761 hour sample) using the above methods.

DATA PRESENTATION: The CG 2.5 aliquot log fO₂ values calculated using the DHEM (-26.4) and H₂S/SO₄ (-29.9) method differ by 3.5 orders of magnitude. Figure 55 shows that the difference between DHEM and SO₄/H₂S calculated log fO₂ values decreases with time. A minimum difference of 1.2 log fO₂ units was

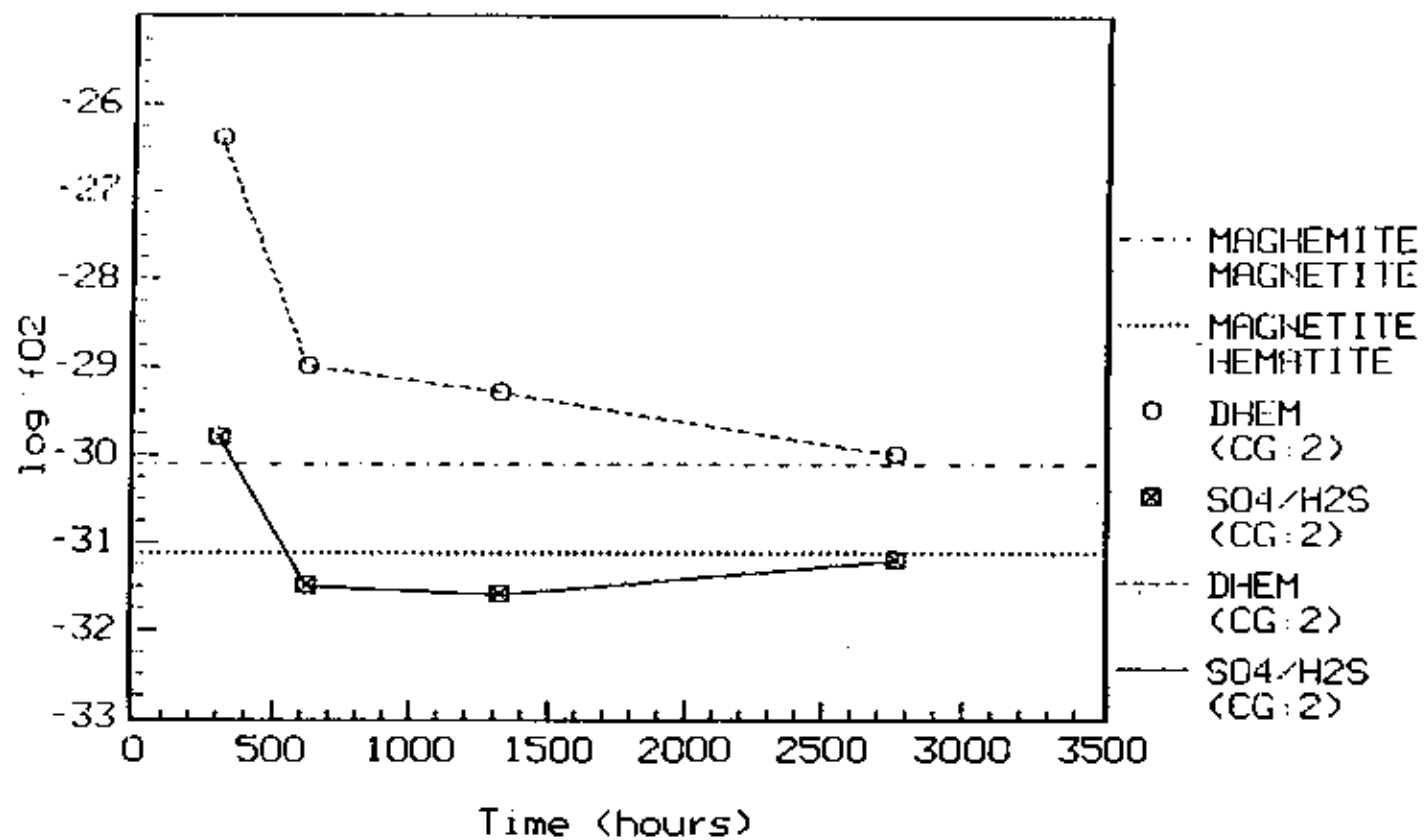


Figure 55: Comparison of CG:2 DHEM and SO₄/H₂S oxygen fugacity trends.

calculated from the final CG:2 aliquot (CG 2.8: DHEM= -30.0, SO_4/H_2S = -31.2).

DATA INTERPRETATION: Larger disparities between DHEM and SO_4/H_2S values are common during the initial periods of 300°C Dickson rocking autoclave experiments (Grandstaff *et al.*, 1985; Gardiner *et al.*, 1989). The initial larger disparity may result from oxidation/reduction kinetics for SO_4/H_2S , that are more sluggish than the H_2/H_2O kinetics. The SO_4/H_2S reaction rate is relatively slow (Ohmoto and Lasaga, 1982; Gigyanbach, 1987). Therefore, the DHEM values probably more reliably represent the redox state of the granite experiment solution.

Both sets of calculated values (excluding the CG 2.8 SO_4/H_2S data point) indicate that the Conway Granite sample rock continued to remove O_2 from solution, throughout the course of experiment CG:2. Brick-red secondary hematite coated the CG:1 quench secondary mineral assemblage (see Secondary Mineral Analyses section). The presence of this coating suggests that the oxidizing conditions necessary for the precipitation of hematite existed during the first 108 hours of experiment CG:2. The secondary mineral assemblage removed from the CG:2

quench aliquot is not coated by hematite. This comparison suggests that the larger amounts of hematite present during earlier time intervals had become unstable, due to more reducing solution redox conditions. The overall narrowing trend of these two sets of measurements suggest an eventual convergence of values.

TUFF (BRT:1) EXPERIMENT REDOX CONDITIONS AND
COMPARISONS WITH THE COMPLETED GRANITE
AUTOCLAVE EXPERIMENT (CG:2), TEMPLE BASALT
AUTOCLAVE EXPERIMENTS, AND GEOTHERMAL FIELDS

Figure 56 is a plot of oxygen fugacity values obtained from the tuff (BRT:1), granite (CG:2), previous Temple basalt experiments, and geothermal fields. The DKEM method was used to calculate $\log f_{O_2}$ in the tuff and basalt experiments. The dashed line and squares represent the tuff redox trend and individual values. The solid line and filled circles are used to represent the granite redox trend and individual f_{O_2} values. The bracket included on the bottom of Figure 56 represents the range of stable f_{O_2} values calculated from previous Temple 300°C basalt experiments, and 270-320°C

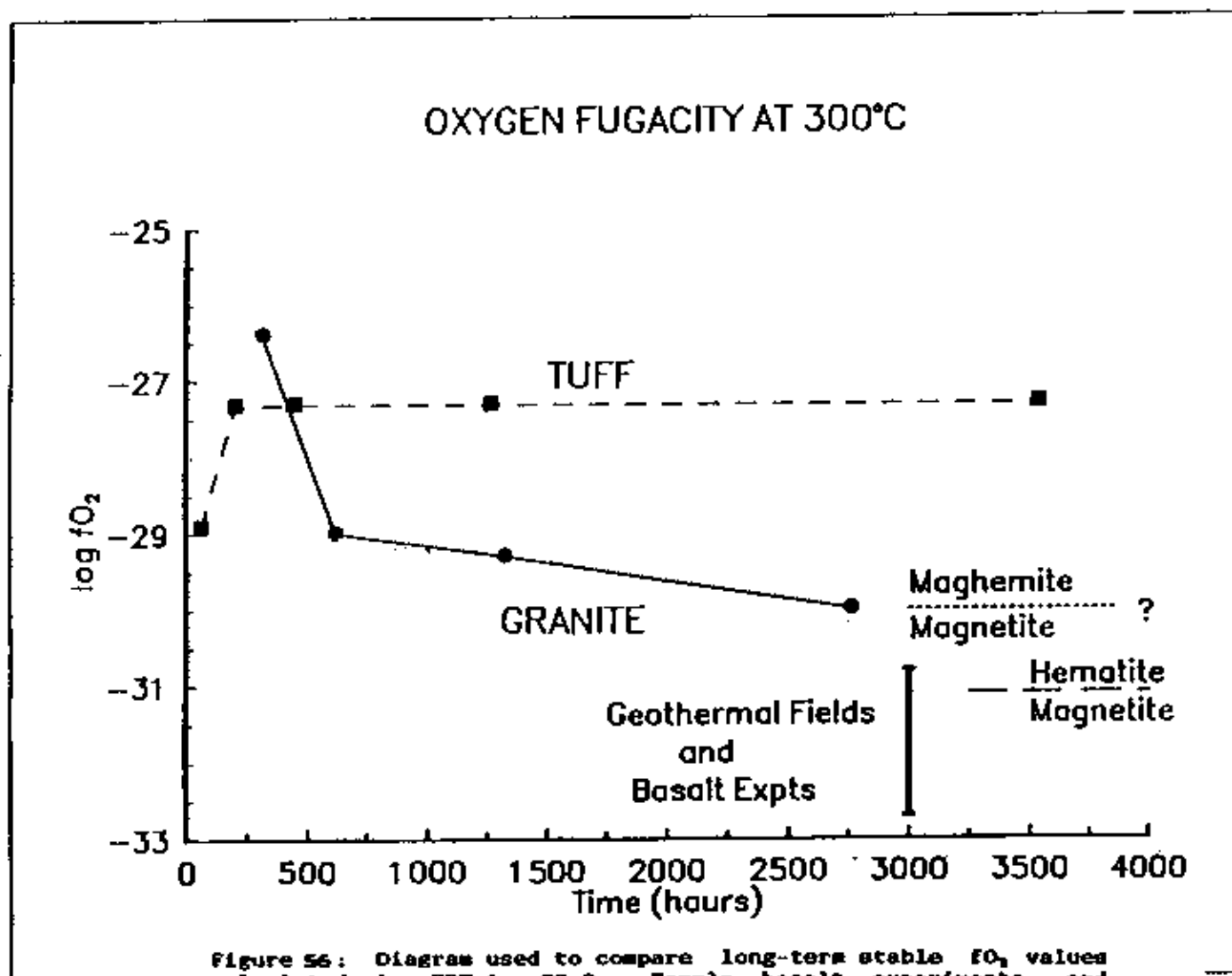


Figure 56: Diagram used to compare long-term stable fO_2 values calculated in BRT:1, CG:2, Temple basalt experiments, and geothermal fields.

geothermal solutions (Kacandes, 1989). This data was obtained from geothermal fields in Iceland, New Zealand, Kenya, Hawaii, Japan, Guatemala, Mexico, Idaho, and the Philippines. The rock types in contact with the above geothermal solutions include; basalt, granite, rhyolite, andesite, and sediment. The source waters present in these fields include all types from low salinity to seawater. For additional information on the characteristics of these geothermal fields see Kacandes (1989).

DATA PRESENTATION: Calculated values of $\log f_{O_2}$ decreased during the entire granite experiment. Experiment CG:2 $\log f_{O_2}$ decreased to -30.0 by the final sample (2762 hour sample).

The calculated $\log f_{O_2}$ of solution removed from aliquot BRT 1.4 is -28.92. Redox measurements taken from BRT 1.5-1.10 solution aliquots are constant (-27.3).

Calculated $\log f_{O_2}$ values from 270-320°C geothermal fluids range from -31 to -33. The stable f_{O_2} trends of 300°C Temple basalt experiments reach the magnetite-hematite boundary ($\log f_{O_2} = -31.0$ at 300°C (Helgeson *et al.*, 1978)), within 2700 hours (*i.e.*, Gardiner, 1988; Kacandes, 1989).

Temple basalt (300°C) autoclave experiment stable log f_{O_2} values fall within the range of geothermal fluids, near the magnetite-hematite boundary (-31 to -33).

THE REMOVAL OF O_2 FROM CG:2, BRT:1, AND 300°C TEMPLE BASALT AUTOCLAVE SOLUTIONS: The solution initially added to the gold reaction vessel in Dickson rooking autoclave experiments is saturated with oxygen from the atmosphere (ca. 8 mg/l at 20°C). In autoclave experiments solution f_{O_2} primarily decreases as a result of the oxidation of ferrous iron (Grandstaff and Ulmer, 1985).

The EDS pattern of unreacted glass in Figure 5, and the 95% volume of glass per whole rock value (see Table 2) suggest that rhyolitic glass is the primary source of the 0.43% FeO contained within the tuff. Trace Fe-rich-olivine identified in the tuff starting material is a minor source (<.1%). The rate of glass dissolution is higher when compared with most crystalline materials. These results suggest that rhyolitic glass dissolution and concomitant release of Fe^{2+} release was primarily responsible for the removal of O_2 from the BRT:1 solution, as the ferrous iron was oxidized. No H_2S was produced in experiment BRT:1, suggesting

that the small amount of Fe^{2+} contained within the tuff glass did not remove enough O_2 from solution to allow for SO_4 reduction (see SO_4 and H_2S trend diagram; Figure 52).

The lack of H_2S formation and the probable reaction with ferrous iron during initial time intervals, imply that the actual BRT 1.4 solution $\log f\text{O}_2$ was at least as oxidizing as the BRT 1.5 aliquot (-27.3). Problems with H_2 standardizing during the $f\text{O}_2$ analysis of aliquot BRT 1.4 may also have resulted in the calculation of this seemingly more reducing value.

Finally the stable BRT 1.5-1.10 $\log f\text{O}_2$ trend suggests that rhyolitic glass ceased to remove O_2 from solution within the first 204 hours of the tuff experiment.

The continued decreasing CG:2 $\log f\text{O}_2$ trend suggests that oxidation of ferrous iron removed O_2 from solution throughout the course of the experiment. Electron-microprobe studies indicate that biotite flakes in the red-phase Conway Granite contain a mean value of 40.8% FeO (Whitney and Stormer, 1976). Using this mean FeO value and the 4% volume value (see Characterization of Starting Materials section) the calculated percentage of FeO contained within biotite is approximately 66% of

the total in the whole rock. The remainder is contained within trace hastingsite, magnetite, pyrite, and allanite. The oxidation of ferrous iron contained within these minerals should be responsible for the decreasing CG:2 log f_{O_2} trend.

Rapid dissolution of basalt mesostasis is thought to be responsible for the removal of O_2 from the solutions in the Temple basalt experiments (Kacandes, 1989). The FeO-bearing components in basalt mesostasis which dissolve most rapidly are the strained glass surrounding Fe-Ca-P rich microspherules (Wang *et al.*, 1989). Numerous Fe-Ca-P microspherules were identified within unreacted basalt starting material, used in re-injection autoclave experiments (Gardiner, 1988). However few Fe-Ca-P microspherules were identifiable in the reacted primary basalt material removed from these experiments (Personal communication, Dr. Gene C. Ulmer, Temple University). These results suggest that O_2 was primarily removed from basalt:water experiments by Fe-Ca-P microspherules and rapidly dissolving glass (surrounding the microspherules).

Redox trend comparisons indicate that basalt:water experiment (300°C) f_{O_2} trends become more reducing at a faster rate, compared to experiment CG:2. These comparisons suggest that

basalt mesostasis (glass and Fe-Ca-P microspherules) removed O_2 from solution at comparatively more rapid rates (when compared to Conway Granite FeO-bearing primary minerals and Bannock Rhyolite Tuff glass).

IMPLICATIONS FOR THE USE OF AUTOCLAVE SOLUTION fO_2 TRENDS IN THE PREDICTION OF LONG-TERM GEOTHERMAL FIELD AND HIGH-LEVEL NUCLEAR WASTE REPOSITORY REDOX CONDITIONS: The constant BRT 1.5 to 1.10 redox trend indicates that the stable BRT:1 experiment fO_2 is -27.3. Temple 300°C basalt experiment stable log fO_2 values range from -31 to -33. The decreasing experiment CG:2 log fO_2 trend implies that redox conditions would become more reducing if the duration of the experiment had been extended. From previous Temple basalt autoclave experiments we infer that granite log fO_2 values would have continued to decrease, stabilizing near the magnetite-hematite boundary (-31 to -33).

Predicted stable log fO_2 values calculated from the 300°C granite experiment (CG:2), 300°C Temple basalt:water experiments, and geothermal fields fall within the -31 to -33 bracket, suggesting that these experiments are useful in predicting the long-term redox conditions of 300°C repository solutions. The stable fO_2 values calculated from

experiment BRT:1 do not fall within the geothermal field bracket. The geothermal field bracket in Figure 56 includes tuff data from New Zealand. This discrepancy between New Zealand values and stable BRT:1 fO_2 values, and the low redox buffering capacity of tuff (in general), indicate that the solutions flowing through the New Zealand site were initially more reducing (than the tuff autoclave solution).

A high-level nuclear waste repository can be thought of as a man-made non-magmatic geothermal field (Xacandes, 1989). Therefore granite (CG:2), tuff (BRT:1), and basalt experimental results should be useful in predicting the stable redox conditions existing at a high-level nuclear waste repository.

Experiment BRT:1 stable solution fO_2 values (~ -27.3) suggest that the fO_2 produced in a high-level nuclear waste repository may be 3 to 5 orders more oxidizing when compared with holocrystalline granite or basalt. The possible exhaustion of Topopah Spring Tuff formation glassy-horizon redox buffering capacity by infiltrating oxidizing groundwater may result in stable fO_2 values much higher than -27.3 . This possibility is further discussed in the following subsection.

REDOX BUFFERING CAPACITY CALCULATIONS

Redox buffering capacity values were calculated for 1 gram of Bannock rhyolite tuff (.43%), Conway Granite (2.47%), and mean basalt using (7.13%) FeO weight percentage values (Table 2). These data were plotted in Figure 57 to compare the redox buffering capacity of Bannock Rhyolite Tuff, Conway Granite and basalt at solution temperatures ranging from 0-350°C. The mean basalt ferrous iron value is based on analyses of 3761 basalt samples recovered from the 7 continents (LeMaitre, 1976). These values represent maximum redox buffering capacity values, since they are based on the assumption that all of the ferrous iron present in the rocks would eventually be oxidized. Solubility values of O₂ in solution were calculated for temperatures ranging from 0° to 350°C using Henry's constants tabulated by (Naumov, 1974). The effect of pressure on Henry's constant was not included in the calculation since the effect is infinitesimal, when considering solutions with pressures not ranging in the kilobar range (Naumov, 1974). The possible effect of glass-rich tuff, granite, and basalt redox buffering capacity on long-term solution

THE REDOX BUFFERING CAPACITY OF 1g OF B.
R. TUFF, C. GRANITE, AND MEAN BASALT
(LEMAITRE, 1976) BASED ON O₂ SOLUBILITY
DATA (MOUMOV, 1974) & FeO (WT.%) VS. TEMP

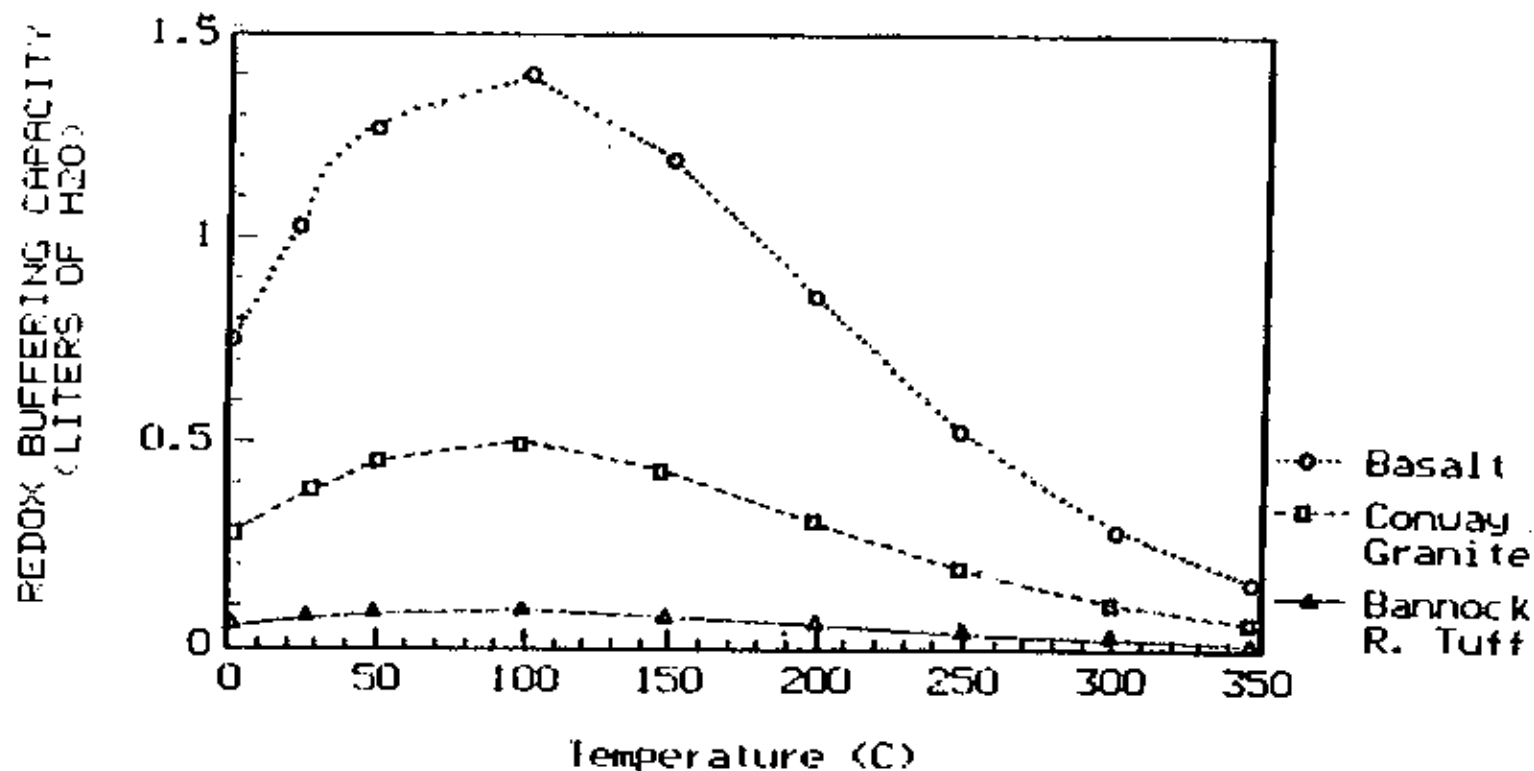


Figure 57: Diagram used to compare the calculated redox buffering capacity (based on FeO wt. %) of 1 gram of Conway Granite, Bannock Rhyolite Tuff, and average basalt (Lemaitre, 1976), from 0 to 350°C.

redox, radionuclide leakage into groundwater, and container corrosion at a high-level nuclear waste repository will be evaluated.

If we assume that all of the ferrous iron contained within the tuff can be oxidized by the 300°C solution, then 1 g of tuff is capable of removing dissolved O₂ from 290 ml of oxygen saturated solution. The initial concentration of oxygen in both solutions was 8 mg/l (log fO₂ = -0.7). The initial solution volume was 160 ml. Using these values the gold reaction cell contained approximately 4x10⁻⁵ moles of O₂ at the beginning of the experiments. If the 0.0688 grams of FeO contained within the BRT glass is distributed homogeneously and oxidized completely to Fe₂O₃ following the reaction:

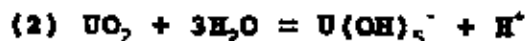


then the redox buffering capacity would be exhausted after 6-160 ml. reinjections of fresh solution. The redox buffering capacity of the granite is almost 6 times higher than the above calculated tuff value throughout the 0-350°C temperature range. The actual redox buffering capacity of the granite may be lower depending on the reactivity of the FeO-bearing minerals contained within the sample (biotite, hastingsite

(tr.), magnetite (tr.), pyrite (tr.), and allanite (tr.)). The calculated mean basalt redox buffering capacity values are approximately 3 times higher than the granite and 16 times higher than the tuff, at temperatures ranging from 0° to 350°C.

More oxidizing solutions percolating through a high-level nuclear waste site may result in increased UO_2 component spent fuel rod solubility. A pH-log fO_2 phase diagram for uranium species in solution (McKeon, 1984) was used to predict which U-complexes would form in repository solutions similar to those formed in experiments CG:2 and BRT:1. Predicted CG:2 and BRT:1 uranium complexes are evaluated to determine the possible influence of solution redox on the solubility of UO_2 (within spent fuel rods), in granite and tuff repository solutions. Using this diagram (at 300°C for example) the dominant uranium species present at a pH of 6.5 in the tuff experiment would be $UO_2F_3^-$. The dominant uranium species present at a pH of 6.6 in the granite experiment would be $U(OH)_5^+$. Approximately 96.1 (wt.%) of the uranium species contained within spent fuel pellets (based on the average spent fuel rod discharged from a reactor and stored for 10 years) consist of UO_2 , (McKeon, 1984; Woodley et al., 1981). If the (1) tuff and

(2) granite dissolved uranium species are in equilibrium with solid UO_2 spent fuel, then the concentration of dissolved uranium in solution can be expressed by these reactions:



The formation of $U(OH)_5^-$ (predicted to be present if the granite solution reacted with solid UO_2 spent fuel), would not be affected by solution redox changes. However pH changes at a granite enclosed high-level nuclear waste repository would affect the solubility of $U(OH)_5^-$ (see pH Trends vs. Time section). The Bannock Rhyolite Tuff has a low redox buffering capacity suggesting that the redox buffering capacity of Paintbrush Tuff formation glassy horizons would be quickly exhausted by the infiltration of oxidized groundwater. If reaction (1) were to occur at the Yucca Mountain site, then the amount of $UO_2F_3^-$ released into Yucca Mountain groundwater by UO_2 for spent fuel rods should be higher in glass-influenced solutions. For example if the $\log fO_2$ of a glass-influenced solution in contact with UO_2 solid spent fuel were to become 3 log units more oxidizing than $UO_2F_3^-$ concentrations may increase by a factor of 32. The possible influence of pH on $UO_2F_3^-$ concentrations within

glass-influenced solutions at the Yucca Mountain repository is discussed in the pH vs. Time section.

The stability of metallic waste containers in percolating repository solutions would be dependent on solution redox conditions. Low-carbon steel and stainless steel are considered to be the prime candidates for use as waste containers. The log f_{O_2} trend data obtained from CG:2 and Temple basalt experiments suggest that granite and basalt repository solutions near waste containers, will have stable redox values near the magnetite-hematite phase boundary (-31 to -33). Under these condition metallic iron alloys will probably corrode in groundwater with time releasing radionuclides. Therefore to delay waste container corrosion, other materials are being considered for use as container material.

At Temple University, for example Dickson rocking autoclave experiments were conducted to determine the suitability of copper as a waste container material (Lasaar, 1988). At 300°C and 300 bars pure copper will be oxidized as solution log f_{O_2} increases above -23.1 (Helgeson *et al.*, 1978). The predicted stable f_{O_2} results of experiment CG:2, Temple basalt experiments, and the above mentioned copper hydrothermal stability research suggest that

uncontaminated copper would be a suitable container material. However, experiment BRT:1 data analyses suggest that the redox buffering capacity of rhyolitic glass would be exhausted faster than crystalline material by oxidizing solutions. These results suggest that if glass-influenced solutions come into contact with pure copper waste containers, rapid corrosion may occur resulting in the release of radionuclides into repository groundwater.

pH TRENDS VS. TIME

Figure 58 is a plot of granite (CG:2) and tuff measured pH vs. time. In both experiments, solution pH (at room temperature and pressure) was analyzed within 5 minutes after the removal of each sample aliquot. Measured pH values and other solution parameters were input into the computer program H1PHPR2 (Kacandes and Grandstaff, 1989; Grandstaff et al., 1989) to determine calculated pH values (high-temperature pH). Figure 59 is a plot of calculated pH vs. time for the granite and tuff experiment. The horizontal dotted line represents neutral high-pressure, high-temperature pH at 5.5. Calculated CG:1 pH values (not plotted) are very similar to CG:2 values suggesting that these results are reproducible (see Tables 6,8).

FIGURE 58: MEASURED pH TRENDS

The tuff and granite starting solution measured pH values were identical at a value of 5.64. Measured pH increased to 6.44 by the 1.36 hour sample of the granite experiment. Within the first 3.17 hours of the granite experiment the

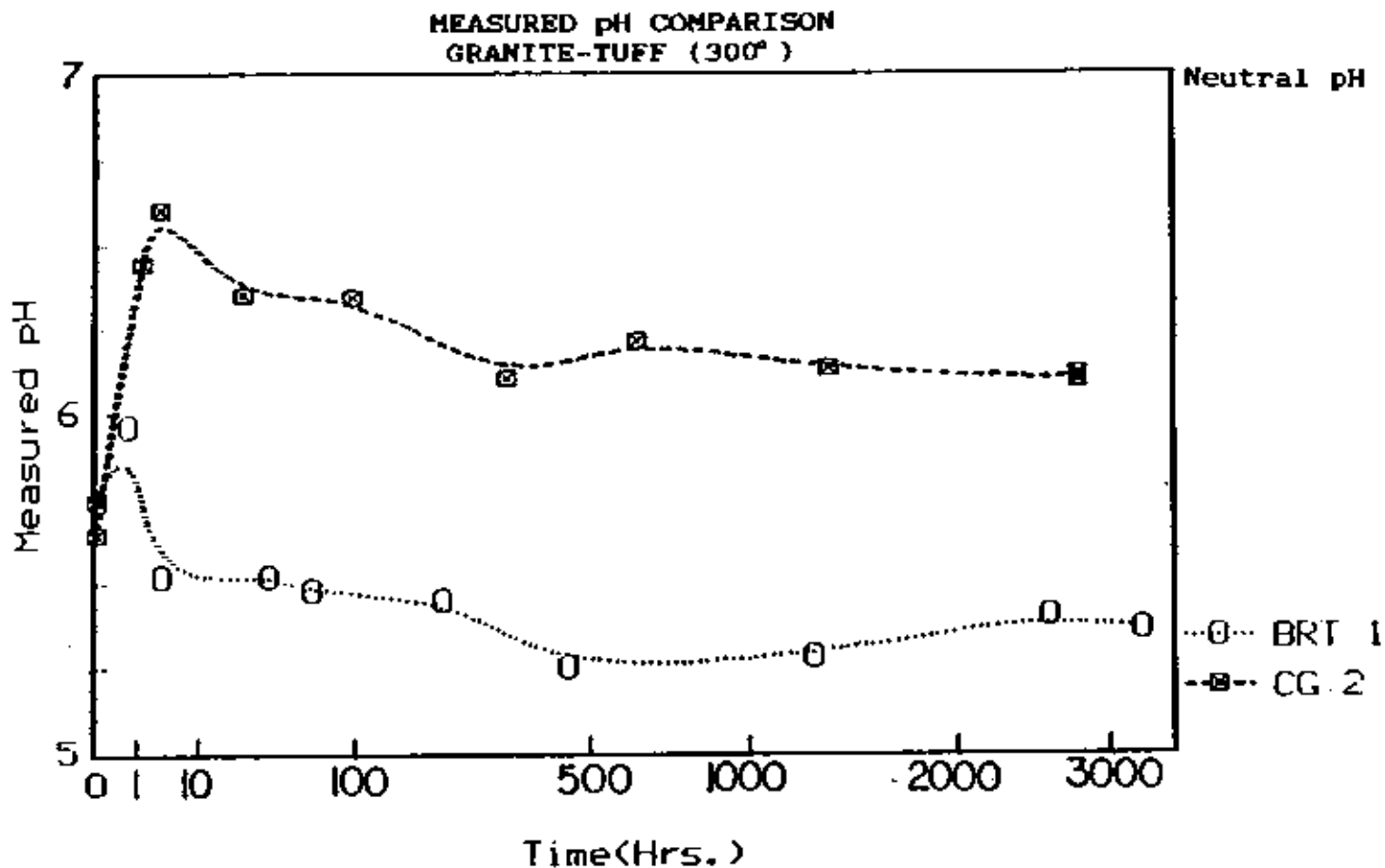


Figure 58: Diagram showing measured pH vs. time trends for the Granite (CG:2) and Tuff (BRT:1) experiment.

Measured granite solution pH values then gradually decreased to 6.10 by the 313 hour sample. Throughout the rest of experiment CG:2, the measured pH values remained relatively constant ranging from 6.09 to 6.21.

Tuff measured pH values rose to 5.96 thirty minutes into experiment BRT:1. Within the first 3.3 hours of the tuff experiment, the measured pH decreased to 5.52, and remained relatively constant throughout the rest of the experiment (5.25 to 5.48). The measured tuff pH values extrapolated from identical time intervals (more than 5 hours after the start of the experiments) are approximately 0.7 to 1.1 pH units more acidic in the tuff experiment. The stable average measured pH for the granite solution (CG 2.5-2.8) was 6.13. The tuff solution (BRT 1.6-1.10) stable measured pH was 5.35. Temple basalt stable measured pH values range from 6.9 to 9.3.

Room-temperature pH values result in the trend from acid to less acid of: tuff < granite < neutral < basalt, with neutral at 25°C and 1 bar being 7.0.

FIGURE 59: GRANITE AND TUFF CALCULATED pH
TREND COMPARISON

Figure 59 shows calculated high-temperature pH values for the tuff (BRT:1) and granite (CG:2) experiment. Calculated pH values are basic throughout the course of the granite experiment. Solution pH rose sharply from 5.6 to 7.2 by the 1.36 sample of experiment CG:2 (CG 2.1). After this initial increase, solution pH slowly decreased reaching 6.7, by the 2762 hour sample. During the initial period of the tuff experiment, the solution became more acidic reaching a minimum pH value of 4.6, by the 3.3 hour interval. After this initial decrease, the calculated pH rose up to a more basic pH of 6.5 by the 36 hour sample. After the 36 hour sample no appreciable upward or downward calculated pH trend is obvious. Calculated pH values after the 36 hour sample ranged from 6.5 to 6.8 (BRT 1.4-1.10).

Initial calculated pH values in the two experiments are approximately equal. Aliquot calculated pH values extrapolated from identical time intervals are more basic throughout the course of the granite experiment. Values extrapolated from identical time intervals during the initial 10

CALCULATED pH COMPARISON
GRANITE - TUFF (300°C)

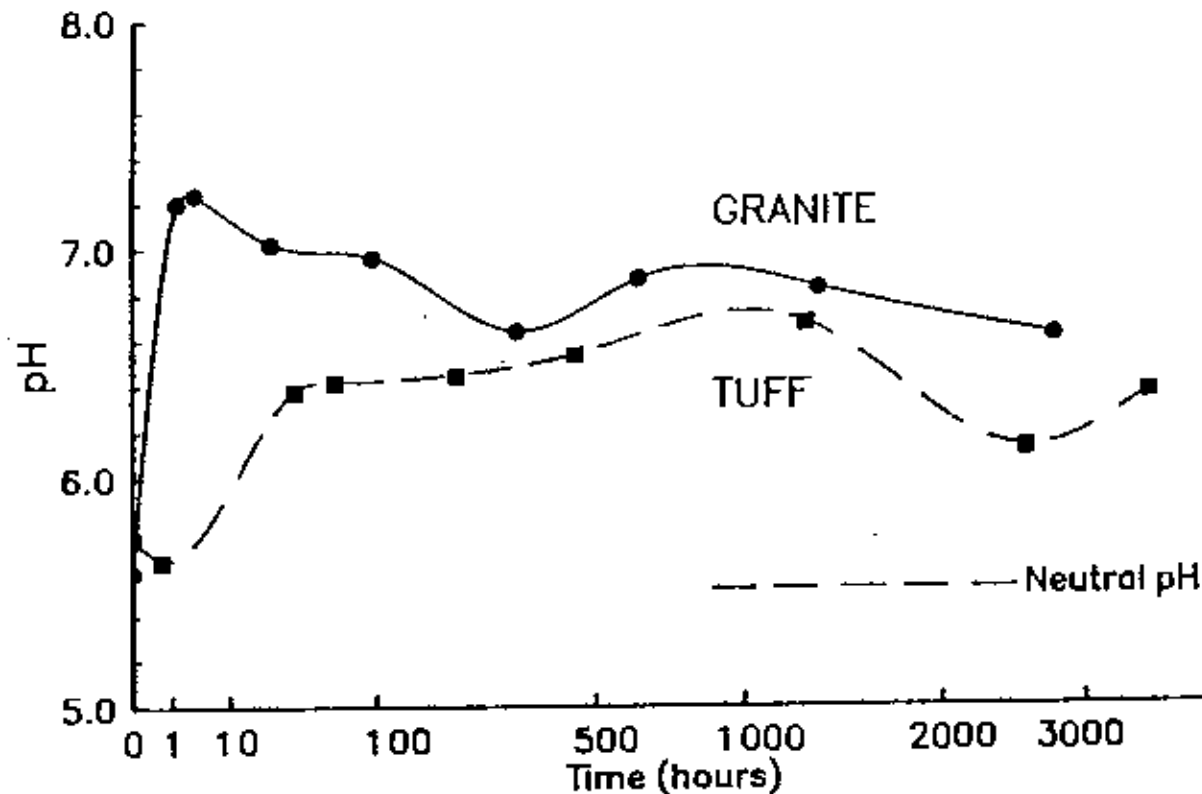


Figure 59: Diagram showing calculated pH vs. time trends for the Granite (CO:2) and Tuff (BRT:1) experiment.

hours of the tuff and granite experiment, indicate a maximum calculated pH divergence of 3 orders. Since the rhyolitic glass in the tuff is more soluble than the quartz and feldspar in the granite (CG 2.4-2.8 avg.=694 mg/l), SiO₂ concentrations are higher throughout the tuff experiment (ERT 1.5-1.10 avg.=1789 mg/l). During the first 3.3 hours of the tuff experiment the initial sharp drop in pH coincides with a sharp rise in SiO₂ concentrations. These results suggests that the formation and disassociation of silicic acid are responsible for the initial decreasing tuff pH trend:



Tuff calculated pH values remain relatively constant after the 36 hour sample, suggesting that illite:smeectite ion exchange started controlling solution pH early in the experiment. After the 0 to 10 hour interval, the decreasing granite pH trend suggests eventual convergence with stable tuff pH values (ERT 1.3-1.10 avg.= 6.54). The convergence of tuff and granite calculated pH trends and the identification of illite and smectites in both experiments (see Secondary Mineral Analyses section), suggest that ion exchange between illite and smectites may control

solution pH. The effect of secondary smectite chemical composition on Granite (CG:2), Tuff (BRT:1), and 300°C Temple basalt experiment stable solution pH will be further evaluated in the following subsection.

pH IMPLICATIONS: THE EFFECT OF ROCK TYPE ON
SMECTITE CHEMICAL COMPOSITION

The most abundant secondary alteration product formed in the 300°C Temple basalt experiments is 15Å trioctahedral smectite (saponite). Illite was also identified in lesser quantities. Chemical analyses of smectites using EDS and electron microprobe techniques indicate that the basalt experiment smectites are rich in Mg and Fe, and poorer in Al. The 300°C basalt experiment saponites formed in copious amounts (Kacandes, 1989). These smectites expand to 17Å on glycolation and collapse on heat treatment at 400°C. Scanning electron microscope (SEM) photomicrographs indicate that the secondary saponite formed in these experiments are well crystallized. Some of the altered olivine grains removed from olivine basalt quench solutions reveal rosettes of secondary saponite.

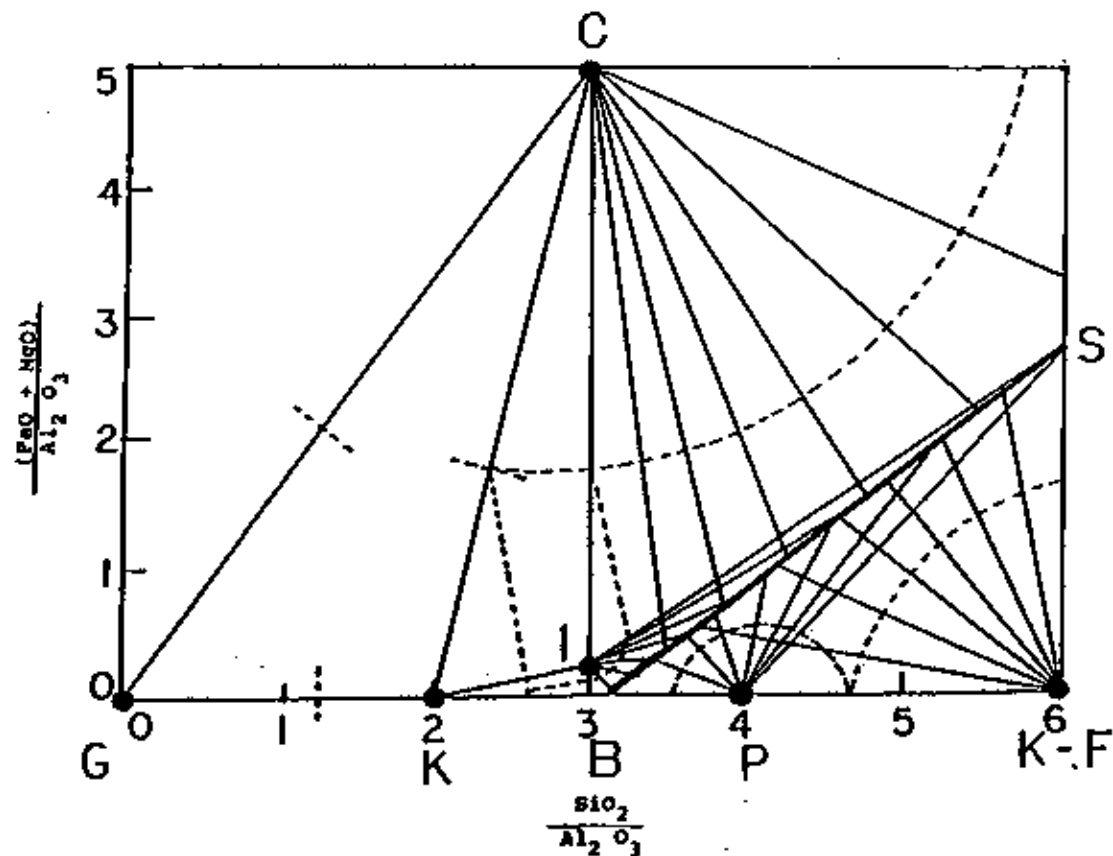
The primary secondary minerals formed in our high SiO_2 -rock:water experiments (CG:1, CG:2, BRT:1), include illite and smectites. Scanning electron microscope (SEM) photomicrographs of secondary smectites removed from granite quench and tuff aliquot solutions were examined. These photomicrographs clearly show the fine-grained poorly crystallized nature of the secondary smectite formed in experiments CG:1, CG:2 and BRT:1 (see Secondary Mineral Analyses section). Visual inspection of tuff and granite smectites using SEM, revealed none of the familiar saponite rosettes precipitated during basalt:water experiments. Analyses of EDS spectra data indicate that granite and tuff solution smectites are richer in Al and contain lesser amounts of Fe, Mg, than 300°C basalt solution smectites. In the smectite solid solution between beidellite and saponite, the beidellites are the Fe-Mg-poor, Al-rich endmember. High Al and low Fe-Mg content suggest that the smectites formed in our high- SiO_2 rock:water experiments lie closer to the beidellite end-member composition.

Since reliable clay free energy data are not available at this time, $\text{SiO}_2/\text{Al}_2\text{O}_3$ (x-axis) and $(\text{FeO} + \text{MgO})/\text{Al}_2\text{O}_3$ (y-axis) ratios of selected clay minerals and K-feldspar, were used to construct

qualitative phase boundaries (Figure 60). A third z-axis representing K_2O/Al_2O_3 mineral ratios (perpendicular to the plane represented by the x and y axes) would position K-bearing minerals (i.e. K-feldspar, Illite) above the plain of this graph. Thus, the tie lines shown in Figure 60 represent points projected from 3-d to 2-d space. Therefore some Figure 60 tie lines appear to intersect in 2-d space. However, these tie lines do not intersect in 3-d space. Not all of the possible phase relationships are shown (e.g. K-spar-Chlorite, K-spar-Kaolinite; muscovite is not included) for reasons of clarity.

Perpendicular lines drawn through Figure 60 tie lines, were used to construct the Figure 61 $\log (Fe^{2+} + Mg^{2+})/(H)^2$ vs. $\log H_4SiO_4$ qualitative topologic mineral stability diagram. In Figure 61, the following mineral stability fields are included; chlorite, gibbsite, kaolinite, illite, K-feldspar, pyrophyllite, and the beidellite-saponite solid solution. The Figure 61 mineral stability fields are used to analyse the relationship between smectite composition and solution pH.

In hydrothermal solutions secondary mineral formation controls solution parameters (such as Fe^{2+} and Mg^{2+}). Saponites are Fe-Mg-rich and beidellites



G=Gibbsite K=Kaolinite C=Chlorite I= Illite
 B=Beidellite P=Pyrophyllite S=Saponite K-F-K-Feldspar

Figure 60: Schematic diagram containing the $(\text{FeO}+\text{MgO})/\text{Al}_2\text{O}_3$ vs. $\text{SiO}_2/\text{Al}_2\text{O}_3$ plot, used to construct the $\log (\text{Fe}^{2+} + \text{Mg}^{2+})/(\text{H}^+)^2$ vs. $\log \text{H}_2\text{SiO}_4$ topologic mineral stability diagram in Figure 61. This diagram is projected from 3-d space (with $\text{Fe}_2\text{O}_3/\text{Al}_2\text{O}_3$ as the z-axis). Although tie lines in this diagram cross, they do not cross in 3-d space. Not all possible phase relationships are shown (e.g., Kspar-Chlorite, Kspar-Kaolinite; Muscovite not included) for reasons of clarity.

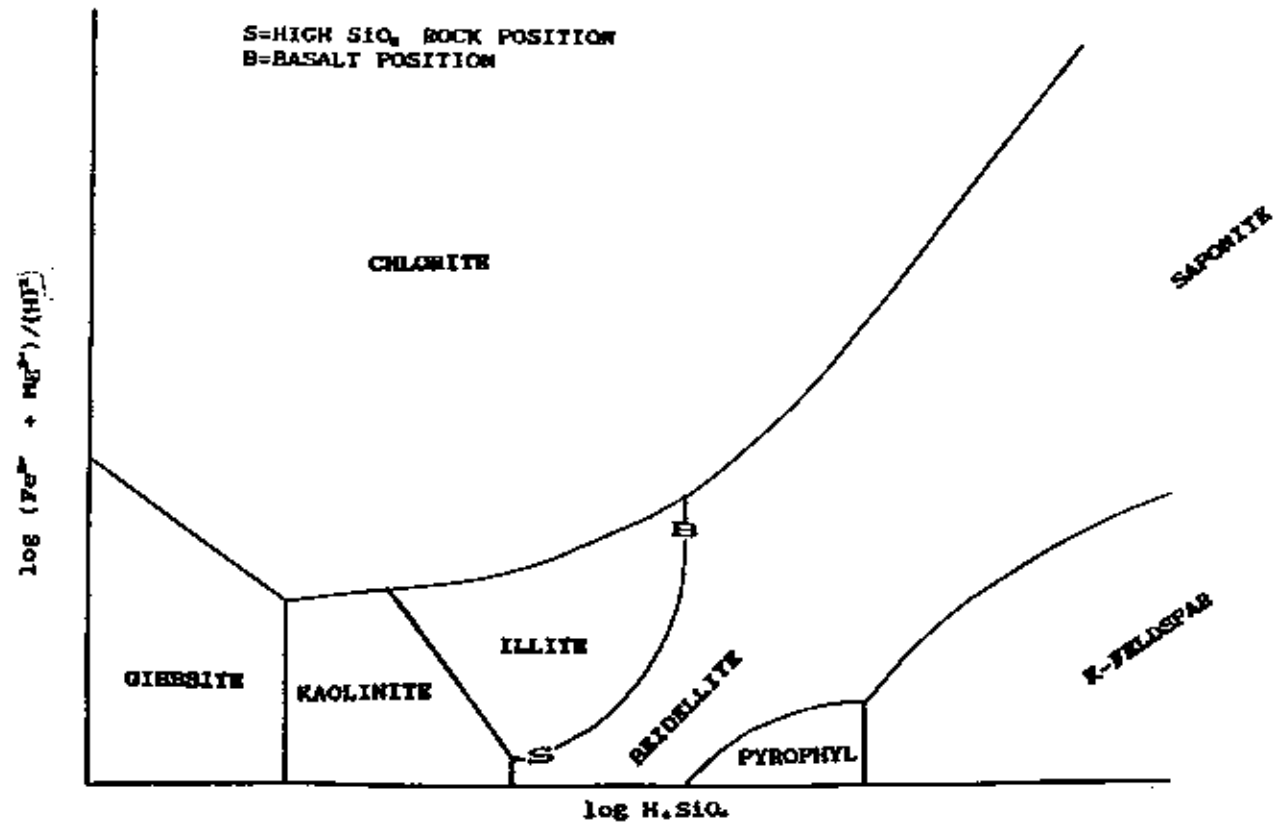


Figure 61: A $\log (\text{Fe}^{2+} + \text{Mg}^{2+})/(\text{H}^+)^2$ vs. $\log \text{H}_4\text{SiO}_4$ topologic mineral stability diagram used to analyze the effect of smectite composition on solution pH.

are Fe-Mg poor. More Fe+Mg should be released into solution by iron-magnesium-rich-basaltic rocks. The average (MgO+FeO) weight percentage value based on the analyses of 3621 basalt samples is 13.66% (LeMaitre, 1976). The (FeO+MgO) values for the Conway Granite and Bannock Rhyolite Tuff are 2.48%, and 0.68% respectively. In the Temple basalt experiments Fe^{2+} is released into solution by the dissolution of mesostasis. Dissolution of strained glass around Ca-Fe-P microspherules, and the Fe-Ca-P microspherules themselves appear to be primarily responsible for the removal of O_2 from basalt experiment solutions (see Redox Comparisons section). Ferromagnesium minerals (e.g., olivine) are also fairly soluble. This supposition is supported by SEM photomicrographs of heavily altered ferromagnesium minerals removed from 300°C basalt:water experiments (Kacandes, 1989). Therefore it can be assumed that dissolution of basalt Ca-Fe-P microspherules, glass, and any ferromagnesium minerals would release high amounts of Fe and Mg into solution. In the 300°C Temple basalt experiments Fe^{2+} and Mg^{2+} were rapidly incorporated into precipitating saponite structures.

In our high-SiO₂ rock:water experiments (CG:1, CG:2, BRT:1), initial dissolution of primary minerals and/or glass released little Fe and Mg into solution. Therefore Al-rich beidellitic smectites precipitated from the CG:1, CG:2, and BRT:1 autoclave solutions. The similarity between tuff and granite stable solution pH suggests that H⁺ activity in these experiments was controlled by the equilibrium between beidellite and illite. Assuming equilibrium between illite and smectite in these experiments (CG:2, BRT:1, 300°C basalt experiments) symbols are plotted on Figure 60 to represent relative positions based on smectite identification data. The "S" symbol represents the secondary beidellites formed in our high-SiO₂ rock:water experiments (CG:1, CG:2, and BRT:1). The "B" symbol represents the secondary saponite formed in the 300°C Temple basalt:water experiments. Experiment CG:2 and BRT:1 solution log (Fe+Mg)/(H)² ratios are apparently controlled by the equilibrium between beidellite and illite. Basalt log (Fe+Mg)/(H)² ratios are likely controlled by the equilibrium between saponite and illite. The Fe and Mg solution concentrations in these experiments are similar. Thus these results suggest that solution pH in BRT:1, CG:2, and the Temple basalt

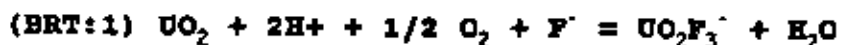
experiments are controlled by smectite precipitation. The type of smectite formed in these solutions appears to be determined by the amount of (FeO+MgO) contained within a rock sample. Therefore the stable solution pH which develops is determined by the amount of (FeO + MgO) contained within a rock. In summary: these comparisons suggest that smectite precipitating solutions reacting with Fe-Mg-rich mafic rocks (i.e. basalt) would be more basic, than smectite precipitating solutions interacting with high-SiO₂ igneous rocks (i.e. granite and rhyolite tuff).

POSSIBLE EFFECTS OF SOLUTION pH ON WASTE
CONTAINER CORROSION AND SPENT FUEL ROD
SOLUBILITY

The stable 300°C pH values calculated in these high-SiO₂ rock:water experiments (approx. pH= 6.5) are 1.0 to 1.5 units more acidic than 300°C basalt:water values (approx. pH= 7.5 to 8.0). Lower pH solutions percolating through a high-level nuclear waste repository site would result in higher rates of container corrosion. If calculated solution pH values are similarly effected by rock

(FeO+MgO) content in repository solutions, then it can be assumed that the rate of container corrosion at a basalt site would be slowest (compared to granite or tuff).

The solubility of UO_2 for spent fuel rods exposed to percolating repository groundwater can also be effected by solution hydrogen ion concentration. For example in the redox comparison section we determined that $U(OH)_5^-$ and $UO_2F_3^-$ would be the stable uranium complexes in equilibrium with the granite, and tuff solutions, respectively. Using equations from the Redox Comparisons section:



it is clear that a decrease in tuff solution pH would result in an increase in UO_2 solubility, and a increase in granite solution pH would yield a similar result.

The combination of lower tuff solution pH, tuff glass redox buffering capacity, tuff glass redox potential, and higher tuff solution F concentrations (see Solution Parameter Trends vs. Time section), may result in comparatively higher rates of waste container corrosion and greater solubility of UO_2 for spent fuel rods at a tuff repository site (i.e., Yucca Mountain, Nevada).

Thus it may be informative to conduct Rhyolite Tuff glass dissolution experiments at lower temperatures. These experiments should be analyzed to determine what effect pH, redox variation, and F concentrations may have on container corrosion and U-complex release rates at the Yucca Mountain repository.

CATION/PROTON COMPARISONS BETWEEN CG:2, BRT:1, 300°C
TEMPLE BASALT EXPERIMENTS AND ICELANDIC GEOTHERMAL
FLUIDS

Figures 62-64 compare selected stable cation/proton ratios calculated from; 270-325°C Icelandic geothermal fluids 300°C Temple basalt:water experiments, and our high-SiO₂ rock:water experiments (CG:2, BRT:1).

Figure 62 was used to compare $\log Ca/(H)^2$ vs. $\log Na/H$ values. Figure 63 is a $\log Na/H$ vs. $\log K/H$ plot. Figure 64 is used to compare $\log Mg/(H)^2$ vs. $\log Ca/(H)^2$ values. The symbols representing CG:2, BRT:1, Temple basalt experiments, and Icelandic geothermal fields are included in Figures 62-64. Experiment BRT:1 and CG:2 stable cation/proton ratios are represented by the last four solution aliquots removed from each experiment (calculated activity and activity ratios for experiment CG:2 and BRT:1 are tabulated in Appendix 1a and 1b, respectively).

The stable cation/proton ratios calculated from Icelandic geothermal fields and 300°C Temple basalt experiments, were obtained from diagrams plotted to compare the chemical interactions of water/rock experiments vs. those of active

geothermal systems (Kacandes et al., 1988). The 270-325°C range was used for the Icelandic data due to the paucity of geothermal data available precisely at 300°C. The Icelandic data was primarily obtained from basaltic geothermal solutions (although Icelandic rhyolite geothermal solution data is also included).

The effect of rock type on long-term geothermal solution parameters is considered to be negligible (Arnorsson and Gunnlaugsson, 1983; Kacandes, 1989). Thus the data point scatter from rhyolite, granite, tuff, basalt, sediment, and andesite geothermal solutions can be approximated by the Icelandic data point scatter. Therefore a comparison of BRT:1, CG:2, and Temple basalt experimental data vs. Icelandic geothermal field data, can be used to evaluate differences and similarities between the solutions formed in these experiments and natural geothermal fluids.

DATA PRESENTATION (FIGURE 62): Higher tuff experiment $\text{Ca}/(\text{H})^2$ ratios (and slightly higher Na/H ratios) result in a small offset between CG:2 and BRT:1 data points. The offset between the high- SiO_2 rock:water experiments (CG:2 and BRT:1) and the basalt experiments, is due to higher calculated

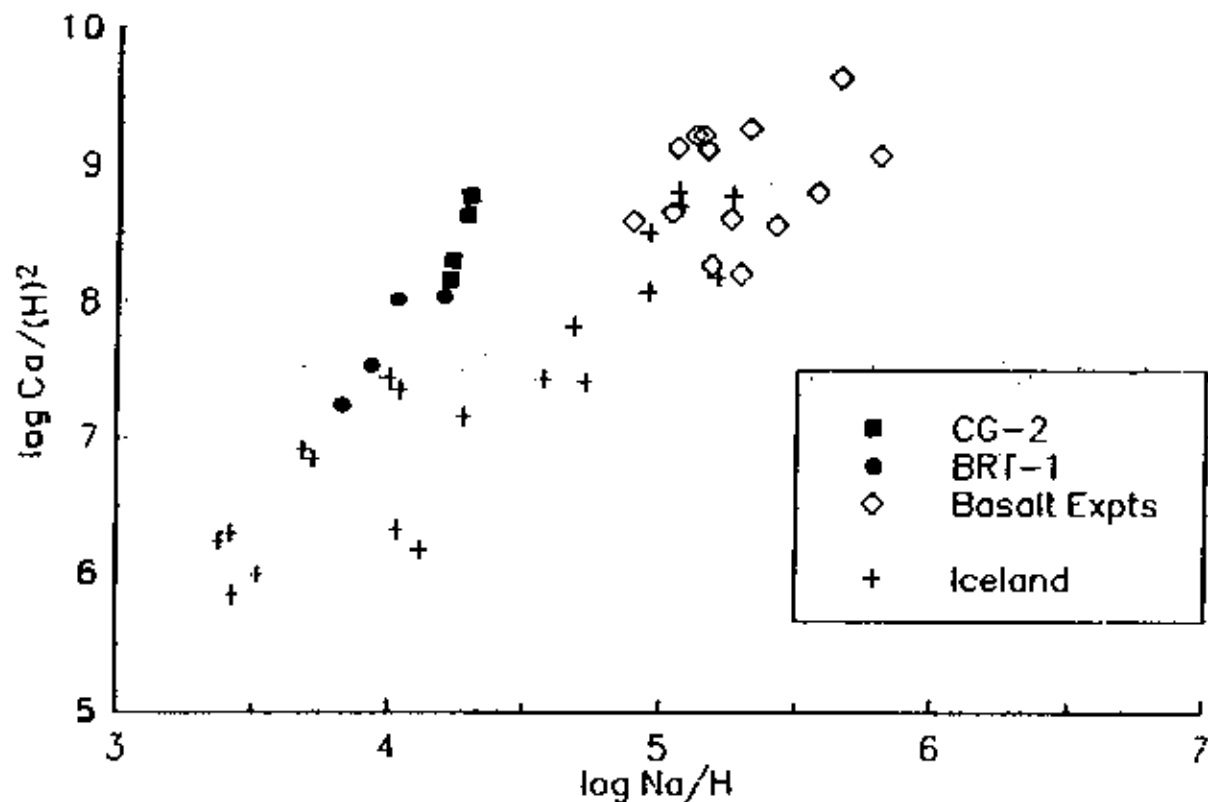


Figure 62: Diagram used to compare long-term stable $\log Ca/(H)^2$ - $\log Na/H$ values from CG-2, BRT-1, 300°C Temple basalt experiments, and Icelandic geothermal fields.

basalt:water experiment $\text{Ca}/(\text{H})^2$ and Na/H values. High- SiO_2 rock:water (CG:2 and BRT:1) and basalt:water experimental points fall predominantly outside the scatter of Icelandic geothermal solution data. The CG:2 data points fall closest to the center of geothermal fluid scatter, followed by the basalt and tuff (BRT:1) data points, respectively.

DATA INTERPRETATION (FIGURE 62): Experiment CG:2 and BRT:1 Na concentration trends are similar. Therefore the slight offset between the granite and tuff data points is primarily due to differences in pH (the stable tuff solution pH is slightly more acidic). Lower tuff $\text{Ca}/(\text{H})^2$ values also result from decreasing Ca concentration vs. time trends (see Solution Parameter Trends vs. Time section).

Average basalt experiment pH values (approx. range= 7.5 to 8.0) are 1.0 to 1.5 units higher than the values calculated in our high- SiO_2 rock experiments (approx.= 6.5). The higher stable basalt pH values result in higher calculated $\log \text{Ca}/(\text{H})^2$ and $\log \text{Na}/\text{H}$ values. Differences in the concentration of Ca and Na in the granite, tuff, and basalt experiment solutions are not significant enough to account for the offset between basalt and

high-SiO₂ rock experiment data points. Therefore the offset between our acidic rock experiments and the scatter representing 300°C basalt experiments, is primarily a result of the more acidic solutions formed in experiments CG:2 and BRT:1.

The calculated Ca/(H)² values from experiment CG:2 and BRT:1 are higher than geothermal field values. This difference accounts for the offset between the high-SiO₂ rock:water experiment (CG:2 and BRT:1) and geothermal fluid data points. Stable high-temperature calculated pH values (approx.= 6.5) from CG:2, BRT:1, and 270-325°C geothermal solutions are similar. Therefore, the offset between the high-SiO₂ rock:water experiment and geothermal fluid data points is due to differences in the amount of Ca in these solutions. In open systems, like the Icelandic magmatically-driven geothermal fields, CO₂ is removed from solution by the precipitation of secondary calcite. Experiment CG:2 quench solution and log IAP/K data suggest that secondary onlcite may have formed in this experiment (see Secondary Mineral Analyses section). However, calcite was not present in sufficient amounts to be identified by EDS/SEM and XRD techniques in both experiments. Therefore the higher Ca/(H)² values recorded in experiments CG:2

and BRT:1 (as opposed to Icelandic geothermal solutions) may primarily result from lack of CO₂ gas input in our closed-system experiments. The CG:2 Ca/(H)² and Na/H values seem to best approximate geothermal fluid values, followed by the basalt experiments and BRT:1, respectively.

DATA PRESENTATION (Figure 63): Lower granite experiment K/H ratios result in a small offset between CG:2 and BRT:1 data points.

The offset between the high-SiO₂ rock:water experiments (CG:2 and BRT:1) and the basalt:water experiments, is due to higher calculated basalt:water experiment Na/H values.

High-SiO₂ rock:water and basalt:water experimental points fall predominantly outside the scatter of Icelandic geothermal solution data. In Figure 63 experiment CG:2 data points fall closest to the center of geothermal fluid scatter, followed by the basalt and tuff (BRT:1) data points, respectively.

DATA INTERPRETATION (FIGURE 63): The general offset between tuff and granite scatter results from the higher log K/H values calculated from BRT:1 solution data. Experiment CG:2 K/H values are

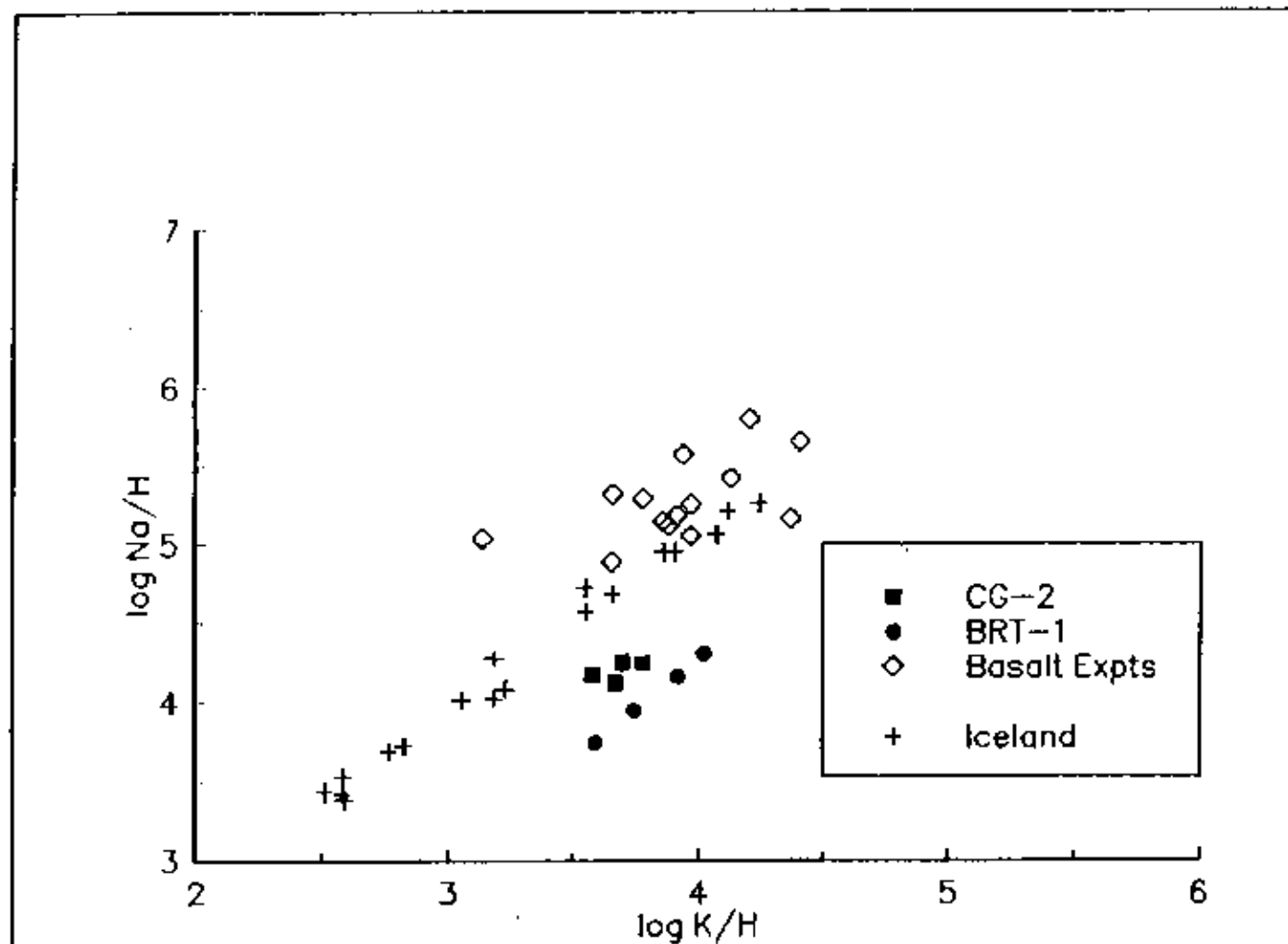


Figure 63: Diagram used to compare long-term stable $\log \text{Na}/\text{H}$ - $\log \text{K}/\text{H}$ values from CG-2, BRT-1, 300°C Temple basalt experiments, and Icelandic geothermal fields.

lower due to the comparatively lower concentration of K in the granite solution (compared to BRT:1). Lower stable tuff solution pH values partially counter the effect of higher BRT:1 K concentrations on K/H values.

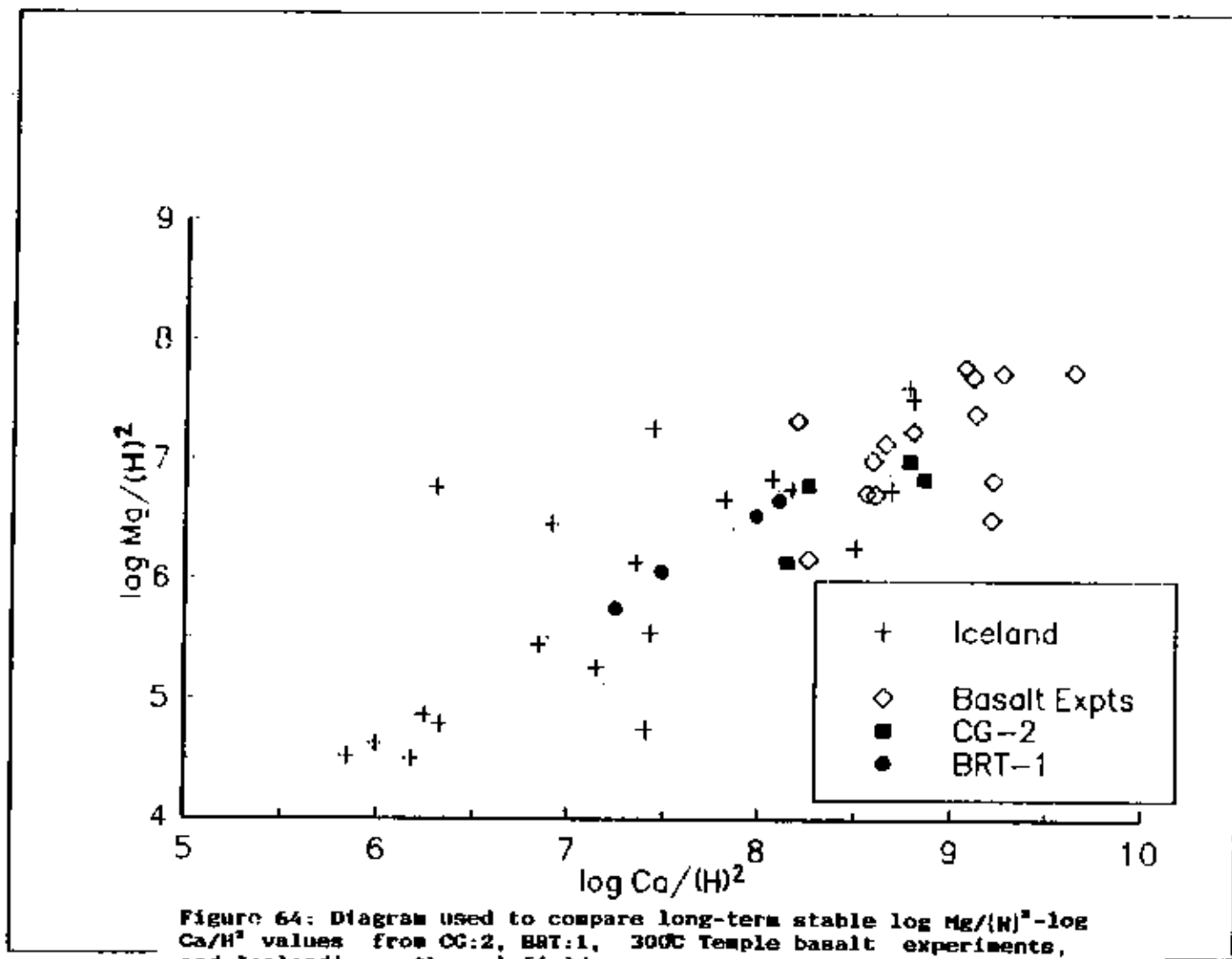
The discrepancy between the basalt:water and high-SiO₂ rock:water scatter (CG:2, BRT:1) is due to the higher Na/H ratios calculated in the basalt experiment. The Na/H ratios calculated from our high-SiO₂ rock:water experiments (CG:2 and BRT:1) are lower due to comparatively basic basalt:water experiment stable pH values.

The offset between short-term autoclave experiments and long-term geothermal solution data in Figure 63 can best be explained by referring to the Na-K solution geothermometer results included in this study (see Tuff and Granite Geothermometer Evaluation section). This solution geothermometer is based on the equilibrium between albite and microcline. In natural geothermal fields the Na-K geothermometer has been proven useful in the estimation of geothermal solution temperatures. However calculated Na-K geothermometer values were not accurate in determining the actual solution temperature in the granite (CG:2), tuff (BRT:1), and basalt experiments (Gardiner, 1988). These

results suggest that the time intervals selected for these short-term experiments are not long enough to reproduce geothermal fluid Na/K ratio values. Experiment CG:2 data points may fall closer to the geothermal fluid data point scatter due to the formation of secondary high albite in this experiment (a common secondary mineral found in geothermal fields).

DATA PRESENTATION (Figure 64): This plot shows that the tuff and basalt data points overlap with each other, and with the high $Mg/(H)^2$, high $Ca/(H)^2$ edge of the geothermal fluid scatter. The granite data points plot well within the geothermal fluid point scatter.

DATA INTERPRETATION: These data suggest that the secondary mineral:solution reactions controlling Ca and Mg concentrations in these short-term experiments are similar to those of geothermal fluids. The concentration of Ca and Mg in 300°C tuff, granite, basalt experiment solutions, and high-temperature geothermal fluids are thought to be primarily controlled by secondary clay mineral formation. These results suggest that the formation of illites and smectites in the above



mentioned experiments and geothermal fluids, results in little offset between these data points. Granite experiment data points fall closest to the center of geothermal fluid scatter suggesting that the reactions controlling Ca and Mg concentrations in this experiment are similar to geothermal fluids.

DATA SIMILARITIES (FIGURES 62-64): In each of the figures granite points fall closest to the center of Icelandic geothermal fluid scatter followed by basalt, and 95% glass rhyolite tuff, respectively. These figures illustrate that long-term solution chemistry of geothermal fluids is best predicted by experiment CG:2, followed by the basalt and tuff (BRT:1) rock:water autoclave experiments, respectively. Tuff (BRT:1), Granite (CG:2), and 300°C basalt experiment calculated solution geothermometer trends will be analyzed in the following section (see Tuff and Granite Geothermometer Evaluation section) to gain further insight with respect to the differences and similarities between short-term autoclave solutions and geothermal fluids.

GEOOTHERMOMETER EVALUATION

Quartz (Fournier and Potter, 1962), Na-K (White, 1965), and Ca-Na-K (Fournier and Truesdell, 1973), solution geothermometers have been used in a number of studies to determine the temperature of geothermal solutions (e.g., Fournier, 1981; Arnorsson, 1983; Truesdell, 1973). The correspondence of these geothermometers with the BRT:1 and CG:2 solution temperature (300°C) is evaluated to determine the extent to which these short-term experiments reproduce the long-term chemistry of 300°C geothermal solutions.

The quartz geothermometer is based upon the variation in solubility of quartz as a function of temperature. The Na/K geothermometer was postulated (White, 1965) as being accurate in natural waters above 175-200°C, where Na and K concentrations are controlled by the equilibrium with albite and K-feldspar. Certain geothermal fields containing solutions rich in Ca, such as Mammoth Hot Springs in Yellowstone Park and the Salton Sea geothermal brines did not yield reasonable Na/K temperatures. As a result the Ca-Na-K geothermometer was introduced to empirically consider Ca concentrations present in geothermal

solutions (Fournier and Truesdall, 1973). Equations and graphs were constructed from connate brine Mg concentration data (1 ppm to 3920 ppm) to correct for the adverse effects of Mg on the Ca-Na-K geothermometer (Fournier and Potter, 1979). The Mg correction to the Ca-Na-K geothermometer was not applied due to low Mg concentrations in both experiments. The results of the geothermometer calculations for experiment CG:2 and BRT:1 are listed in Table 9. Apparent solution temperature vs. time diagrams were produced for the tuff (Figure 65) and granite (Figure 66) experiments.

TUFF GEOTHERMOMETER VALUES (FIGURE 65)

Quartz geothermometer apparent temperature values are higher than the actual temperature (BRT 1.4-1.10 average = 611°C). These values indicate that the tuff solution was saturated with respect to secondary amorphous silica (not quartz). The quartz geothermometer has worked well in geothermal solutions with temperatures greater than 150°C. These results indicate that geothermal fluids are saturated with respect to secondary quartz. As a solution becomes saturated with respect to

1.4-1.9		2.4-2.8 avr.	
Allyquif	CG 2.0	CG-Na-K	CG 2.0
BRT 1.0	CG 2.1	N/A	CG 2.1
BRT 1.1	CG 2.2	N/A	CG 2.2
BRT 1.2	CG 2.3	417.9	CG 2.3
BRT 1.3	CG 2.4	390.7	CG 2.4
BRT 1.4	CG 2.5	382.9	CG 2.5
BRT 1.5	CG 2.6	404.6	CG 2.6
BRT 1.6	CG 2.7	389.0	CG 2.7
BRT 1.7	CG 2.8	404.6	CG 2.8
BRT 1.8		424.0	
BRT 1.10		415.2	
		424.0	
		405.6	
		CG-Na-K	
		N/A	
		298.5	
		CG-Na-K	
		N/A	
		424.8	
		Na-K	
		N/A	
		290.0	
		Quartz	
		312.2	
		610.9	

TABLE 9 : Geothermometer values

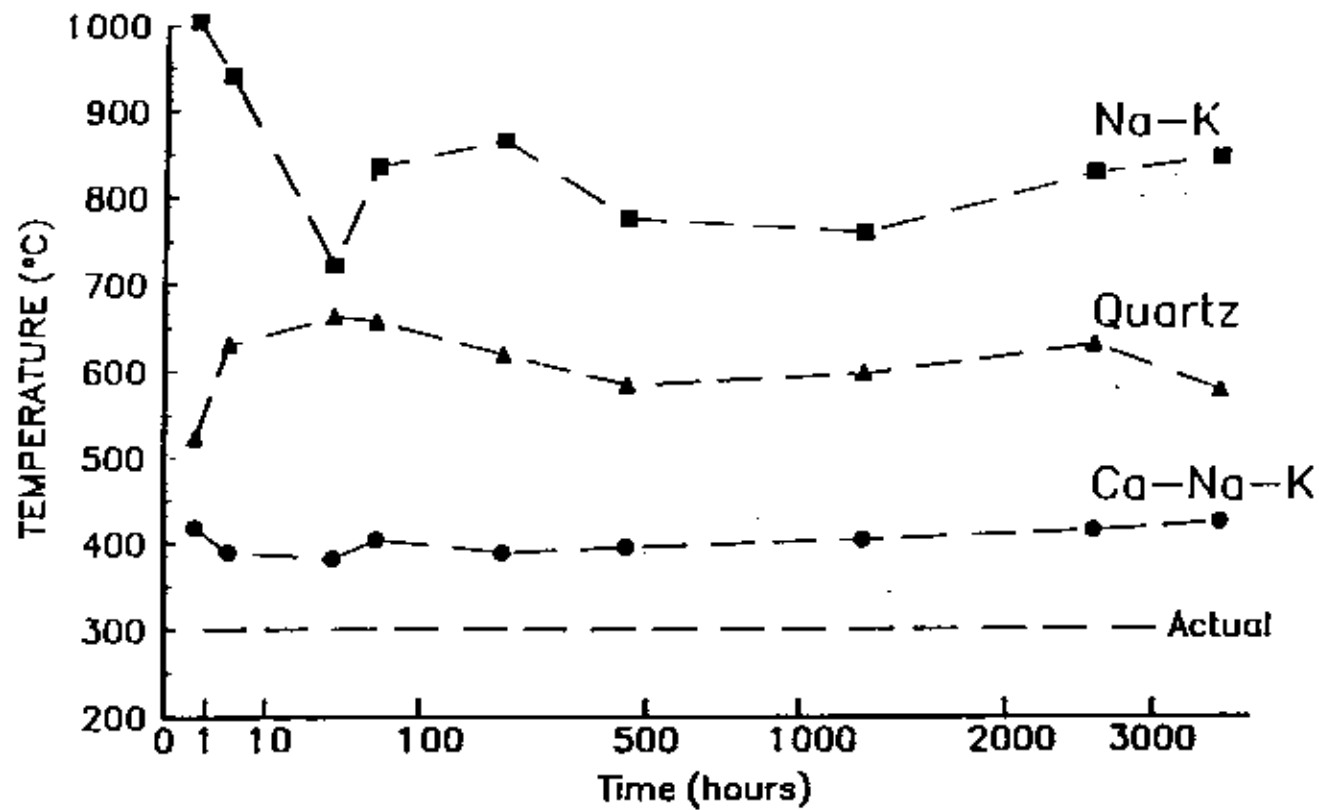


Figure 65: Tuff experiment (BRT:1): Ca-Na-K, Na-K, and Quartz solution geothermometer trends.

rhyolitic glass, the rate of SiO_2 incorporation into secondary minerals will exceed the rate of SiO_2 release from glass dissolution. Thus, as the time of reaction between glass-rich tuff and solution groundwater increases, SiO_2 concentrations may decrease. Therefore if geothermal solutions react with rhyolite glass-rich rocks for extended periods of time, then the quartz geothermometer should fall closer to actual temperatures.

The BRT:1 Na-K geothermometer apparent temperatures were approximately 2.5 to 3.3 times higher than the actual 300°C value (ranging from 759° to 1006°C). Stable Na/K geothermometer apparent temperatures in the tuff experiment (818°C) are approximately twice as high as those calculated in the granite experiment. This difference is due to the comparatively high concentration of K contained in the BRT:1 solution (compared to geothermal fluids).

Stable Ca-Na-K geothermometer apparent temperatures are also high (BRT 1.4-1.10 stable average = 406°C). The difference between Ca-Na-K geothermometer apparent temperature values and the actual experimental temperature, are also due to the comparatively high concentration of K contained in the BRT:1 solution.

None of the solution geothermometers were accurate in predicting experimental temperature in the tuff experiment (see Figure 65). All three solution geothermometers provided apparent temperatures above the range of measured experimental and geothermal values. These results suggest that the chemistry of the aliquots removed from experiment BRT:1 do not correspond with geothermal fluids.

GRANITE GEOTHERMOMETER VALUES (FIGURE 66)

After the 3.2 hour sample the quartz geothermometer accurately predicted experimental temperature. The quartz geothermometer stable estimated temperature average of 312°C was within 4% of the correct 300°C value. The quartz geothermometer was relatively accurate throughout the remainder of the granite experiment as silica concentrations appeared to be controlled by equilibrium with secondary quartz (CG 2.3-2.6 log IAP/K values ranged from 0.05 to -0.02).

Stable Na-K geothermometer values did not accurately predict the CG:2 experimental temperature (CG 2.3-2.6 =425°C). The Na-K

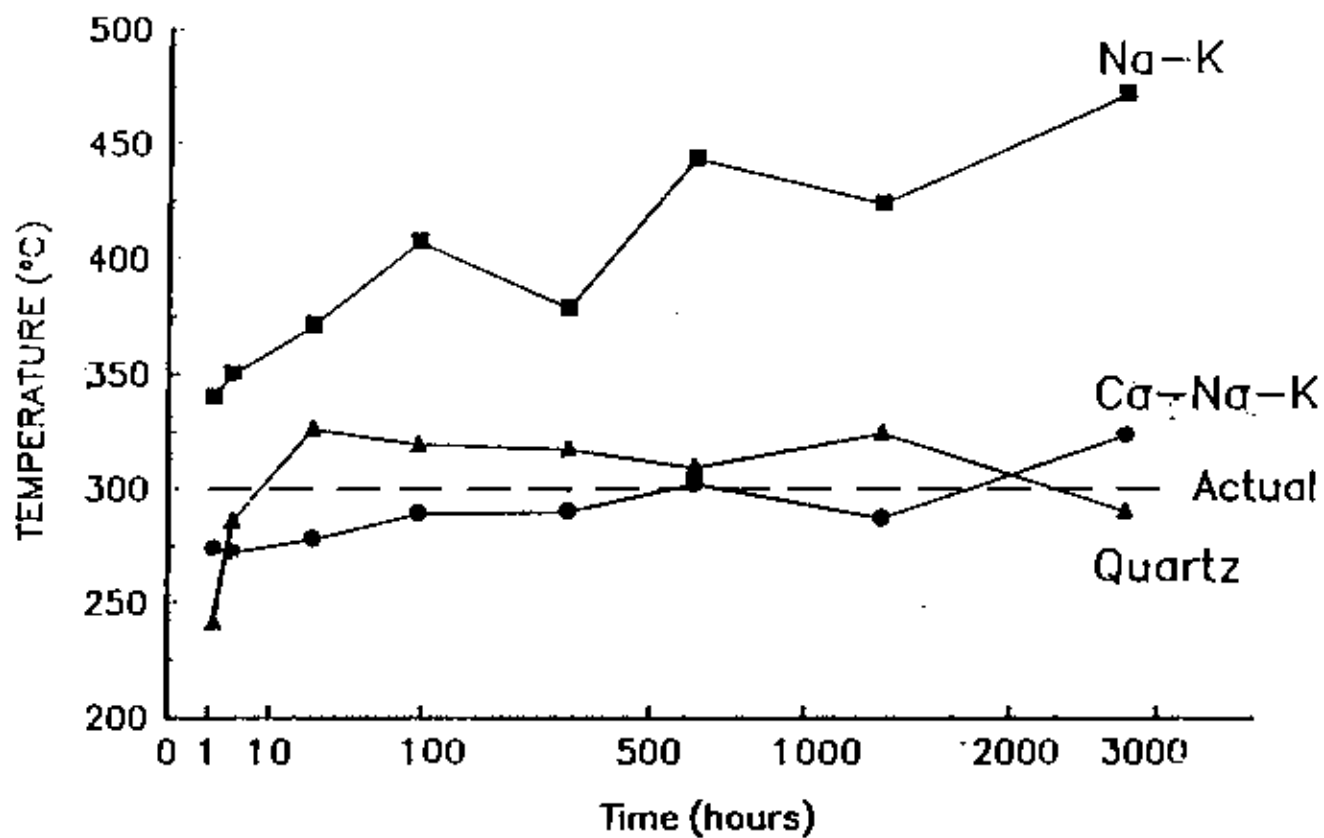


Figure 66: Granite experiment (CG:2): Ca-Na-K, Na-K, and Quartz solution geothermometer trends.

geothermometer results suggest that the time interval selected for experiment CG:2, is not adequate for the equilibrium between albite and microcline to occur. These results are not surprising since the Na/K geothermometer is often very sluggish to respond even in geothermal systems where solutions have had long time intervals to equilibrate (Henley et al., 1984). In the granite experiment (CG:2) the Ca-Na-K geothermometer started predicting experimental solution temperatures (Figure 66) within 9% of 300°C, by the first 1.36 hour sample. These results suggest that the precipitation of illite and smectites controlled Ca, Na, and K concentrations in experiment CG:2. The stable Ca-Na-K geothermometer average temperature based on aliquots CG 2.4-2.8 is equal to 299°C. The Ca-Na-K geothermometer performed well since it is based on equilibrium with clays present in natural geothermal fields (such as illite and smectites).

IMPLICATIONS FOR THE USE OF SHORT-TERM
AUTOCLAVE EXPERIMENTS IN THE PREDICTION OF
LONG-TERM GEOTHERMAL FLUID CHEMISTRY

The correspondence between CG:2 Ca-Na-K and quartz geothermometer values with the actual solution temperature (100°C), suggests that experiment CG:2 more closely models natural geothermal fluids (as opposed to experiment BRT:1). Apparent solution geothermometer values were calculated from 300°C Temple basalt:water experiment data (Moore, 1983; Korn, 1986; Gardiner 1988). The geothermometer values calculated in these experiments did not correspond as well as CG:2 data, with the actual solution temperature (300°C). However basalt geothermometer values closer approach the actual temperature, when compared with the 95% rhyolitic glass experiment (BRT:1). The basalts used in these experiments contained 10-40% mesostasis (predominantly glass). Solution/glass phase interactions generate a high level of supersaturation with respect to a variety of aluminosilicate minerals. In such supersaturated solutions a sequence of metastable reactions will occur resembling an Ostwald step sequence (Dibble *et al.*, 1981). Eventually, after a series of

steps, stable mineral assemblages will form. However the formation of intermediate metastable minerals may delay this eventuality for millions of years. The formation of minerals commonly found in geothermal fields (i.e. quartz, and high albite), suggest that stable mineral assemblages began to form in experiment CG:2, after only 2761 hours. The experiments compared in this geothermometer comparison seem to approach long-term geothermal solution chemistry in the following order; holocrystalline Conway Granite, 10-40% glass basalt, 95% Bannock Rhyolite Tuff. These results would suggest that the time interval necessary to emulate geothermal solutions in short-term autoclave experiments varies sympathetically with glass content.

Natural geothermal solution data are considered to be useful in predicting the long-term chemistry of high-level nuclear waste repository solutions (Ulmer et al., 1987). These data suggest that the glass content of the rock material within geothermal fields should be considered, when selecting natural analogs to predict the long-term solution chemistry of high-level nuclear waste repository solutions.

SUMMARY**SUMMARY OF EXPERIMENTAL RESULTS**

1) Optical mineralogy, XRF, and FeO titration techniques results suggest that the holocrystalline Conway Granite and 95%-glass Bannock Rhyolite Tuff are chemically similar. Therefore the results from experiments CG:2 and BRT:1 can be utilized to evaluate the effect of rhyolitic glass dissolution on concentration trends, fO_2 , pH, secondary mineral formation, and approach to long-term geothermal fluid chemistry. Granite (CG) and tuff (BRT) oxide weight percentages and norms plot near the center of granite and tuff fields in the LaMaitre diagrams, indicating that these rocks can be used to study rock:water interactions occurring between typical granites and glass-rich rhyolite tuffs at 300°C.

2) The secondary minerals identified from tuff aliquots BRT 1.2-1.10 include; illite (2M₁), smectites, amorphous silica, and anhydrite. The X-ray diffractograms of tuff aliquot secondary mineral assemblages indicate that illite was the predominant secondary mineral to precipitate from

the tuff experiment autoclave solution. The smectites identified from tuff solutions were not homogeneous and contain varying amounts of Fe, Ca, Ti, Na, and Mn.

The secondary minerals identified from granite quench solutions CG:1 and CG:2 include; illite (2M₁), smectites, high albite, and quartz. The XRD data of granite quench secondary mineral assemblages (CG:1, CG:2) indicate that illite was the dominant secondary mineral formed in these experiments. The smectites identified in the granite experiment incorporated varying amounts of Fe and Ca.

Starting rock (FeO + MgO) content and secondary mineral identification data indicate that the smectites identified in the granite and tuff experiments are beidellitic. Phase diagrams were constructed using solution log Na/H vs. log K/H ratio values. These diagrams demonstrate that secondary mineral formation controlled solution parameters in these experiments. Secondary mineral identification analyses indicate that the near-linear distribution of granite and tuff log Na/H vs. log K/H ratio values may represent high albite:illite (CG:2), and smectite:illite (BRT:1) phase boundaries, respectively.

Comparisons between CG:2, BRT:1, and 300°C Temple basalt secondary mineral assemblages indicate that the illite/smectite mass ratio is higher for our high-SiO₂ rock:water experiments (CG:2, BRT:1). These comparisons also indicate that the mass of secondary minerals formed in CG:1 and CG:2 is lower, when compared to the tuff and basalt experiments.

3) The glass within the tuff was more soluble than the feldspars and quartz contained within the granite. Rhyolitic glass dissolution resulted in comparatively higher tuff SiO₂, K, Al, F, Fe, and SO₄ concentrations. Concentrations increased sharply during the first 1 hour of both experiments, and stabilised within the first 10 hours of the tuff and granite experiments. Most CG:1, CG:2, and BRT:1 species concentration aloges were controlled by secondary mineral formation.

4a) Stable log fO₂ values calculated from CG:2 (predicted), 300°C Temple basalt autoclave experiments, and geothermal fluids range from -31 to -33. The BRT:1 stable log fO₂ of -27 is 3-5 orders more oxidising (than granite, basalt, and geothermal solutions).

4b) At solution temperatures ranging from 0° to 350°C the average basalt (LeMaitre, 1976) redox buffering capacity based on FeO (wt.%) is 3 times greater than the Conway Granite, and 16 times greater than the tuff.

5) A comparison of CG:2, BRT:1 and Temple Basalt stable measured (room temperature) pH suggests the following general effect of rock type on the numeric value of cooled solution pH: Glassy Tuff (Granite (Neutral (Basalt (acidic to basic). During initial extrapolated intervals the BRT:1 solution was as much as 3 pH units more acidic than CG:2 solution. The difference between solution pH values extrapolated from identical time intervals decreases due to the gradual decrease in granite pH. The stable granite and tuff calculated pH (approx.= 6.5) is approximately 1 to 1.5 orders more acidic when compared with 300°C Temple basalt experiment values (approx. range= 7.5 to 8.0). The difference in high-SiO₂ rock:water and basalt:water stable pH is due to differences in the composition of smectites formed in these experiments. In the 300°C Temple basalt experiments large amounts of Fe and/or Mg are added to solution by the dissolution of mesostasis (glass and Fe-Ca-P microspherules),

and any ferromagnesium minerals. These elements were rapidly incorporated into secondary saponite structures. Illite has also been identified in lesser quantities in the Temple basalt experiments. Topologic mineral stability diagrams indicate that the equilibrium between saponite and illite would result in comparatively basic basalt solution pH (stable 300°C basalt solution pH values range from 7.5 to 8.0). In contrast, the smectites identified in BRT:1 and CG:2 contain higher amounts of Al and lower amounts of Fe, Mg. Less Fe and Mg were incorporated into these smectites, due to the paucity of Fe^{2+} and Mg^{2+} in the sample rocks (and high- SiO_2 rocks in general). Therefore the secondary smectite formed in our experiments can be classified as beidellitic. Topologic mineral stability diagrams indicate that the equilibrium between secondary illite and beidellitic smectite in our high- SiO_2 rock:water experiments resulted in comparatively lower solution pH (compared to basalt). BRT:1 and CG:2 stable pH values (approx. avg. = 6.5) are similar, suggesting that the smectites formed in these experiments are similar in composition.

6) Icelandic geothermal fluid, CG:2, BRT:1, and Temple 300°C basalt:water experiment, stable log cation/proton ratio comparisons indicate that granite points lie closest to the center of Icelandic geothermal field scatter (followed in close order by basalt and tuff points, respectively).

7) Quartz, Na-K, and Ca-Na-K solution geothermometer trend data from CG:2, BRT:1, and Temple 300°C basalt experiments were compared. Granite geothermometers were the most accurate in predicting actual solution temperature followed by the basalt and tuff geothermometers, respectively. Tuff apparent solution temperatures are much higher than other values calculated from Temple 300°C autoclave experiments, and geothermal fluids.

**SUMMARY OF HIGH-LEVEL NUCLEAR WASTE DISPOSAL
IMPLICATIONS**

1) RADIONUCLIDE RELEASE RATES:

These results suggest that redox buffering capacity would probably be exhausted most rapidly in a tuff repository followed by granite, and basalt, respectively. More oxidizing percolating repository solutions may result in higher solubility of UO_2 for spent fuel rods. Solution pH may also effect radionuclide release rates. The solubility of UO_2 for spent fuel rods in repository solutions depends on the type of uranium complex formed. Using a log fO_2 -pH phase diagram (McKeon, 1984) it was determined that UO_2 contained within spent fuel rods, would form $UO_2F_3^-$ in the tuff solution, and $U(OH)_5^-$ in the granite solution. If $UO_2F_3^-$ forms in tuff repository solutions than the solubility of UO_2 in spent fuel rods would be higher in; lower pH solutions, oxidizing solutions, and solutions rich in fluoride. If $U(OH)_5^-$ forms in granite repository solutions then higher hydrogen activities would result in higher solubility of UO_2 from spent fuel rods. The stable granite solution pH is only slightly higher than the corresponding

BRT:1 stable pH. The stable tuff log fO_2 is 3-5 five units more oxidizing than CG:2 granite, and the highly soluble rhyolitic glass released comparatively high concentrations of F (stable avg. approx.= 20 mg/l) into the tuff solution. If the uranium complexes predicted to be in equilibrium with the granite and tuff solutions are formed in lower temperature repository solutions, spent fuel rods would release U-complexes more rapidly into surrounding groundwater at a tuff repository.

2) HIGH-LEVEL NUCLEAR WASTE CONTAINER

CORROSION RATES:

Stainless steel and low-carbon steel are the primary materials being considered for high-level nuclear waste containers. However waste containers manufactured using these materials would corrode rapidly upon interaction with oxidizing repository solutions. Pure Cu is considered to be superior since this metal is not expected to oxidize in repository solutions. Stable solution fO_2 data and redox buffering capacity calculations, suggest that tuff-glass influenced repository solutions would be oxidizing (compared to granite and basalt). The

exhaustion of repository glassy-tuff-redox buffering capacity may result in more oxidizing solutions, near the fO_2 of corrosive solubility of Cu-waste containers. If this were to occur, then Cu-waste container corrosion rates may increase, resulting in the release of radionuclides into repository groundwater.

More acidic solutions also would result in comparatively higher rates of container corrosion. Stable solution pH calculated in these high-SiO₂ rock:water experiments (avg. approx.= 6.5) are 1 to 1.5 pH units more acidic than those calculated in 300°C Temple basalt experiments (approx. range= 7.5 to 8). The pH of these experimental solutions appear to be controlled by host rock (FeO + MgO) content and smectite precipitation. If these factors control solution pH in lower temperature infiltrating repository solutions, then container corrosion may be relatively more rapid in a tuff or granite rock enclosed high-level nuclear waste repository.

3) RADIONUCLIDE MOBILITY AND POROSITY:

The dominant secondary mineral formed in 300°C Temple basalt experiments is saponite (a very Fe-Mg-rich smectite). In these basalt experiments saponite formed in copious amounts (illite formed in lesser quantities). The primary secondary mineral formed in experiments CG:2 and BET:1 was illite (2M₁). Beidellitic smectites were also identified in lesser quantities. These results indicate that the illite/smectite mass ratio is higher for our high-SiO₂ rock:water secondary mineral assemblages (compared to basalt:water experiments). If the illite/smectite ratio is similarly affected by rock type and crystallinity in lower temperature repository solutions, then the sorption capabilities of greater quantities of smectites in basalt repository solutions should have comparatively beneficial effects in lowering the mobility of some radionuclides (compared to granite and tuff). The precipitation of large amounts of smectite at a basalt repository would result in a comparatively larger decrease in porosity near waste containers (compared to tuff and granite sites). Decreased porosity near repository waste containers at a basalt enclosed

repository would also result in relatively lower radionuclide mobility (compared to granite and tuff).

Lesser amounts of secondary minerals were formed in experiment CG:2 (when compared to basalt and tuff). The formation of lesser quantities of secondary minerals in granite repository solutions, should result in comparatively high porosity near waste containers (compared to basalt and tuff). Higher porosity at granite repository site would result in comparatively high radionuclide mobility (compared to basalt and tuff).

**SUMMARY OF THE IMPLICATIONS OF USING 300°C GRANITE,
GLASSY TUFF AND BASALT SHORT-TERM DICKSON ROCKING
AUTOCLAVE EXPERIMENTS TO PREDICT LONG-TERM
GEOHERMAL FLUID CHEMISTRY**

1) CATION/PROTON MASS RATIO COMPARISONS

Diagrams were constructed to compare BRT:1, CG:2, 300°C Temple basalt, and Icelandic geothermal fluid; $\text{Ca}/(\text{H})^2$ vs. Na/H , Na/H vs. K/H , and $\text{Mg}/(\text{H})^2$ vs. $\text{Ca}/(\text{H})^2$ data scatter. In these diagrams the stable granite data plot closest to the center of

Icelandic geothermal fluid scatter, followed by tuff and basalt data points, respectively. This comparison suggests that the granite experiment came closest to the long-term geothermal fluid chemistry followed by the tuff and basalt experiments, respectively.

2) SOLUTION GEOTHERMOMETER COMPARISONS

Differences in BRT:1, CG:2, and 300°C Temple basalt experiment solution geothermometer trends were analyzed. The granite; Ca-Na-K and Quartz geothermometer trends came closest to approximating actual experimental temperatures, followed by basalt and tuff, respectively. All of the tuff geothermometers provided very high apparent solution temperatures suggesting that rhyolitic glass dissolution may perturb the Na-K, Ca-Na-K, and quartz geothermometers. The Na-K geothermometer does not accurately predict actual experimental temperatures in these and other autoclave experiments.

These results suggest that the durations of these experiments were not adequate for the equilibrium between albite and microcline to control Na and K concentrations. The closer

correspondence of the Ca-Na-K and quartz geothermometers in the holocrystalline granite experiment followed by the basalt (10-40%-glass) and tuff (95%-glass) experiments, suggest that rock type and crystallinity may effect the amount of rock:water interaction time necessary to predict long-term geothermal fluid chemistry (10^3 - 10^5 years).

Secondary quartz, and high albite were identified in the secondary mineral assemblages removed from CG:1 and CG:2 quench solutions. These minerals are commonly found in the stable mineral assemblages formed in geothermal fluids, suggesting that stable mineral assemblages began to form in experiment CG:2 within 2761 hours. Most of the minerals identified in the tuff and basalt experiments represent metastable assemblages.

Solution:glass phase reactions lead to a high level of supersaturation with respect to a variety of aluminosilicate minerals. In such supersaturated solutions a sequence of metastable reactions will occur resembling an Ostwald step sequence (Dibble et al., 1981). After a series of steps stable mineral assemblages will form. However the formation of intermediate metastable minerals may delay this eventuality for millions of

years. The experiments compared in the cation/proton ratio and geothermometer comparison seem to approach long-term geothermal solution chemistry in the following order; holocrystalline Conway Granite, 10-40% glass Basalt, 95% Bannock Rhyolite Tuff. These results suggest that the amount of time required to emulate long-term geothermal solutions in short-term autoclave experiments, is dependent on the amount of glass contained within the rock. Using this logic, holocrystalline granite (or gabbro) autoclave experiments would emulate long-term natural geothermal solution chemistry in comparatively shorter periods of time.

These data indicate that when natural analogs (geothermal fields) are used to predict the long-term solution chemistry of high-level nuclear waste repository solutions, the effect of glass dissolution should be considered.

REFERENCES

Abelin, H., Birgersson L., Gídlund J., Koreno L., Agren, T., Widen H., Neretnieks, I. (1988) 3-D migration experiment in sparsely fractured crystalline rock. Mat. Res. Soc. Symp. Proc. 112:199-207.

Arnorsson, S., Gunnlaugsson, E. (1983) The chemistry of geothermal waters in Iceland. II. Mineral equilibria and independent variables controlling water compositions. Geochim. Cosmochim. Acta 47:547-566.

Arnorsson, S., Gunnlaugsson, E. (1983) The chemistry of geothermal waters in Iceland. III. Chemical geothermometry in geothermal investigations. Geochim. Cosmochim. Acta, 47:567-577.

Billings, M. P. (1964) Chemical analyses of rocks and rock-minerals from New Hampshire, Mineral Resources Survey, New Hampshire Div. of Econ. Develop., Part XIX.

Birgersson, L., Neretnieks I. (1988) Diffusion in the matrix of granitic rock field test in the Strip Mine. *Mat Res. Soc. Symp. Proc.* 112:189-199.

Carlos, B. A. (1985) Occurrence of fracture-lining minerals in silicic tuffs, Yucca mountain, Nevada, USA. *In*, Fifth International Symposium on Water-Rock Interaction, Reykjavik, Iceland, 96-99.

Charles, R. W., Bayhurst, G. K. (1983) Rock-fluid interactions in a temperature gradient: Biotite granodiorite + H₂O. *In*: Heiken G, Goff F. (Eds.) Geothermal energy from hot dry rock. *J. Volcanol. Geotherm. Res* 15:137-166.

Delaney, J. M. (1985) Reaction of Topopah Spring Tuff with J-13 water: A geochemical modeling approach using the EQ3/6 reaction path code, Lawrence Livermore National Laboratory, Livermore, CA, UCRL-53631.

Dibble, W. E. Jr., Tiller, W. A. (1981) Kinetic model of zeolite paragenesis in tuffaceous sediments. *Clay and Clay Minerals* 29: 5:323-330.

Dickson, F. W. (1977) The reaction of granite with seawater at 300°C and 1000 bars. EOS (Transactions of the Am. Geophys. Union), 58:1251 (abstract)

Dickson, F. W., and Potter J. M. (1982) Rock-Brine interactions. EPRI AP-2258. Electrical Power Research Institute, Palo Alto, Ca.

DOE/TIC-11033 (1980) Earth Science technical plan for disposal of nuclear waste in a mined repository. U. S. Department of Energy, Office of Radioactive Waste Management, Washington, D.C. 20585.

DOE/RW-0198 (1988) Nuclear waste policy act (Section 113). Site characterization plan overview. Yucca Mountain site, Nevada research and development area, Nevada. U. S. Department of Energy, Office of Radioactive Waste Management, Washington, D.C. 20585.

Fournier, R. O. (1981) Application of water geochemistry to geothermal exploration and reservoir engineering. Chapter 4 In Geothermal Systems, L. Ryback and L. Muffler, eds., (Wiley, New York), 109-143.

Fournier, R. O., and Potter, R. W. (1982) A revised and expanded silica (quartz) geothermometer. Geothermal Res. Council Bull., 11:3-9.

Fournier, R. O., and Truesdell, A.H. (1973) An empirical Na-K-Ca Geothermometer for natural waters. Geochim. Cosmochim. Acta, 37:1255-1275.

Fournier, R. O., and Potter, R. W. (1979) Magnesium correction to the Ca-Na-K geothermometer. Geochim. Cosmochim. Acta, 43:1543-1550.

Gardiner, M. A. (1988) Hydrothermal reaction of groundwater with basalt from the entablature of the Cohasset flow, Grande Ronde formation, Hanford, Washington: The effect of the introduction of fresh solution to the system at 200° and 300°C, and 30 MPa. Master of Arts Thesis, Temple University, Philadelphia, PA, 152 p.

Gardiner, M. A., Ulmer G. C., and Grandstaff D. E (1989) Application of a reinjection technique to Dickson hydrothermal experiments: The effect of introducing fresh solution to the basalt-water system at 300°C and 30 MPa. Proceedings of the 6th International Water-Rock Symposium, Malvern, U.K.,

239-242.

Giggenbach, W. F. (1987) Redox processes governing the chemistry of fumarolic gas discharges from White Island, New Zealand. *Applied Geochemistry*, 2:143-161

Grandstaff, D. E., Foster, R. W., Korn, R., and Ulmer, G. C. (1985) Measurement of hydrothermal redox using a direct hydrogen evolution method (DHEM) (Abstract)., In Proceedings of the Second International Symposium on Hydrothermal Reactions, Pennsylvania State University, p. 10.

Grandstaff, D. E., McKeon, G. L., Moore, E. L., and Ulmer, G. C. (1984) Reactions in the System Basalt Simulated Spent Fuel/Water. *Material Res. Soc. Symp. Proc. V. 26.*

Grandstaff, D. E., and Ulmer, G. C. (1985) Buffering capacity and redox control in water-rock systems. *Rockwell Hanford Document RHO-SD-TI-298.*

Grossman, D., Shulman S., A Nuclear Dump: The Experiment Begins (1989) *Nature*, 49-56.

Helgeson, H. C., Kirkham, D. H., Flowers, G. C. (1981) Theoretical prediction of the thermodynamic behavior of aqueous electrolytes at high pressures and temperatures IV. Calculation of activity coefficients, osmotic coefficients, and apparent molal and standard and relative partial molar properties to 600°C and 5 Kb. Amer. J. Sci. 281: 1249-1516.

Hanley, R. W., Truesdell, A. H., and Barton, P. B., Jr. (1984) Chapter 3: Chemical geothermometers for geothermal exploration. In, Reviews in Economic Geology, 1:31-43.

Hoag R. B. Jr., Glenn W. Stewart (1977) Preliminary petrographic and geophysical interpretations of the exploratory geothermal drill hole and core, Red Stone, New Hampshire. U.S. Energy Research and Development Administration, Doc. No. COO-2720-1.

Ingamells, C.O. (1960) A new Method for "Ferrous Iron" and "Excess Oxygen" in rocks, minerals, and Oxides. Talanta 4:268-273.

Jassey, D. R., Kilpatrick Rose M. (1986) PETRX; A program to classify igneous rocks, personal

computer software for geological education, Rober Burger Ed., NAGT Special Publication 1.

Kacandes, G. H., Ulmer, G. C., and Grandstaff, D. E. (1986) Icelandic geothermal fields as an analog for nuclear waste isolation in Columbia Plateau (Washington, USA) basalt. In, Fifth International Symposium on Water-Rock Interaction, Orkustofnun, Reykjavik, 302-305.

Kacandes, G. H., Ulmer, G.C., and Grandstaff, D.E. (1989) Monitoring the evolution of alteration minerals and fluids during a hydrothermal experiment. Proceedings of the 6th international water-rock interaction symposium, Malvern, U.K., 353-356.

Kacandes, G. H. (1989) Water/rock experiments to 300°C and comparisons to chemical interactions in active geothermal systems. Master of Arts Thesis, Temple University, Philadelphia, PA, 241 p.

Kishima, N., and Sakai, H. (1964) Fugacity-concentration relationship of dilute hydrogen in water at elevated temperature and pressure. Earth and Planet. Sci. Lett., 67:79-86.

Knauss, K. G., Beiriger, W. J., Peifer, D. W.
(1987) Hydrothermal interaction of solid wafers of
Topopah Spring tuff with J-13 water at 90 and 150°C
using Dickson-type, gold-bag rocking autoclaves:
long-term experiments, Lawrence Livermore National
Laboratory, Document No. UCRL-53722

Knauss, K. G., Beiriger, W. J., (1984) Report on
static hydrothermal alteration studies of Topopah
Spring Tuff wafers in J-13 water at 150°C, Lawrence
Livermore National Laboratory, Document No. UCRL-
53576

Korn, R. A. (1986) A comparison of the hydrothermal
stability of the Columbia Plateau Basalts from the
Umtanum and Cohasset flows at 100, 200, and 300°C;
and at 30 MPa. Master of Arts thesis, Temple
University, Philadelphia, PA, 126 p.

Lazaar, P. I. (1988) A study of the hydrothermal
stability of copper for use as a container
material for nuclear waste at the Hanford site,
Richland, Washington. Master of Arts thesis,
Temple University, Philadelphia, PA, 97 p.

Lee, A. C., Grandstaff D.E., Ulmer G.C. (1990) The effect of rhyolitic glass on solution parameters in autoclave experiments at 300°C and 30 MPa, EOS (Transactions of the Am. Geophys. Union), 71:663 (abstract)

LeMaitre R.W. (1976) The chemical variability of some common igneous rocks. Journal of Petrology 17:589-637, 40 figs.

Lipman, P. W. (1967) Chemical composition of glassy and crystalline volcanic rocks. GSA Special Paper 82:260-261

McKeon, G. L. (1984) Hydrothermal reaction of simulated spent fuel with Columbia Plateau Basalt from the Umtanum flow at 100°, 200°, 300°C; and at 30 MPa (300 Bars). Master of Arts thesis, Temple University, Philadelphia, PA, 108 p.

Moore, E. L. (1983) Hydrothermal interaction of Columbia River Basalt from the Umtanum Formation with its coexisting-groundwater. Master Of Arts Thesis, Temple University, Philadelphia, PA, 89p.

Moore, E. L., Ulmer, G. C., and Grandstaff, D. E. (1985) Hydrothermal interaction of Columbia Plateau Basalt from the Ontanum Flow (Washington, USA) with its coexisting groundwater. *Chemical Geol.*, 49:53-71.

Moreno, L., Neretnieks I. (1988) Channeling and its potential consequences for radionuclide transport. *Mat. Res. Soc. Symp. Proc.* 112:169-178.

Myers, W. B. (1946) Preliminary map of the N.W. 1/4 of the Willis Quadrangle, Beaverhead County, Montana. Montana Bureau of Mines and Geology. Open File Map MBMG 189.

Naumov, G. B., Ryzhenko B.W., Khodakovasky (1974) Handbook of Thermodynamic data, N.T.S.B. Doc no. ppB 226-727:243-245.

Ohmoto, H., and Lasaga, A. C. (1982) Kinetics of reactions between aqueous sulfates and sulfides in hydrothermal systems. *Geochim. Cosmochim. Acta*, 48:1727-1745.

Oversby, V. M. (1984) Reaction of the Topopah Spring Tuff with J-13 water at 120°C, National

Livermore National Laboratory, Document no. UCRL-53574.

Overaby, V. M. (1985) The reaction of Topopah Spring Tuff with J-13 water at 150°C-Samples from drill cores USW G-1, USW GU-3, USW G-4, and US-25h#1, National Livermore National Laboratory, Document no. UCRL-53629.

Potter, J. M. and Dibble, W. H. (1986) Experimental calibration of the Na/K geothermometer: flow through studies. In, Fifth International Symposium on Water-Rock Interaction, Orkustofnun, Reykjavik, Iceland, 444-447.

Sato, S., Furuya, H., Sakamoto, Y., Okuno, T., Yabe, I. (1985) Migration behavior of U(VI) in a granitic rock. In, Fifth International Symposium on Water-Rock Interaction, Reykjavik, Iceland, 481-484.

Savage, D. (1984) The Geochemical interactions between simulated borosilicate waste glass, granite, and water at 100-350°C and 50 MPa. Rep. Br. Geologic Survey, FLPV 84-3.

Savage, D., Cave, M. E., Milodowski A. E., and George I. (1987) Hydrothermal alteration of granite by meteoric fluid: An example from the Carnmenellis Granite. United Kingdom, Contributions to Mineralogy and Petrology, 96:391-405.

Savage, D. (1986) Granite-water interactions at 100°C, 50 MPa: An Experimental Study., Chemical Geology, 54:81-95.

Seyfried, W. E., Janecky, D. R. and Berndt, M. (1987) Dickson Rocking autoclaves for hydrothermal experiments II. The flexible reaction cell system. Hydrothermal Experimental Techniques, G. C. Ulmer and H. L. Barnes, eds. (Wiley, New York).

Smith B. (1968) High Albite JCPDS Card 20-572. American Mineralogist 53:1709.

Ulmer G. C., Grassi V. J., Lee A. C., Grandstaff D. E. (1990) Comparison of tuff, granite, and basalt as high-level repository host rocks: lithologic factors influencing fluid compositions, Nat. Res. Ass. (abstract), in press.

Ulmer, G. C., Kacandes, G. H., and Grandstaff, D. E. (1987) Icelandic geothermal fields as an analog for nuclear waste disposal in basalt. In, Nuclear Waste Management In, Advances in Ceramics, Vol.1 20, D. E. Clark, ed. (Ceramic Society, Columbus, OH), 755-764.

Ulmer, G. C., Grandstaff D. E., Foster, R. W., Korn, R. (1985) Applications of DHEM to nuclear repository design (Abstract)., In Proceedings of the Second International Symposium on Hydrothermal Reactions, Pennsylvania State University.

Van der Graaf, T. T., Grondin, D. M., Draw, D. J. (1988) Laboratory radionuclide migration experiments at a scale of 1 m., Mat. Res. Soc. Symp. Proc. 112:159-168.

Van der Plas, L. A. (1965) A chart for judging the reliability of point counting results. Am. Journal of Science 263:87-90.

Wang, J., Gardiner M.A., Grandstaff D.E., and Ulmer G.C. (1989) Differentiation in mesostasis and the effect on the hydrothermal redox buffering capacity of Basalt, Proceedings of the 6th

international water:rock interaction symposium,
Malvern, U. K., 735-737.

White, D. E. (1965) Saline waters of sedimentary
rocks, In: Fluids in subsurface environments-a
symposium. Memoir Am. Assn. Petrol. Geol., 4:347-
366

Whitney, J. A., Stormer J.C. Jr. (1976)
Geothermometry and geobarometry in epizonal
granitic intrusions: a comparison of iron-titanium
oxides and coexisting feldspars, American
Mineralogist, 61:751-761.

Winchell, A. N. (1914) Mining Districts of the
Dillon Quadrangle, Montana and adjacent areas, USGS
Bulletin 574:43-44.

Woodley, R. E., Wilson, C. N. (1981) The chemical
and physical characteristics of spent light water
reactor fuel and a method for simulation of a
nonradioactive analog, RHO-BWI-C-114, Rockwell
Hanford Operations, Richland, Washington.

Appendix 1a: BRT:1 activities and activity ratios as calculated by the computer program MIPMPR2.

RUN	0	1	2	3	4	5	6	7	8	10
log Ca/H ₂	5.67	5.61	4.64	7.95	7.88	8.35	8.06	8.04	7.29	7.52
log Mg/H ₂	4.65	4.24	2.88	6.26	6.41	6.69	6.79	6.56	5.83	6.12
log Na/H	3.18	2.57	1.90	3.98	3.92	3.93	4.08	4.22	3.73	3.92
log K/H	0.46	2.53	1.82	3.74	3.77	3.81	3.88	4.02	3.58	3.78
log H ₄ SiO ₄	-4.456	-1.604	-1.500	-1.526	-1.480	-1.512	-1.545	-1.534	-1.502	-1.550
log Na/K	2.717	0.044	0.080	0.234	0.146	0.126	0.191	0.204	0.153	0.140
log Na/Ca ^{0.5}	0.348	-0.234	-0.418	0.002	-0.018	-0.242	0.047	0.200	0.087	0.157
log Ca/Mg	1.015	1.376	1.759	1.690	1.464	1.658	1.268	1.485	1.453	1.397
log Al/H ³	-----	0.620	0.228	-1.328	-1.433	-1.474	-1.834	-2.301	-0.977	-1.319

Appendix 1b: CG:2 activities and activity ratios as calculated by the computer program MIPMPR2.

RUN	0	1	2	3	4	5	6	7	8
log Ca/H ₂	4.90	9.07	9.25	8.96	8.97	8.21	6.75	8.86	8.15
log Mg/H ₂	4.41	7.59	7.60	7.58	7.17	6.79	6.97	6.81	6.12
log Na/H	3.07	4.71	4.73	4.51	4.45	4.23	4.35	4.29	4.20
log K/H	1.32	3.94	3.98	3.81	3.82	3.54	3.78	3.69	3.68
log H ₄ SiO ₄	-4.446	-2.150	-2.008	-1.908	-1.922	-1.924	-1.944	-1.909	-1.991
log Na/K	1.749	0.769	0.748	0.703	0.633	0.688	0.569	0.603	0.525
log Na/Ca ^{0.5}	0.618	0.173	0.103	0.032	-0.035	0.125	-0.025	-0.139	0.129
log Ca/Mg	0.484	1.476	1.645	1.380	1.806	1.426	1.773	2.054	2.035
log Al/H ³	----	-1.317	-1.483	-1.474	-1.527	-1.315	-1.526	-1.425	-1.280

APPENDIX 2: ANALYTICAL METHODS AND ERROR RANGES

<u>ELEMENT</u>	<u>METHOD</u>	<u>ERROR RANGE</u>
H ₂ gas	GAS CHROMATOGRAPH	± 0.1 log fO ₂
pH _E	pH METER	± 0.05 pH units
SiO ₂	ATOMIC ABSORPTION	± 5%
K	ATOMIC ABSORPTION	± 5%
Na	ATOMIC ABSORPTION	± 5%
Ca	ATOMIC ABSORPTION	± 5%
Al	ATOMIC ABSORPTION	± 10%
Mg	ATOMIC ABSORPTION	± 2%
Fe	ATOMIC ABSORPTION	± 5%
Mn	ATOMIC ABSORPTION	± 10%
Li	ATOMIC ABSORPTION	± 5%
F	ION CHROMATOGRAPH	± 10%
SO ₄	ION CHROMATOGRAPH	± 5%
Cl	ION CHROMATOGRAPH	± 10%
ECO ₂	INFRARED CARBON ANALYZER	± 10%
EH ₂ S	SPECIFIC ION ELECTRODE	± 10%